

Strain, size and field effects in (La,Ca)MnO₃ thin films

Christianne Beekman

Casimir PhD series 2010-08
ISBN: 978-90-8593-072-3
©2010 Christianne Beekman

Dit werk is uitgevoerd aan de Universiteit van Leiden en maakt deel uit van het onderzoeksprogramma van de Stichting voor Fundamenteel Onderzoek der Materie (FOM), die financieel wordt gesteund door de Nederlandse Organisatie voor Wetenschappelijk Onderzoek (NWO).

Strain, size and field effects in (La,Ca)MnO₃ thin films

Proefschrift

ter verkrijging van
de graad van Doctor aan de Universiteit Leiden,
op gezag van de Rector Magnificus prof. mr. P.F. van der Heijden,
volgens besluit van het College voor Promoties
te verdedigen op donderdag 25 februari 2010
klokke 16:15 uur

door

Christianne Beekman
geboren te Amsterdam
in 1980

Promotiecommissie

Promotor: Prof. dr. J. Aarts
Overige leden: Prof. dr. M. G. Blamire (University of Cambridge)
Prof. dr. P. H. Kes
Dr. ing. A. J. H. M. Rijnders (Universiteit Twente)
Prof. dr. J. M. van Ruitenbeek
Prof. dr. J. Zaanen
Prof. Dr. H. W. Zandbergen (Universiteit Delft)

Omslag: door Rina Beekman

Table of Contents

1	Introduction	1
2	The physics of doped manganites	5
2.1	The parent compound: LaMnO_3	5
2.1.1	The Crystal structure	5
2.1.2	The electronic configuration	7
2.1.3	Jahn-Teller distortions	8
2.2	Competing phases and ordering phenomena	9
2.2.1	Intermediate doping	9
2.2.2	Low and high doping: charge and orbital ordering	12
2.3	Electronic phase control	13
2.3.1	Epitaxial strain as a tuning parameter	14
2.3.2	Disorder-induced effects	14
3	Sample fabrication and characterization	19
3.1	Thin film growth	20
3.1.1	DC-sputtering	20
3.1.2	Reactive DC-sputtering	20
3.1.3	Growth process	21
3.2	Sample characterization	22
3.2.1	Morphology and film thickness	22
3.2.2	Reciprocal space mapping	25
3.3	Microstructure and Mn valency	27
3.3.1	Microstructure	28
3.3.2	Mn-oxidation state and elemental composition	28
3.3.3	Discussion	33
3.4	Summary	34
3.5	Patterning thin films	35
3.6	Measuring thin films	36
3.7	Conducting STO: problem and solution	37
3.7.1	The effect of Ar-ion etching on STO	37
3.7.2	Conducting STO: solution	38

3.7.3	Contact resistance and Joule heating	39
4	Strain effects in (La,Ca)MnO₃ thin films	45
4.1	Introduction	45
4.2	Transport properties and magnetization measurements	46
4.2.1	T _{MI} dependence on thickness	46
4.2.2	Magnetic properties	50
4.2.3	Discussion	53
4.3	Low field magnetoresistance	56
4.3.1	Introduction	56
4.3.2	Films on flat STO	56
4.3.3	Films on 1° misoriented STO	58
4.3.4	Discussion	59
4.4	Conclusion	61
5	Mesoscopic transport in (La,Ca)MnO₃ thin films	65
5.1	Introduction	65
5.2	LCMO microbridges on flat STO	66
5.3	LCMO microbridges on NGO	72
5.4	LCMO microbridges on 1° STO	73
5.5	Discussion	76
5.6	Conclusion	79
6	Electric field effects in (La,Ca)MnO₃ thin films	83
6.1	Introduction	83
6.2	STO: backgate dielectric	85
6.2.1	The device	85
6.2.2	Electrostriction	86
6.2.3	Possibility of leak current	87
6.3	Gating effects in LCMO microbridges	88
6.4	Discussion	92
6.5	Conclusion	93
7	Putting the pieces together	95
Appendix: (La,Ca)MnO₃ nanowires, growth process and preliminary find-ings		97
A.1	Introduction	97
A.2	Growth process	97

A.2.1	The sol-gel process	97
A.2.2	Templates and pores	99
A.3	LCMO nanowires	102
A.3.1	Viscosity	102
A.3.2	Commercial anodized alumina template	103
A.3.3	Custom anodized alumina template	105
A.3.4	Polycarbonate template	107
A.4	Discussion	111
A.5	Conclusion	111
	Samenvatting	113
	Summary	115
	Curriculum vitae	117
	Publicatielijst	119
	Nawoord	121

Chapter 1

Introduction

Transition metal oxides with the perovskite structure are strongly correlated electron systems which show diversity in physical properties caused by the competition between charge, spin and orbital degrees of freedom. Examples of such systems are PbTiO_3 which shows ferroelectricity, La_2CuO_4 and LaMnO_3 which are Mott insulators and SrTiO_3 (STO) which is a high k dielectric. Even larger diversity in physical properties arises upon doping (electrons or holes) into the insulating matrix, through substitution of different ions. This leads to high T_C superconductivity in $(\text{La}, \text{Sr})_2\text{CuO}_4$ and ferromagnetic metallic behavior in $(\text{La}, \text{Ca})\text{MnO}_3$. The occurrence of various types of collective behavior (superconductivity, magnetism, ferroelectricity) within one class of crystal structures makes them appealing for fundamental studies, for researching novel phenomena by combining different properties in hybrid materials, and also for applications. Especially, the fact that doping the insulators invokes a metal-insulator transition in many of these compounds allows to think about electric field control of the metallicity or conductance such as already exploited in Field Effect Transistors (FET). Currently FET's are based on conventional structures such as Si. However, the dimensions of these semiconductor microstructures are reaching their intrinsic physical limit. Further increase of circuit density requires the consideration of different channel and gate-oxide materials, such as transition metal oxides, and redesigning the device microstructure. The perovskite oxide class provides a wide range of materials which might be used in such devices. For instance in ref. [1], conductivity switching of the perovskite type material, $\text{YBa}_2\text{Cu}_3\text{O}_{7-\delta}$ (YBCO) is explored, by varying the doping level with an applied electric field. In the reported nanoscale device, use was made of the fact that thin films of YBCO can be epitaxially grown on STO, but that at the same time the high electric polarizability of STO allows it to be used as a gate oxide.

Our goal is the characterization of the electrical transport properties of $\text{La}_{0.67}\text{Ca}_{0.33}\text{MnO}_3$ (LCMO) thin films and micron-sized structures, to investigate novel behavior for a better understanding of the physics in these small geometries

and material functionality in view of possible future application. The use of thin film growth is necessary to investigate transport on mesoscopic lengthscales. In this thesis a process to successfully grow and pattern thin LCMO films into microbridges is presented. We investigate the differences in magnetotransport properties going from as-grown unstructured thin films to microbridges with micron dimensions. The focus here is on films grown on STO substrates, which can be used as backgate dielectric, but which also imposes tensile strain on the LCMO thin film. This makes it necessary to investigate the influence of strain states and disorder. That is done by using substrates imposing less strain, but also through varying the amount of atomic steps on the STO substrate surface. Substrates which contain unit cell high steps on the surface impose variations of crystallographic disorder in the film; this may influence transport, especially on small length scales. The FM-PI phase transition is susceptible to such crystallographic disorder (doping disorder, oxygen nonstoichiometry, defects from strain relaxation, twinning, and grain boundaries) which can lead to an inhomogeneous state in which the insulating and metallic phases coexist on a variety of length scales. For strained LCMO microbridges, we show that the percolative nature of the conductance leads to E-field sensitivity. Furthermore, the conductance shows non-linear behavior and even a novel kind of melting of the insulating state, which we attribute to the formation of an intervening glassy polaron state when going from the correlated metal to the polaronic insulator.

Outline of the thesis

In the following a short outline of this thesis is given. In **Chapter 2** we introduce the material $\text{La}_{1-x}\text{Ca}_x\text{MnO}_3$. We give a background on the crystal structure, the effect of doping (the phase diagram), the FM-PI transition and the conduction and (magnetic) ordering mechanisms involved. In **Chapter 3** the experimental techniques used for sample fabrication, measurements and details on sample characterization are described, which includes studies of the microstructure and composition of our thin films. Furthermore, we describe in detail a problem which occurs when conventional Ar-etching is used in the lithography process of LCMO thin films grown on STO substrates. We also present a solution enabling us to reliably measure current effects intrinsic to our LCMO microbridges. In **Chapter 4** we present the results of the magnetotransport properties and magnetoresistance measurements of the unstructured thin films as function of film thickness. We also discuss the influence of step edges on the transport properties. In **Chapter 5** we present the magnetotransport properties of LCMO microbridges. In **Chapter 6** we describe the electric field effect device and we present results on the effect of electric fields on transport properties of the microbridges. We correlate the findings from **Chapters 4-6** in **Chapter**

7 "Putting the pieces together".

Large magnetoresistance effects, nonlinear behavior and electric field effects are observed around the FM-PI transition. For LCMO films on STO substrates the transition occurs between 100 - 170 K, quite far below room temperature. The material LCMO can only be used in applications if the transition can be moved closer to room temperature, without sacrificing the strength of the above mentioned effects. Recently, Shankar et al. [2] claimed that in single crystalline LCMO nanowires, the Curie temperature is shifted to above room temperature! We conclude the thesis with an **Appendix** on the development of a growth procedure for LCMO nanowires, through a template assisted sol-gel process. We also show some preliminary results on the characterization of these wires.

Bibliography

- [1] D.M. Newns, T. Doderer, C.C. Tsuei, J.A. Misewich, A. Gupta, B.M. Grossman, A. Schrott, B.A. Scott, P.C. Pattinaik, R.J. von Gutfeld and J.Z. Sun, *J. Electroceramics* **4**, 339 (2000); D. M. Newns, J. A. Misewich, C. C. Tsuei, A Gupta, B. A. Scott, and A. Schrott, *Appl. Phys. Lett.* **73**, 780 (1998)
- [2] K. S. Shankar and A. K. Raychaudhuri, *Nanotechnology* **15**, 1312 (2004); K. S. Shankar, S. Kar, A. K. Raychaudhuri, and G.N. Sabbanna, *Appl. Phys. Lett.* **84**, 993 (2004)

Chapter 2

The physics of doped manganites

The rare earth perovskite oxide manganites have the general formula $R_{1-x}A_xMnO_3$, in which R is a trivalent rare earth element (examples: La, Pr, Sm) and A is a divalent alkaline earth element, such as, Ca, Sr and Ba. The physics of this class of materials depends heavily on the amount of A-doping. We start this chapter with a discussion on the parent compound ($LaMnO_3$, section 2.1). We explain the effect of Ca-doping on the crystal structure and the Mn-valence state of the material, which leads to different types of ordering phenomena. At intermediate doping ($0.2 < x < 0.5$) the material exhibits a combined metal-insulator and ferromagnetic-paramagnetic transition and the well known colossal magnetoresistance effect (CMR), which is described in section 2.2.1. At higher doping levels ($x > 0.5$) the material is charge and orbital ordered (CO, OO), which is explained in section 2.2.2. The competition between several interactions makes that only small energy differences exist between the different possible phases of the system. As a result the phase of the material can be tuned by various external perturbations, such as magnetic and electric fields, strain and disorder. These perturbations may lead to large effects (for example orders of magnitude resistance change by applying a magnetic field: the CMR effect) and can be used for electronic phase control in manganite devices. In section 2.3 a short overview will be given on theoretical and experimental efforts concerning phase tuning in manganites.

2.1 The parent compound: $LaMnO_3$

2.1.1 The Crystal structure

The crystal structure of $LaMnO_3$ (LMO) is of the ABO_3 , perovskite type shown in Fig. 2.1a. The A-atom is located at the center of the cube and the B-atoms are at the corners. The B-atoms are surrounded by (coupled) oxygen octahedra which form a BO_6 complex. The structure shown here is cubic and is an ideal representation which

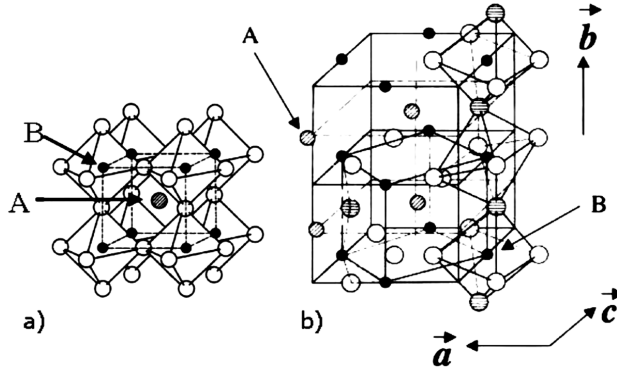


Figure 2.1 — Crystal structure of LaMnO_3 . The A-site is occupied by La-ions and the B-site is occupied by the Mn-ions. The white spheres indicate the six oxygen ions which surround the Mn-ion. a) Ideal cubic structure with $t = 1$. b) The orthorhombic ($Pnma$) structure with the buckling of the octahedra around the a , b and c axes.

only holds when the tolerance factor t ,

$$t = \frac{(r_A + r_O)}{\sqrt{2}(r_B + r_O)} \quad (2.1)$$

is equal to 1 (r_A , r_B and r_O denote the radii of respectively the A, B and oxygen atoms) [1]. Consequently when the A-atoms do not have an optimal size compared to the BO_6 complex the tolerance factor deviates from 1 (for La, Sr and Ca, $t < 1$). This results in the buckling of the octahedra in order to accommodate the A-atom and fill the extra empty space. The buckling consists of cooperative rotations of the MnO_6 octahedron around one or several axes of the initial cubic lattice. The amount of rotation depends on the value of the tolerance factor and for values close to unity the distortions lead to a rhombohedral structure. For lower values (in general $t < 0.96$) the rotations around the a , b and c axis, which are denoted in Fig. 2.1b, result in the formation of the orthorhombic ($Pnma$) structure; this structure has lattice parameters, $\sqrt{2}a_c$, $2a_c$ and $\sqrt{2}a_c$, with a_c the lattice parameter of the cubic lattice. In the case of $\text{La}_{1-x}\text{Ca}_x\text{MnO}_3$, the structure is orthorhombic for the parent material. Upon doping the average radii of the A and B site are reduced, however the structure remains orthorhombic for $x \rightarrow 1$, CaMnO_3 [2].

2.1.2 The electronic configuration

The electronic configuration of the Mn atom is $3d^5 4s^2$, with degenerate 3d and 4s levels. The degeneracy of the 3d shell is partially lifted when the ion is incorporated

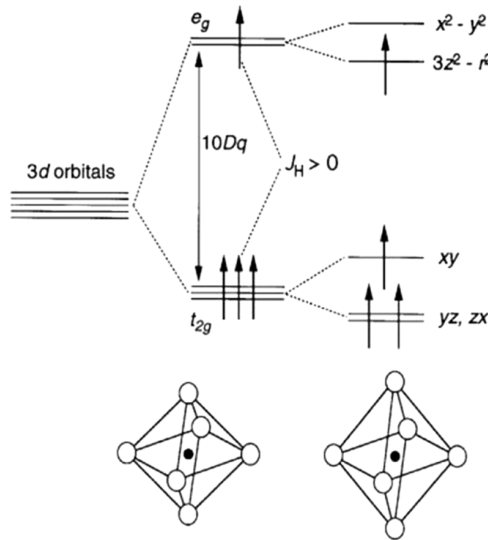


Figure 2.2 — Electronic configuration of Mn-ions in LaMnO_3 . From left to right: the degeneracy of the five 3d energy levels is partially lifted by the crystal field, into the lower energy triplet levels, t_{2g} and the higher energy doublet levels, e_g . The t_{2g} levels are half filled and for the Mn^{3+} ion one electron occupies the e_g level. J_H denotes the Hund's rule coupling between the electrons in the t_{2g} and e_g levels, which results in alignment of the spins. The presence of the electron in the e_g level leads to so-called Jahn Teller distortions of the oxygen octahedra which further lifts the degeneracy of energy levels. The different electron orbitals, which correspond to the energy levels, are indicated. The figure is taken from Tokura et al [3].

in a crystal lattice, which destroys the rotational invariance of the atom. The crystal field splitting results in formation of a t_{2g} triplet (d_{xy} , d_{yz} , d_{zx}) and an e_g doublet ($d_{x^2-y^2}$, $d_{3z^2-r^2}$), see Fig. 2.2. Theoretical calculations of the crystal field strength are reported by Dagotto et al [4]; values estimated from optical spectra are between 1 and 2 eV [5]. The Mn-ions have a partially filled 3d shell which is, in the case of Mn^{3+} , $3d^4$ and for Mn^{4+} , $3d^3$. The Hund's rules are a simple tool to determine which electron and spin configuration, in a multi-electron system, is the ground state. One of the rules dictates that the lowest energy state corresponds to the state with maximum spin angular momentum, S . The strong Hund's rule coupling between the

t_{2g} and e_g levels leads to the configuration $t_{2g}^3 e_g^1$ ($S = 2$, magnetic moment = $4 \mu_B$), for Mn^{3+} and t_{2g}^3 ($S = \frac{3}{2}$, magnetic moment = $3 \mu_B$), for Mn^{4+} . The superexchange interactions in the parent material $La^{3+}Mn^{3+}O_3^{6-}$ lead to so-called A-type antiferromagnetic ordering of the magnetic moments on the Mn^{3+} -sites. The metallicity of the material is determined by the competition between the strength of the inter-site hopping (responsible for band formation with bandwidth W), the electron-phonon coupling (Jahn-Teller distortions) and the on-site Coulomb repulsion U (for $W < U$, a Mott-Hubbard gap is formed between the occupied and unoccupied e_g -levels [6]). As a result the parent compound is an antiferromagnetic Mott insulator.

2.1.3 Jahn-Teller distortions

The crystal field splitting does not fully lift the degeneracy of the energy levels of the Mn-ion. The remaining degeneracy is lifted by the Jahn-Teller distortions of the oxygen octahedron around the Mn^{3+} -ion. The Jahn-Teller (JT) theorem states that a nonlinear molecule with a degenerate ground state is unstable; a geometric distortion lowers the overall energy of the molecule and lifts the degeneracy of the ground state (costs elastic energy, gains electronic energy). In LMO the strong JT distortions lead to cooperative static distortions throughout the lattice which results in orbital ordering at the Mn-site. Depending on the Mn - O bond lengths on either side of the anion this results in an antiferromagnetic (orbital ordered) ground state. The large value for U prevents delocalization of the e_g electrons. The static cooperative JT distortions results in a lowering of the energy of the Mn^{3+} -ion but the energy of the Mn^{4+} -ion, which is not a JT ion, remains unchanged. Therefore, hole doping disrupts the cooperative effect and leads to delocalization. In the doped crystal lattice, the 3d (e_g) orbitals of the Mn-ion overlap with the 2p orbitals of the oxygen ions [5, 7]. The overlap of the t_{2g} orbitals with the 2p orbitals of the oxygen is small. The hybridization results in the delocalization of the conduction (e_g) electron, it is smeared out over the Mn-O bond. This delocalization results in the formation of four covalent bonds [8]. The different JT modes, stretching and contracting of the Mn-O bonds (Q_2 and Q_3) can be degenerate in energy. This degeneracy can be removed by letting the octahedron resonate between the two stable configurations. In this way the Mn - O distances on either side of the oxygen are oscillating [8]. Assuming that changes in the electronic configuration of the Mn-ion occur on a much faster timescale than the nuclear vibrations and, that the two are strongly coupled, the response is adiabatic and is called quasistatic.

2.2 Competing phases and ordering phenomena

The insulating state of the parent compound can be changed into, for instance, a ferromagnetic metallic state by introducing doping. Replacing La^{3+} with Ca^{2+} introduces mixed Mn-valence, $(\text{La}_{1-x}^{3+}\text{Ca}_x^{2+})(\text{Mn}_{1-x}^{3+}\text{Mn}_x^{4+})$ and leads to a wide variety of structural, electronic and magnetic phases (Fig. 2.3). In this section we give an

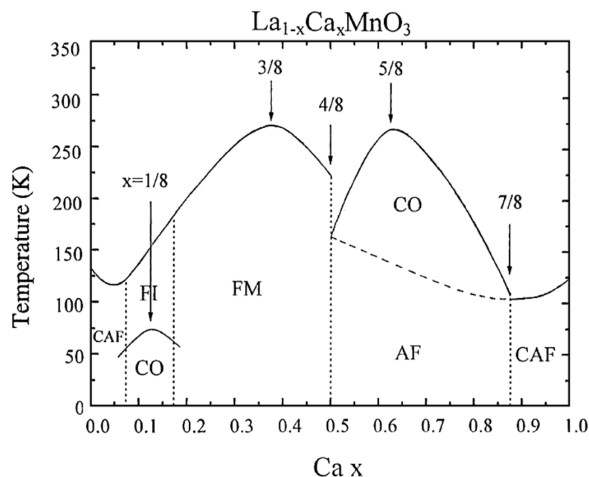


Figure 2.3 — Phase diagram of the material $\text{La}_{1-x}\text{Ca}_x\text{MnO}_3$. A wide range of physical properties is indicated as function of x (Ca-doping) and T (temperature). The acronyms in the figure are, PI: paramagnetic insulator (C)AF: (canted) antiferromagnetism, CO: charge ordering, FI: ferromagnetic insulator. Taken from ref. [4]

overview of the physical properties of $\text{La}_{1-x}\text{Ca}_x\text{MnO}_3$ for intermediate and high doping levels. In the case of intermediate doping, the striking feature of this material is the presence of a combined metal-insulator and ferromagnetic-paramagnetic (FM-PI) transition at transition temperature T_{MI} (section 2.2.1). At higher doping levels the material becomes charge and orbital ordered (section 2.2.2).

2.2.1 Intermediate doping

The electrical transport properties of a bulk $\text{La}_{0.7}\text{Ca}_{0.3}\text{MnO}_3$ single crystal shows a drop in resistance of a few orders of magnitude when it is cooled through the metal-insulator transition, $T_{MI} = 250$ K. Magnetization measurements show that this large resistance change is coupled to an onset in magnetization (see Fig. 2.4). Around the transition, a large reduction in resistance is induced by applying a high magnetic field,

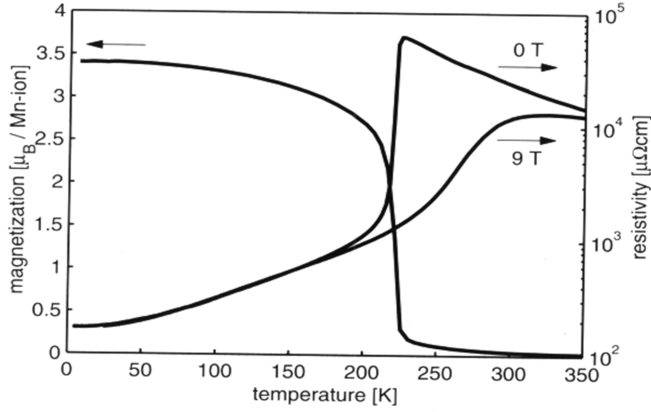


Figure 2.4 — (Right axis) resistance vs. temperature diagram of a bulk $\text{La}_{0.7}\text{Ca}_{0.3}\text{MnO}_3$ single crystal in 0 and 9 T applied magnetic fields. (Left axis) magnetization vs. temperature. Taken from [9].

this is called colossal magnetoresistance effect. The conduction mechanisms above T_{MI} (polaron hopping) and below T_{MI} (double exchange) are different as will now be discussed.

Polaron hopping

In the paramagnetic insulating state the conduction mechanism is similar to that of electrons which move through an ionic (polar) lattice. The Coulomb interactions with the ions cause a polarization of the immediate vicinity of the electron, and it drags this polarization cloud with it when it moves through the lattice. In the case of manganites this polarization cloud consists of lattice phonons, which exist only around the Mn^{3+} -ions, because of the electron-phonon coupling and the Jahn-Teller distortion (see Fig. 2.1) of the oxygen octahedron. The distortion creates a potential well for the e_g -electron, which has a self-trapping effect. The electron together with the lattice distortion is called a polaron. When enough energy is provided (through lattice vibrations) the polaron can hop to a neighboring Mn^{4+} , which is not a Jahn-Teller ion since it has an unfilled e_g -level [10]. Upon hopping the e_g -electron needs to drag along its lattice distortion. Consequently the conduction behavior above T_{MI} is thermally activated,

$$R = R_0 \exp\left(\frac{-E_A}{k_B T}\right) \quad (2.2)$$

with activation energy E_A [11]. The polaron is called small when the particular electron only distorts the lattice in its immediate vicinity. However, the distortions can extend across multiple lattice spacings creating a large polaron. If too large, the low temperature state of this system becomes a (cooperative Jahn-Teller) insulator.

Double Exchange Mechanism

Zener first described the low temperature magnetic ordering and conduction mechanisms in transition metals. He argued that the spin coupling (Hund's rule) between the incomplete d-shell (t_{2g}) and the conduction electrons (e_g) leads to ferromagnetic alignment of the spins [12]. In a second effort he presented the Double Exchange mechanism [13] as the low temperature conduction mechanism. It describes a two electron hopping process from the Mn^{3+} -ion to its neighboring Mn^{4+} -ion which is mediated by the $2p$ orbital of the oxygen ion in between. The hopping strongly de-

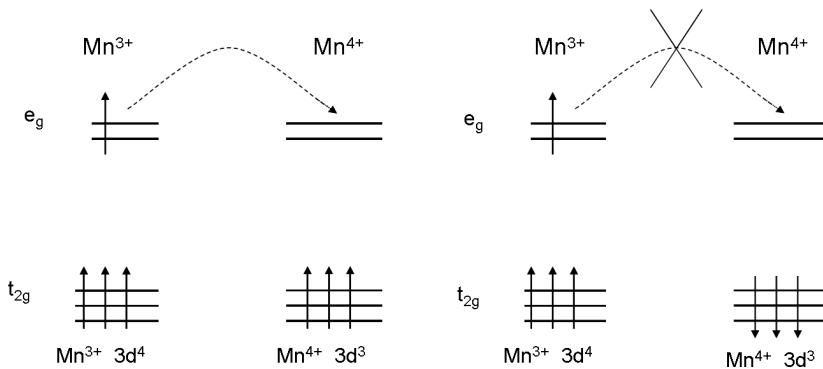


Figure 2.5 — Double exchange mechanism as proposed by Zener et al. [13]. Two electron hopping process between neighboring Mn-sites mediated by the oxygen in between.

pendes on the relative angle θ_s between neighboring spins and Anderson [14] showed that it can be denoted by an effective hopping parameter which is proportional to $\cos(\theta_s/2)$. As a result hopping is maximal if the spins on the Mn^{4+} -site are aligned with the spin of the conduction electron ($\theta_s = 0$) and completely forbidden in an antiferromagnetic state ($\theta_s = \pi$) (see Fig. 2.5).

Metal-insulator transition

It was realized by Millis et al. [15] that the disappearance of the spin scattering in the Double Exchange mechanism is not enough to explain the large resistance change in the transport properties of CMR-manganites. The metal-insulator transition for intermediate doping levels is caused by the competition between the electron-phonon interaction and the inter-site hopping parameter t_{eff} . The competition can be described by the dimensionless ratio,

$$\lambda_{eff} = \frac{E_{JT}}{t_{eff}} \quad (2.3)$$

between E_{JT} , the energy gained by the electron-phonon coupling without hybridization, and t_{eff} . The temperature dependence of λ_{eff} comes from the hopping parameter. This ratio would lead to insulating behavior above T_{MI} , due to electron localization and itinerancy below the transition. Furthermore, the buckling of the octahedra, and therefore the Mn-O-Mn bond angles and distances, are very important in determining the one electron bandwidth of the material,

$$W \propto \frac{\cos^2 \theta}{l_{Mn-O}^{3.5}} \quad (2.4)$$

with θ the bond angle and l_{Mn-O} the bond length. The large bandwidth, for instance in the material (La,Sr)MnO₃, results in a metal-insulator transition which is second order. However, for smaller tolerance factors (as in LCMO) the bandwidth is decreased and the corresponding loss of itinerancy results in a reduction of T_{MI} [3] and a stronger first order component of the transition. It is this closeness to a first order transition which is important for the remainder of this thesis.

The Colossal Magnetoresistance effect

Around the transition the PI and FM phases coexist, which results in an electronically inhomogeneous state. When a high magnetic field is applied, spins are aligned. As a result the metallic domains grow at the expense of insulating regions and the transition shifts to higher temperatures (see Fig. 2.4). Application of high magnetic fields leads to a resistance drop of a few orders of magnitude around the transition, the well known CMR effect.

2.2.2 Low and high doping: charge and orbital ordering

The tolerance factor, which causes the average tilt angles of the oxygen octahedra, determines the bandwidth or hopping parameter of the system. The JT distortions

(see section 2.1.3) are added to this effect and create additional local lattice deformations. In the case of the parent material, LaMnO_3 , this leads to long range order, i.e. cooperative static JT effect. The orbitals on the Mn^{3+} -sites are highly directional and orbital order occurs (see Fig. 2.6a), which leads to A-type antiferromagnetism. Long range order also occurs at higher doping levels. At $x = 0.5$ equal amounts of Mn^{3+} and Mn^{4+} are present in the material, causing the Mn^{3+} and Mn^{4+} to arrange themselves on alternate Mn-sites. The electron orbitals are also ordered, which results in a zigzag chain-like structure with ferromagnetic coupling in the direction of the ligands. Perpendicular to the ligands the superexchange interactions [8] lead to antiferromagnetic coupling. This is called the checkerboard (CE) [4] pattern which is shown in Fig. 2.6b (white spheres, Mn^{4+} and black spheres, Mn^{3+}). If the band-

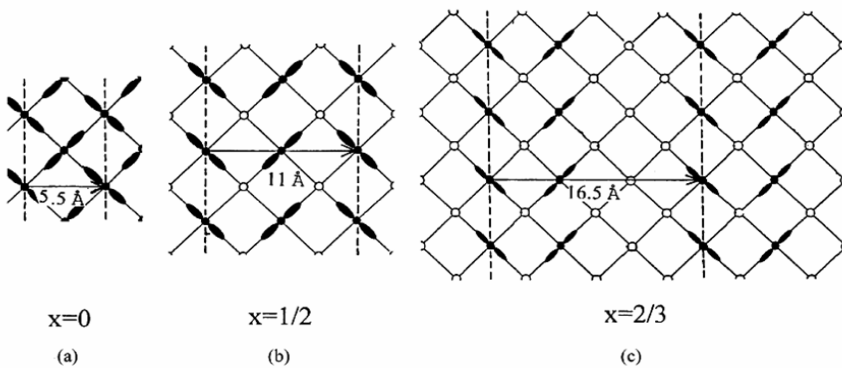


Figure 2.6 — Various types of charge and orbital order for different doping levels, x , in $\text{La}_{1-x}\text{Ca}_x\text{MnO}_3$. a) The ordered state in LaMnO_3 . b) The checkerboard (CE) type ordering for doping $x = 0.5$. c) Charge and orbital order for doping level $x = 2/3$. Taken from Dagotto et al. [4].

width (i.e. itinerancy) of the system is reduced, the charge-ordered state can occur over larger doping range (see Fig. 2.6c, for doping $x = 2/3$). From Fig. 2.6 it may seem that the charge ordering is always accompanied by orbital ordering. However, here we note that the temperature at which charge order sets in (T_{CO}) is not necessarily equal to the temperature at which orbital order starts to occur (T_{OO}).

2.3 Electronic phase control

The different phases, described in the previous sections are caused by various competing interactions. The small energy differences between these interactions can lead to electronically inhomogeneous states [16]. Several theoretical efforts have led to possible mechanisms to explain the inhomogeneity in manganites. For instance

Burgy et al [17] demonstrates the relevance of quenched disorder and cooperative effects. Furthermore, Ahn et al [18] have shown that the strong coupling between electronic and elastic degrees of freedom, i.e. epitaxial strain and lattice distortions, can be used to tune the multiphase state.

2.3.1 Epitaxial strain as a tuning parameter

In the past decade the experimental developments have led to the ability to grow manganite thin films of increasingly good quality. The lattice mismatch between film and substrate, which induces different strain states for various substrates, leads to tunability. The use of epitaxial strain in electronic phase control has already been demonstrated by Konishi et al [19]. In Table 2.1 we denote the different pseudocubic lattice parameters, a_s for various commonly used substrates; the bulk pseudocubic lattice parameter of $\text{La}_{0.67}\text{Ca}_{0.33}\text{MnO}_3$ (LCMO) is $a_b = 0.386$ nm and the lattice mismatch is given by $m = a_b - a_s/a_b * 100$ %. In epitaxial thin films, the imposed strain

Table 2.1 — We indicate the pseudocubic orientation and lattice parameter, a_s of several substrates which are commonly used. We also give the lattice mismatch of the substrate compared to the pseudocubic bulk lattice parameter of $\text{La}_{0.67}\text{Ca}_{0.33}\text{MnO}_3$, $a_b = 0.386$ nm. Note: for NGO (100) in pseudocubic notation is (110) in orthorhombic notation.

substrate	SrTiO_3	NdGaO_3	LaAlO_3
	(100)	(100)	(100)
a_s (nm)	0.391	0.387	0.379
m (%)	-1.29	-0.26	1.81

directly influences the Mn-O bond length and the Mn-O-Mn bond angles. For compressive strain (LaAlO_3) this can lead to enhancement of the transition temperature. In the case of SrTiO_3 , the introduction of tensile strain leads to enhancement of the electron-phonon coupling, which hampers band formation. As a result the transition temperature is decreased compared to the bulk value and suppression of ferromagnetism leads to a reduction of T_C [20]. Films grown on (almost) lattice matched substrates (NdGaO_3) and thickness dependencies show that strain relaxation results in enhancement of T_C towards the bulk value [21]. Lattice effects, similar to epitaxial strain, can also be induced by applying external pressure [22].

2.3.2 Disorder-induced effects

Sensitivity to (local) changes in the crystal structure provides disorder as another tool for phase tuning. Introducing doping into transition metal oxides results in random distribution of the rare earth and alkaline ions. Therefore, the doping inherently

causes crystallographic disorder. In CMR manganites, this leads to the tendency to form a phase separated state. However, several types of disorder can be (intentionally) incorporated into thin films. For instance, the application of epitaxial strain leads to incorporation of misfit dislocations [23] in $\text{Ba}_{1-x}\text{Sr}_x\text{TiO}_3$. Furthermore, Dörr et al. [24] shows that vacuum annealing LCMO after growth, leads to oxygen deficiency. Reduction in oxygen stoichiometry results in a reduction of manganese valence to Mn^{3+} , which changes the electrical transport properties dramatically. However, also other systems, such as charge ordered manganites, are sensitive to disorder. For instance, Yang et al. [25] studied the magnetic field induced melting of charge order in $\text{Pr}_{0.5}\text{Ca}_{0.5}\text{MnO}_3$. The introduction of disorder, through annealing and addition of a buffer layer $\text{YBa}_2\text{Cu}_3\text{O}_{7-\delta}$, results in a large decrease of the required melting field.

We will show in this thesis, that the sensitivity to external perturbations, such as magnetic fields, strain and electric fields provides a tool for electronic phase control in LCMO thin films. We use STO substrates, which contain unit cell high steps on the surface, to introduce additional crystallographic disorder in our thin films. Furthermore, we will show that going to micron-sized LCMO structures leads to novel behavior such as E-field sensitivity which we attribute to the occurrence of an electronically inhomogeneous state, and strongly nonlinear behavior in the transition which we attribute to the occurrence of an intervening charge ordered phase.

Bibliography

- [1] G.H. Jonker and J.H. Van Santen, *Physica* **16**, 337 (1950); Jonker G. H and Van Santen J.H., *Physica* **16**, 337 (1950)
- [2] R. Sopracase, G. Gruener, E. Olive, and J.-C. Soret, *Physica B*, **405**, 45 (2009)
- [3] Y. Tokura and Y.Tomioka, *C, J Mag. Mag. Mat.* **200**, 1 (1999)
- [4] E. Dagotto, T. Hotta, and A. Moreo *Phys. Rep.* **344**, 1 (2001)
- [5] J. M. D. Coey, M. Viret, and S. von Molnar, *Adv. Phys.* **48**, 167 (1999).
- [6] N. N. Kovaleva, A. V. Boris, C. Bernhard, A. Kulakov, A. Pimenov, A. M. Balbashov, G. Khaliullin, and B. Keimer, *Phys. Rev. Lett.* **93**, 147204 (2004); N. N. Kovaleva, A. M. Olés, A. M. Balbashov, A. Maljuk, D. N. Argyriou, G. Khaliullin, and B. Keimer, arXiv:0907.5098v1 [cond-mat.str-el]
- [7] Y. Tokura and N. Nagaosa, *Science* **288**, 462 (2000)
- [8] Goodenough, *Magnetism and the chemical bond*, John Wiley & Sons (New York - London - Sidney) 1963
- [9] S. Freisem Ph.D. thesis, University of Leiden, 1999
- [10] The Mn^{4+} -ion, although not a Jahn-Teller ion, can couple to the lattice through the so-called breathing mode (A.J. Millis, *Nature* **392**, 147 (1998)).
- [11] T.T.M. Palstra, A.P. Ramirez, S-W. Cheong, and B.R. Zegarski, P.Schiffer, J. Zaanen, *Phys. Rev. B*, **56**, 5104 (1997)
- [12] C. Zener, *Phys. Rev.* **81**, 440 (1951)
- [13] C. Zener, *Phys. Rev.* **82**, 403 (1951)
- [14] P. W. Anderson and H. Hasegawa, *Phys. Rev.* **100**, 675 (1955)
- [15] A. J. Millis, P. B. Littlewood, and B. I Shraiman, *Phys. Rev. Lett.* **74**, 5144 (1995)

-
- [16] M. Uehara, S. Mori, C. H. Chen, and S. -W. Cheong, *Nature* **399**, 560 (1999)
- [17] J. Burgy, A. Moreo, and E. Dagotto, *Phys. Rev. Lett.* **92**, 097202 (2004)
- [18] K.H. Ahn, T. Lookman, and A.R. Bishop, *Nature* **428**, 401 (2004)
- [19] Y. Konishi, Z. Fang, M. Izumi, T. Manako, M. Kasai, H. Kuwahara, M. Kawasaki, K. Terakura, and Y. Tokura, *J. Phys. Soc. Jpn.* **68**, 3790 (1999)
- [20] Z.Q. Yang, R. Hendrikx, J. Aarts, Y. Qin, and H. Zandbergen, *Phys. Rev. B.* **67** 024408 (2003)
- [21] J. Aarts, S. Freisem, and R. Hendrikx, and H.W. Zandbergen, *Appl. Phys. Lett.* **72**, 2975 (1998)
- [22] A. Arulraj, R. E. Dinnebier, S. Carlson, M. Hanfland, and S. van Smaalen, *Progress in Solid State Chemistry* **35**, 367 (2007)
- [23] K. Terai and M. Lippmaa, P. Ahmet and T. Chikyow, T. Fujii, H. Koinuma, and M. Kawasaki, *Appl. Phys. Lett.* **80**, 4437 (2002)
- [24] K Dörr, J M De Teresa, K-H Müller, D Eckert, T Walter, E Vlahov, K Nenkov, and L Schultz, *J. Phys.: Condens. Matter* **12**, 7099 (2000)
- [25] Z. Q. Yang, R. W. A. Hendrikx, P. J. M. v. Bentum, and J. Aarts, *Europhys. Lett.*, **58**, 864 (2002)

Chapter 3

Sample fabrication and characterization

As was described in the previous chapter the physical properties of the material (La, Ca)MnO₃ depend heavily on crystal structure. In epitaxial thin films the lattice parameters, i.e. Mn-O-Mn bond lengths and angles, of the manganite can be varied by choosing a suitable substrate with a corresponding lattice mismatch. In this chapter we describe the film growth and characterization of thin films grown on three different substrates, SrTiO₃ (STO) (tensile strain) with a misorientation of $<0.2^\circ$ in random directions which we denote as flat, NdGaO₃ (NGO) (lattice matched) and SrTiO₃ with misorientation of 1° towards the [010] direction. The misoriented substrate has unit-cell high steps on the surface with an average terrace length of ~ 20 nm. Here we define the nomenclature which we will use throughout this thesis to refer to our films. Films grown on flat STO are indicated by $L(d)$, with d the film thickness (rounded to the nearest integer value), films grown on misoriented STO by $L(d)_{mis}$ and films on NGO, by $L(d)_{NGO}$. This nomenclature provides every film with an unique sample name. We also describe the process developed to structure the films into microbridges, which is necessary to investigate properties intrinsic to (La, Ca)MnO₃ down to mesoscopic length scales. The thin film growth process is discussed in section 3.1. In section 3.2 we discuss the characterization methods, AFM (Atomic Force Microscopy) and XRR (X-ray reflectivity), which are used to determine morphology and film thickness. We also present the characterization of the lattice parameters with RSM (reciprocal space mapping). High resolution transmission electron microscopy (HR-TEM) and electron energy loss spectroscopy (EELS) are used to determine the microstructure and composition of our thin films as discussed in section 3.3. After characterization the films are structured into microbridges as presented in section 3.5. Section 3.6 describes the measurement equipment, and section 3.7 discusses how to overcome a specific problem that occurs when conventional Ar etching is used with STO substrates, namely that the substrate surface becomes conducting.

3.1 Thin film growth

We use the DC-sputtering technique to grow the films which are studied in this thesis. Here we briefly describe the sputtering and growth processes.

3.1.1 DC-sputtering

In the case of DC-sputtering the process chamber is filled with an inert gas, such as argon. This process gas is ionized by applying a voltage between the cathode (the target), and the chamber, which is grounded. The electric field near the target surface results in the emission of electrons which are accelerated away from the target surface. These electrons ionize the Ar gas and the resulting Ar^+ -ions are accelerated towards the target, creating material fragments (mainly atoms) upon impact. Depending on the Ar pressure a glow discharge ignites which leads to a stable plasma when a sufficient ionization rate is reached. The fragments of target material are deposited onto a substrate which is mounted near the target. The ionization efficiency due to the secondary electrons can be enhanced by placing a ring magnet underneath the target, which results in confinement of the electrons. This process is called magnetron sputtering. DC-sputtering only works for conductive materials. Insulating materials would build up surface charge during the process, which would screen the electric field and hence, the ion current would die off. In that case an AC current has to be supplied.

3.1.2 Reactive DC-sputtering

The above process is generally used for the growth of thin films; however, to grow perovskites oxygen is used as the process gas. This is called reactive sputtering since the oxygen reacts with the material fragments and is incorporated into the film during the growth. The oxygen content of the material is an issue; it is dependent on the oxygen pressure during growth and subsequent annealing steps. Reactive gasses can also form negatively charged ions, by splitting up into its constituents instead of ionizing the whole molecule. Therefore, the oxygen ions will be accelerated towards both the target and the growing film. This causes the material of the film to be back-sputtered towards the target. By tuning the oxygen pressure w.r.t. target-substrate distance this effect can be minimized. A high surface mobility of the material fragments that reach the substrate surface, is crucial to obtain an epitaxial thin film. For the formation of the compound as well as sufficient surface mobility of the atoms, a high temperature is required. For growth of the LCMO films we used a substrate temperature of 840 °C.

3.1.3 Growth process

All films were grown using the reactive DC-sputtering technique. The target has a nominal composition of $\text{La}_{0.67}\text{Ca}_{0.33}\text{MnO}_3$ (LCMO) and the films are grown on STO and NGO substrates. Typical substrate dimensions are $10 \times 10 \text{ mm}^2$ with a thickness of 0.5 mm. The substrate is glued on a heater with Silver Paste Plus, which is dried at $300 \text{ }^\circ\text{C}$ for 1h. Side plates, which are mounted around the substrate, ensure better temperature homogeneity near the edges of the substrate. Before starting the growth a base pressure around 10^{-4} Pa is reached. Pure oxygen is let into the system at a pressure of 300 Pa which is regulated and maintained by the rotation speed of the turbopump. The sputtering current is 350 mA and after heating the substrate to $840 \text{ }^\circ\text{C}$, the substrate is rotated above the plasma and growth is timed. Typical thicknesses for our films vary between 7-50 nm with a growth rate of approximately 0.8 nm/min. Here we note two parameters that are important in determining the quality of the film growth. One is the growth rate. When the film is grown in "slow" mode (rate $< 0.6 \text{ nm/min}$), the quality of the film growth is unstable, which leads to many different morphologies (very granular, different shaped holes, see Fig. 3.1) and different transport properties (for example the absence of the metal-insulator transition). A second

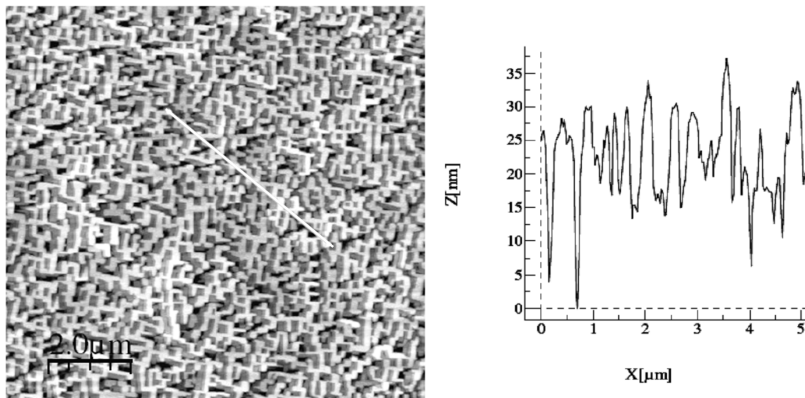


Figure 3.1 — (Left) AFM image (scan size: $10 \times 10 \text{ } \mu\text{m}^2$) and (right) profile of 75 nm LCMO film on a STO substrate as an example of morphology due to slow growth rate. Scale bar: $2 \text{ } \mu\text{m}$.

issue that has to be taken into account is the aging of the target. It appears that with time the growth rate of the target goes down. A solution would be to keep decreasing the target-substrate distance, which cannot continue indefinitely. We have found that the introduction of water during the conditioning of the target improves the film qual-

ity. We believe that the water adheres better to the target and results in an increase of oxygen ions during conditioning. It has been reported before [1] that addition of water during growth of $\text{Y}_1\text{Ba}_2\text{Cu}_3\text{O}_{7-\delta}$ films helps to prevent and even reverses the aging of the target.

3.2 Sample characterization

Both before and after growth substrate and film are characterized using an Atomic Force Microscope (AFM). Furthermore, thickness of the film and in- and out-of-plane lattice parameters are measured with x-ray reflectivity measurements. Some films were investigated by Reciprocal Space Mapping (RSM).

3.2.1 Morphology and film thickness

Before the film is grown we check the quality of the substrate with an AFM. One issue to be discussed is the surface termination of the STO, which can be either a TiO_2 - or an SrO-layer. Commercial substrates have mixed termination but can be treated to become singly terminated, with the TiO_2 surface easier to fabricate and more stable. Some of the misoriented STO substrates underwent a surface treatment to obtain a TiO_2 termination; the other substrates have mixed termination. Whether this is of influence on the film properties which are investigated in this thesis will be discussed later. In Fig. 3.2 we show typical topography and profiles of two STO substrates with misorientation of 1° of which the one in Fig. 3.2 (right) is singly terminated. From the profiles it becomes clear that both substrates have terraces with an average length of around 20 nm. However, there is also a clear difference. The step height on the unterminated STO varies from half to a full unit-cell (~ 0.4 nm) while the terminated STO only shows unit-cell high step edges. Typical AFM results for LCMO thin films on both flat STO and unterminated 1° miscut STO are shown in Fig. 3.3.

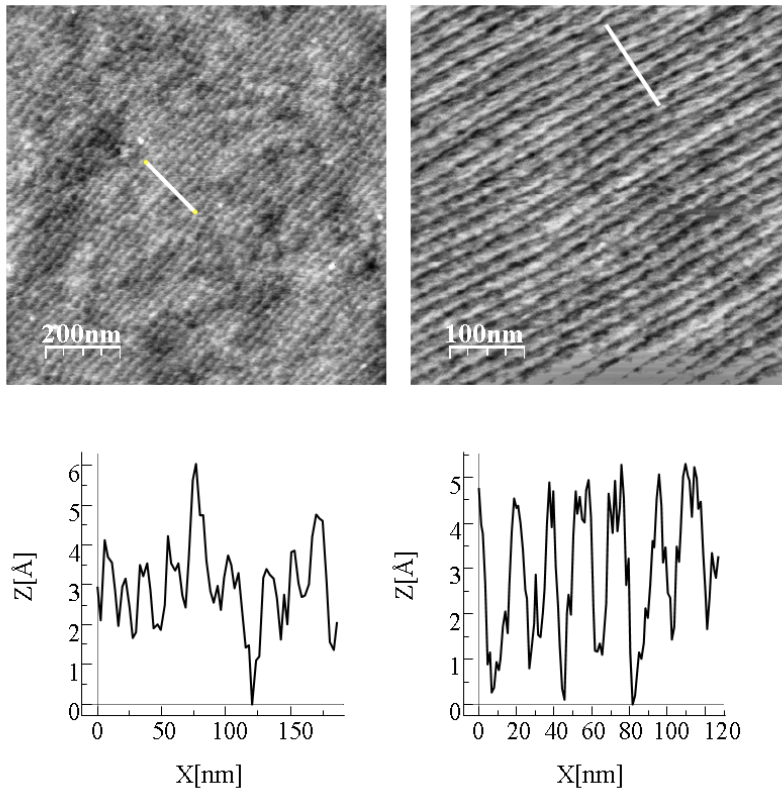


Figure 3.2 — AFM images of STO substrates and corresponding profiles of (left) untreated STO (scale bar: 200 nm) and (right) TiO₂ terminated STO (scale bar: 100 nm); both substrates have a misorientation of 1° towards the [010] direction.

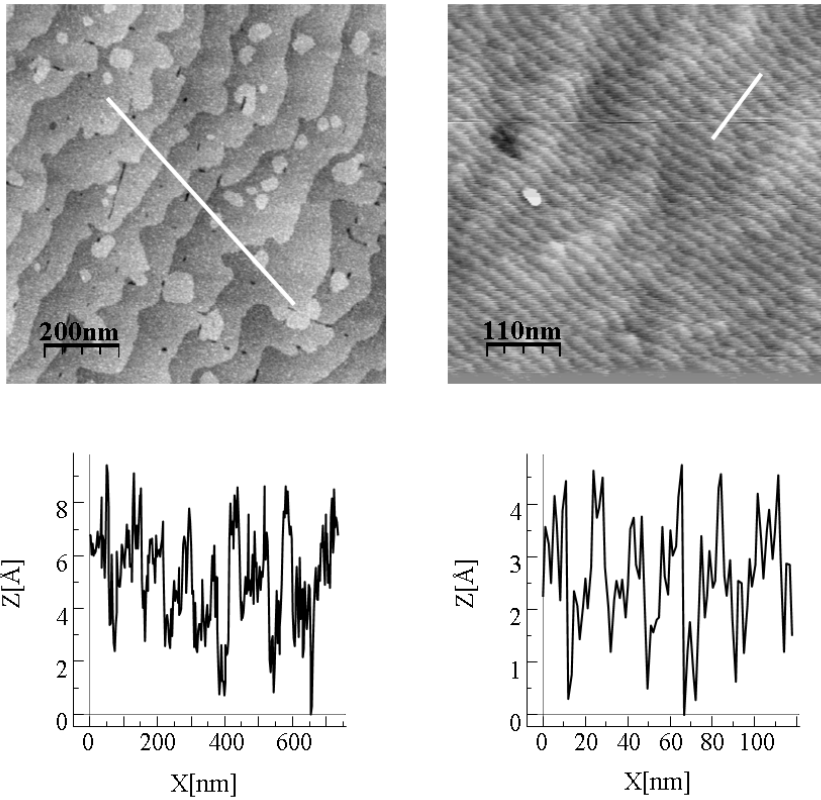


Figure 3.3 — AFM images of LCMO thin films and corresponding profiles of (left) 15 nm LCMO on flat STO, L(15) (scale bar: 200 nm) and (right) 7 nm of LCMO on untreated STO with a misorientation of 1° , L(7)_{mis} (scale bar: 110 nm).

All films show clear unit-cell high step edges. The films grown on flat STO show an average terrace length of 75 nm and the films grown on misoriented STO show an average terrace length of 20 nm, identical to the terrace length of the substrate.

The thickness of the LCMO films was determined by x-ray reflectivity (XRR) measurements, from which we determine growth rate of the sputtering process. The average growth rate of our LCMO thin films is 0.8 nm/min, which results in films with roughness of the order of the dimensions of the unit cell. An example of an

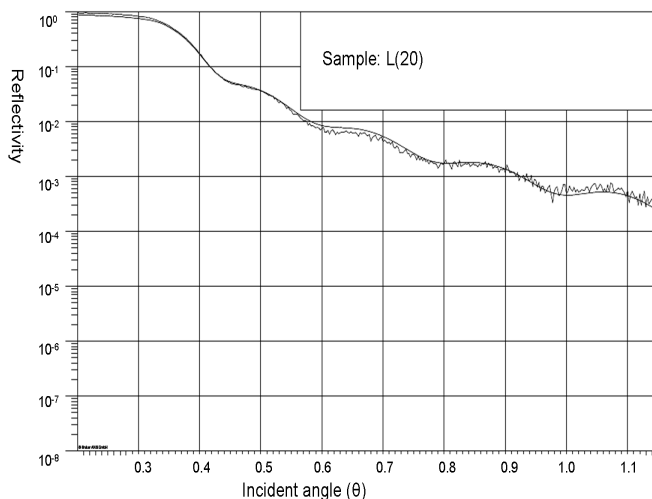


Figure 3.4 — Typical XRR measurement for thickness determination of a LCMO thin film. Theta is the angle of incidence and the thickness is determined from the period of the oscillations.

XRR measurement to determine the film thickness is given in Fig. 3.4. The thickness is calculated from the period of the oscillations, which in this case is $20 \text{ nm} \pm 0.2 \text{ nm}$.

3.2.2 Reciprocal space mapping

For several films the lattice parameters were determined through RSM around certain reflection spots. The RSM experiments were performed at Twente University by J. Boschker in the Inorganic Material Science group of Prof. Dr. D. Blank. The measurements were done with a Bruker D8 discoverer, equipped with a monochromator ($\lambda = 1.5406 \text{ \AA}$) and a Vantec-1 array detector. We have scanned reciprocal space around the reflection spot with indices (103) and the spots related by symmetry (013), ($\bar{1}03$) and ($0\bar{1}3$). The scattered intensity vs. the scattering vector, for

two different samples, is plotted in Fig. 3.5 (top: L(20); bottom: L(10)). The scans

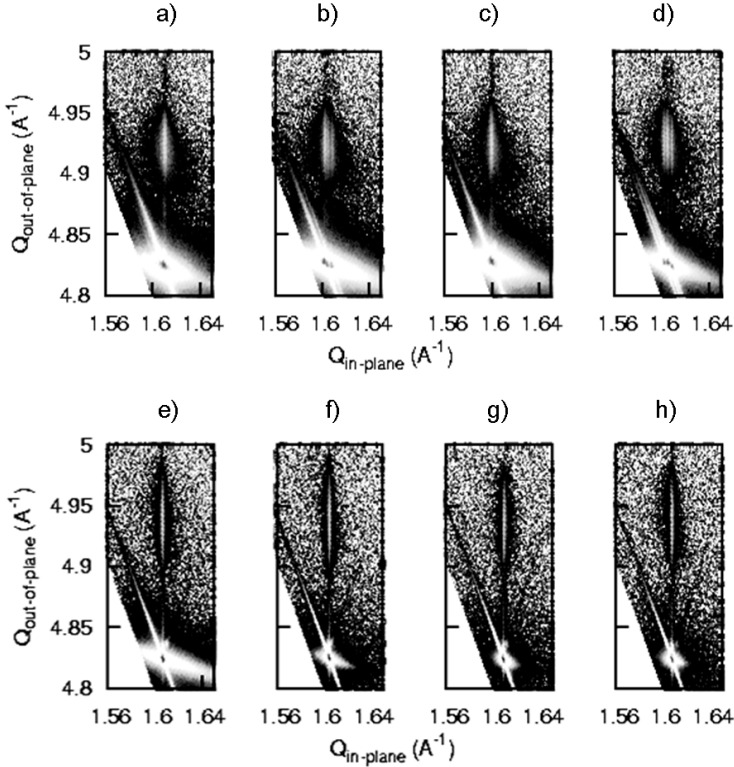


Figure 3.5 — The RSM-plots of two samples are shown for reflections (103) (a and e), (013) (d and f), ($\bar{1}03$) (c and g) and (0 $\bar{1}3$) (d and h). Graphs a)-d): L(20), graphs e)-h): L(10). For each graph two peaks are visible, the strong peak at the bottom (at 1.6 \AA^{-1} and 4.82 \AA^{-1}) is caused by the STO substrate and the weaker peak at the top (around 1.6 \AA^{-1} and 4.94 \AA^{-1}) is caused by the LCMO film.

show two peaks; the peak at $Q_{in-plane} = 1.6 \text{ \AA}^{-1}$ and $Q_{out-of-plane} = 4.82 \text{ \AA}^{-1}$ corresponds to the STO substrate. The other peak (around 1.6 \AA^{-1} and 4.94 \AA^{-1}) is caused by the LCMO film. The RSM-plots show that the films have an in-plane parameter equal to that of the substrate ($a_s = 3.91 \text{ \AA}$), i.e. the films are epitaxial and strained. The film peaks are well defined with a small spread in the in-plane parameter. The spread for the out-of-plane parameter (a_{out}) is larger and increases when film thickness is reduced. The value of a_{out} is determined from the relative distance between the STO peak and LCMO peak positions and is plotted as function of film thickness in Fig. 3.6. The epitaxial coupling to the substrate leads to

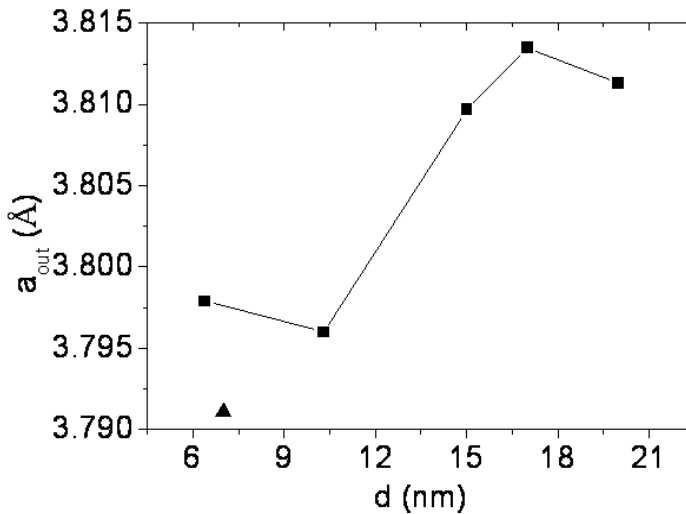


Figure 3.6 — Out-of-plane lattice parameter (a_{out}), determined from the relative distance between the STO and LCMO peak positions, plotted vs. film thickness d . Squares: films grown on flat STO; triangle: film grown on 1° misoriented STO.

in-plane elongation and out-of-plane compression of the LCMO unit cell which indicates that the film is fully strained. Furthermore, a_{out} shows a thickness dependence, the unit cell becomes more compressed when film thickness is reduced. Since the electrical transport properties of the films are highly dependent on the lattice (Mn-O bond lengths and angles), the observed changes in the lattice parameter may cause a thickness dependence in the transport properties.

3.3 Microstructure and Mn valency

We have characterized the microstructure, the atomic composition, and the Mn-valence state of LCMO thin films using the HR-TEM and EELS techniques. The measurements presented in this section were all performed by M. Porcu at Delft University in the HREM group of Prof. Dr. H. Zandbergen. We will show results of LCMO films grown on three different substrates, STO (flat), STO (1° , untermi- nated) and NGO. TEM specimens were prepared according to a standard cross-section preparation method. Before insertion into the microscope, the specimens were plasma-cleaned for 1 minute to prevent carbon contamination during the exper-

iments. The analysis was performed with a FEI TITAN equipped with a spherical aberration (C_s) corrector and a High Resolution Gatan Image Filter (HR-GIF) operated at 300kV. EELS data were collected in scanning TEM (STEM) mode with a probe size of about 0.2 - 0.5 nm. The spectra were acquired by probing the same region only once to reduce the beam damage. The energy dispersion was 0.1 eV/channel for the Zero Loss Peak and 0.2 eV/channel for the Mn L-edge to obtain more signal.

3.3.1 Microstructure

The perovskite crystal structure of the films is close to cubic with lattice parameter $a_c = 0.39$ nm, but due to small rotations of the oxygen octahedra it becomes orthorhombic (space group: Pnma). We observed that throughout the films the bulk Pnma structure is present with lattice parameters of $\sqrt{2}a_c$, $2a_c$ and $\sqrt{2}a_c$. HR-TEM investigations on 3 specimens for each film confirmed that the films are epitaxial. Several HR-TEM images are shown in Fig. 3.7. The images are manipulated (see caption) to emphasize the presence of defects (i.e. misfit dislocations). For most films, the b axis was found to be parallel to the interface normal (with length $2a_c$ in pseudocubic notation). We did not observe any antiphase boundaries (shift in periodicity of b -axis with a_c) or any domain type disorder w.r.t. the b -axis which is in line with previous reports [2]. The disordered layer visible at the top surface of the thin film is glue used during preparation of the sample. The HR-TEM image shown in Fig. 3.7a (sample L(6)) is a typical image for films grown on a flat STO substrate. However, for one sample L(10), shown in Fig. 3.7b, the film and also the substrate fringes are not very clear. The white circle indicates a region where fringes are more visible. The lines in the image clarify the apparent orientation of the crystal lattices of the film and the substrate. As will be shown later this film has deviating properties compared to the typical film on flat STO. Although this is not clear from Fig. 3.7b we surmise that the film might have a deviating orientation w.r.t. the substrate lattice. We also observe that films grown on 1° misoriented STO (Fig. 3.7c) are epitaxial with no clear influence of the step edges on the microstructure of the LCMO film. We also do not observe any misfit dislocation at the film-substrate interface in any of the films which are shown in Fig. 3.7.

3.3.2 Mn-oxidation state and elemental composition

We have used EELS to investigate the composition and the Mn-oxidation state across the thickness of our thin films. In an EELS measurement the sample is exposed to an electron beam with a well defined (small range of) kinetic energies. While the

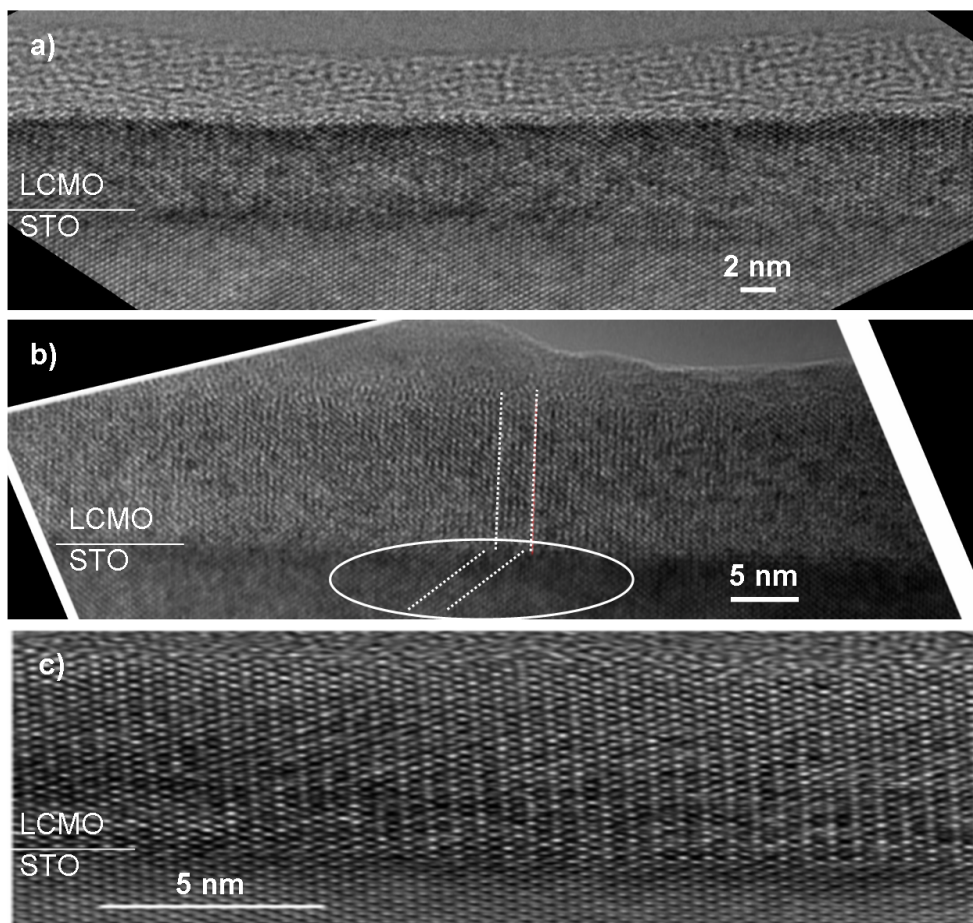


Figure 3.7 — HR-TEM micrographs of LCMO films on STO. a) L(6); b) L(10); c) L(7)_{mis}. Scale bars are indicated. To emphasize the presence of defects the images are blurred 10 pixels in the vertical direction and 1 pixel in horizontal direction and compressed in the vertical direction. The lines in b) are indicative of the orientation of the crystal lattice of the film and the substrate.

electrons go through the sample, inelastic interactions (i.e. atom core loss, inner shell ionization) result in the loss of kinetic energy, which can be measured using an electron spectrometer. An EELS spectrum consists of a Zero Loss peak (ZLP), and subsequent peaks at lower energy corresponding to different losses due to interaction with the sample. The obtained EELS data were corrected for specimen thickness [3] (it influences the ratio between intensities of ZLP peak and the rest of the spectrum). From the data it can be assumed that the elemental composition will not have any

dependence on the specimen thickness (for more details on the EELS measurements, see [4]). Since the only interest is to qualitatively monitor the changes across the film, the cross section was taken as a constant. By acquiring the ZLP, Mn L-edge and the La K-edge at 100 eV and calculating the ratio between the integrals, the Mn-valence and the elemental concentration across the film thickness were obtained. Manganese valence retrieval involves the acquisition of several Mn L-edge spectra across the film from the interface towards the surface. An example of an EELS spectrum is given in Fig. 3.8. The L_2 and L_3 peaks are indicated which correspond to the energy loss due to the presence of Mn^{4+} and Mn^{3+} -ions respectively. The L_{32}

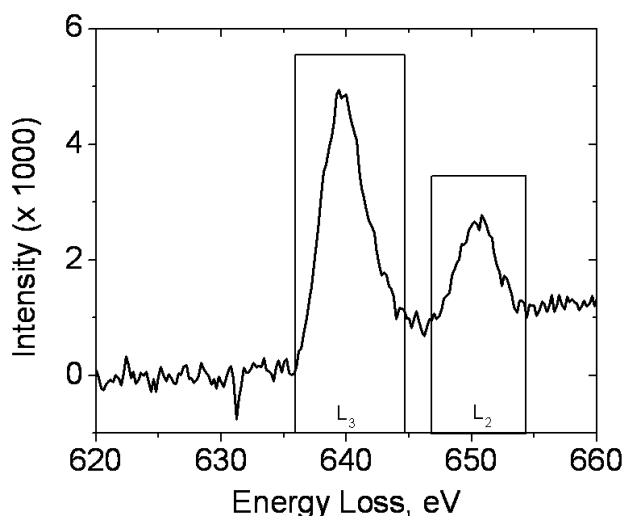


Figure 3.8 — Example of a EELS spectrum with the Mn L_2 and L_3 peaks indicated. The L_{32} ratio is determined from the integrated intensities ratio.

ratio (Mn-valence) is determined from the integrated intensities ratio L_3/L_2 . Ratios of 2.1 and 2.7 correspond to Mn^{4+} and Mn^{3+} , respectively; the calculated valence for $La_{0.7}Ca_{0.3}MnO_3$ is 3.3+ for bulk specimens [5]. In Fig. 3.9 the calculated L_{32} ratio is shown for several films grown on STO; three regions can be discerned. At the film surface (interface with vacuum) the Mn-valence is reduced towards 3+. In the bulk of the film, particularly visible in L(47), the L_{32} ratio indicates a Mn-valence close to 3.3+, similar to the value for bulk LCMO. Close to the interface with the STO substrate a reduction in Mn-valence is observed. With the probe placed on the first layer the valence is equal to 3.2+ in both L(6) and L(47). The presence of this

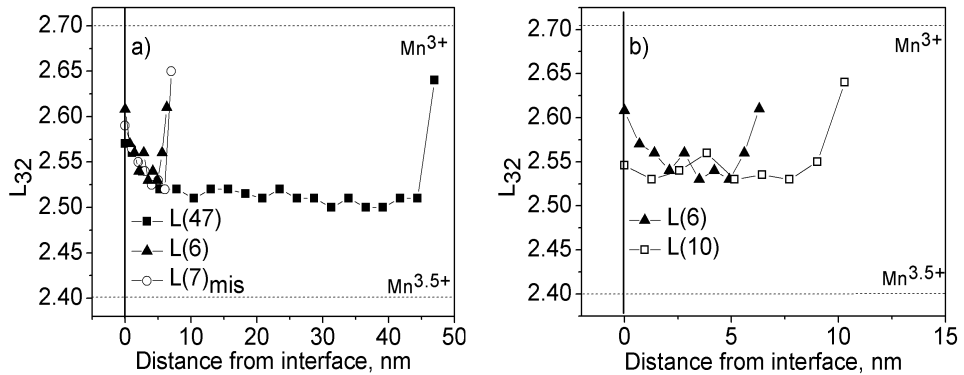


Figure 3.9 — The calculated L_{23} ratio from the EELS spectra. a) Results on three samples: L(6) and L(47) on flat STO and L(7)_{mis} on miscut STO. b) Results on L(10) (the results for L(6) are shown for comparison). The drawn lines are guides to the eye. The dashed lines indicate the L_{32} values which correspond to Mn^{3+} and Mn^{4+} respectively. The solid line indicates the substrate-film interface.

reduction is typical for our LCMO films grown on STO substrates, but the extent of the reduction varies between 2 - 5 nm for different films. In Fig. 3.9a we also show the L_{32} ratio for a film grown on STO with a 1° misorientation, L(7)_{mis}. The step edges on the STO surface appear to have no significant influence on the Mn-oxidation state near the substrate interface. Therefore, these properties are general features of LCMO films grown by sputtering on STO substrates. However, in Fig. 3.9b we show that sample L(10) did not show the reduced ratio at the substrate interface for which the precise cause remains unclear. The deviating Mn-valence might be correlated with cation segregation. Therefore, we also used EELS to map the elemental composition across the films. As shown in Fig. 3.10a, the composition (for the most part) is close to that of the sputtering target. The figure shows all elements of the films as well as the Ti^{4+} content. The apparent interdiffusion of Ti^{4+} into the film is caused by the limited resolution (determined by the beam size) of the measurement. For sample L(47) (see Fig. 3.10b), we did observe La enrichment near the film-substrate interface. However, since the results for all other samples did not show such segregation, it is likely that the observed La-enrichment is not correlated with the observed Mn-valence reduction.

Another question is whether the valence reduction at the interface is caused by strain. We therefore investigated the Mn-valence profile and elemental composition in LCMO films grown on NGO substrates. The results, plotted in Fig. 3.11, show

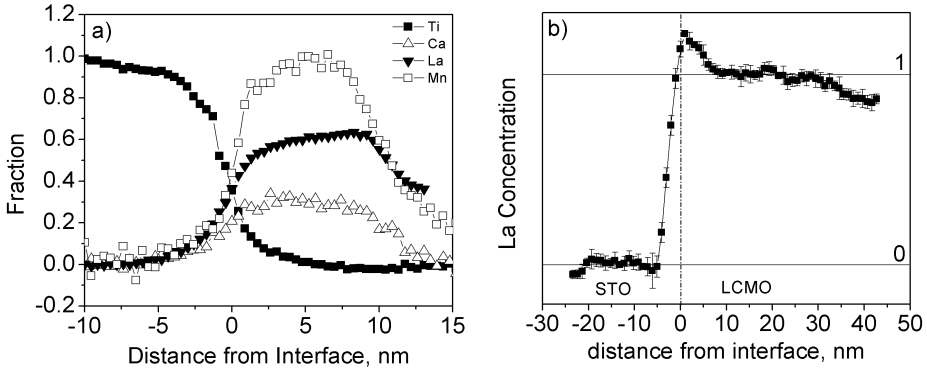


Figure 3.10 — a) Typical elemental composition of sample L(10). b) La-concentration across sample L(47). The graph is the average of three scans (each 15 nm apart) and the standard deviation is given for each point.

that also for films grown on NGO substrates an increase of the Mn^{3+}/Mn^{4+} ratio is observed at the substrate interface. Similar to films on STO there is no cation

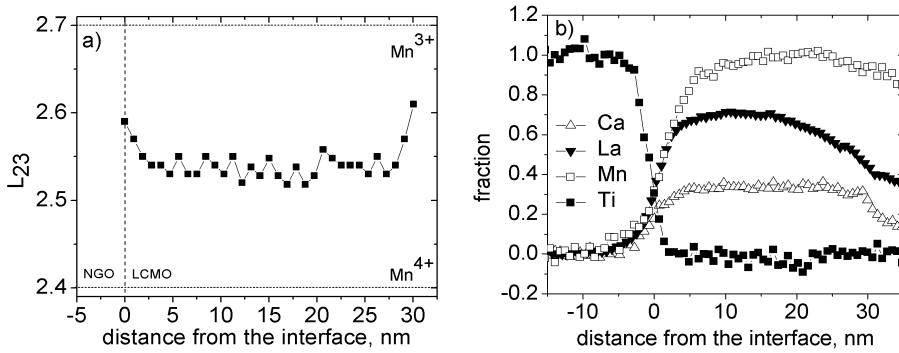


Figure 3.11 — a) The L_{32} ratio across the $L(30)_{NGO}$. b) Elemental composition of the same sample.

segregation for the films on NGO substrates.

3.3.3 Discussion

We find that LCMO grown on STO substrates is orthorhombic. The lattice parameters show that all films are coherently strained, with the in-plane lattice parameter equal to that of the substrate. Furthermore, we observe a thickness dependence for the out-of-plane axis; it is more compressed when the film thickness becomes small. We have also measured the Mn-valence and composition profiles across the film thickness. In the bulk of the films the Mn-valence is 3.3+ as expected for $\text{La}_{0.67}\text{Ca}_{0.33}\text{MnO}_3$. Therefore, we conclude that our films have correct oxygen stoichiometry (not deficient). The films do show a reduced valence value at the interface with vacuum which is probably caused by oxygen deficiency of the film surface (after growth the sample is cooled in vacuum). As a result the $\text{Mn}^{3+}/\text{Mn}^{4+}$ ratio needs to increase to compensate for the overall less negative charge. The films also show a reduced Mn-valence near the film-substrate interface (also observed in $\text{La}_{0.7}\text{Sr}_{0.3}\text{MnO}_3/\text{STO}$ [6]) which is not caused by oxygen deficiency. Since the film is grown at high temperature, diffusion of Ti^{4+} into the film could occur. The presence of the Ti^{4+} introduces a higher charge and as a result the $\text{Mn}^{3+}/\text{Mn}^{4+}$ ratio has to increase to compensate. Characterization of the elemental composition (see Fig. 3.10) and experiments reported by others [7] show that interdiffusion does not occur beyond a few atomic planes. The EELS analysis of the elemental composition show that in general the films have a composition close to that of the sputtering target. It is likely that the deviating Mn-valence is not associated with cation segregation. Since films grown on NGO show similar Mn-valence profiles the reduction appears to depend on the epitaxial relation between film and substrate. A question is whether the Mn-valence at the interface is affected by the termination of the substrate. In the case of STO substrates the termination can be $\text{Sr}^{2+}\text{O}^{2-}$ or $\text{Ti}^{4+}\text{O}_2^{4-}$, both terminations are neutral. The manganite growth can start with either a $[(\text{La}_{0.7}\text{Ca}_{0.3})\text{O}]^{0.7+}$ layer (LaO has charge 1+ and CaO is neutral) or a MnO_2 layer which can have charge 1- or be neutral depending on the Mn-valence state. We use substrates with mixed termination but it is not obvious that the charge in the first layer will average out (locally one termination could be dominant). A charge mismatch could arise (Madelung potential) across the LCMO-STO interface. The reduction of the Mn-valence at the interface shows that growth starts with the $[(\text{La}_{0.7}\text{Ca}_{0.3})\text{O}]^{0.7+}$ layer and that the interface polarization leads to a charge compensation layer with varying thickness (2 - 5 nm); the variation could be caused by different TiO_2/SrO termination ratios of the substrate surfaces. This also explains the absence of Mn-valence deviations for films on (110) STO, as reported by Estradé et al [8]. The termination layer of (110) STO is either $\text{Sr}^{2+}\text{Ti}^{4+}\text{O}^{2-}$ (total charge: 4+) or O_2^{4-} . The first layer of the film would be either $\text{La}^{3+}\text{Mn}^{3+}\text{O}^{2-}$ or $\text{Ca}^{2+}\text{Mn}^{4+}\text{O}^{2-}$, which both have a total charge of 4+, or O_2^{4-} . The result is that

LCMO (110) grown on STO (110) would not have a charge mismatch between film and substrate and therefore does not show a Mn-valence reduction at the substrate interface. The similar Mn-valence profiles in films on NGO substrates are explained in the same way. We use NGO (100) (pseudocubic notation) which has either $\text{Nd}^{3+}\text{O}^{2-}$ or $\text{Ga}^{3+}\text{O}_2^{4-}$ termination layers. Again the termination is mixed but does not necessarily lead to an average charge close to 0. The film, LCMO (001) will start the growth with a layer with charge $\pm(1-x)$ (x is the Ca-doping) as described above. The resulting Madelung potential again leads to the observed Mn-valence profiles. The only sample for which the Mn-valence reduction is absent (sample L(10)) possibly shows a deviating film orientation w.r.t. the STO substrate. It is not a priori clear why there is no charge mismatch for this sample since the STO would be neutral and the first film layer should still have a charge. One could imagine that the growth started with a CaMnO_3 layer for which the charge mismatch with the substrate would indeed be equal to 0. The resolution of the EELS measurement to determine elemental composition would be insufficient to detect such a small Ca-segregation at the STO interface. We were unable to further investigate this effect since the occurrence of the compensation layer is a general feature of the LCMO thin films. Furthermore, we have observed that the presence of unit-cell high steps on the STO surface do not significantly influence the microstructure or the Mn-valence profile of the film.

3.4 Summary

The characterization of our LCMO thin films on STO/NGO substrates led to several observations which we summarize here. All films which are grown on STO substrates are coherently strained. In addition we observe a thickness dependence of the out-of-plane axis with decreasing film thickness. Important to note is the absence of oxygen deficiency in the bulk of our thin films which we observed by monitoring Mn-valence across the film thickness. However, we do observe a Mn-valence reduction at the film-substrate interface which cannot be associated with cation segregation. It appears to be a generic feature of our LCMO thin films grown on STO and NGO substrates. The effect is most probably caused by the charge mismatch between the substrate termination layer and the first layer of the film. We surmise that this effect can be tuned by varying the orientation of the substrate. The question arises how this compensation layer would affect the transport properties of the films. It is not a priori clear whether this interface layer would still be ferromagnetic metallic. The transport properties of these thin films are presented in the next chapter.

3.5 Patterning thin films

In this thesis we present the magnetotransport properties of unpatterned LCMO thin films as well as micron-sized structures. The fabrication process of the LCMO microbridges consists of two electron beam lithography steps. The first step involves creating a resist mask (MaN-2405) for the microbridge with four small leads. The sample is etched using Ar-ions which sputter away the film that is not covered by the mask (beam current: 10 mA, beam voltage: 350 V). After cleaning, a LCMO microbridge is left. However, special care has to be taken during the Ar-ion etch process step. If this step is not timed exactly, it damages the substrate surface. This problem and its solution is presented in section 3.7. The second e-beam step is necessary to attach four macroscopic Au/MoGe [9] contacts to the LCMO structure. This is done using a lift-off technique. First a bilayer of PMMA/MMA resist is spun on top of the LCMO structure and the contact structure is written into this resist stack with the e-beam. Since positive resist is used, all exposed resist is dissolved upon development of the sample. An additional cleaning step with a low energy oxygen plasma can be used to remove any residue left by the resist. The Au/MoGe bilayer can be sputtered into the contact structure which is present in the resist mask. After sputtering the resist is dissolved with acetone, which removes all resist and excess Au from around the contact structure. An overview of this fabrication process is given in Fig. 3.12. Films on NGO substrates can only be patterned using a single e-beam lithography

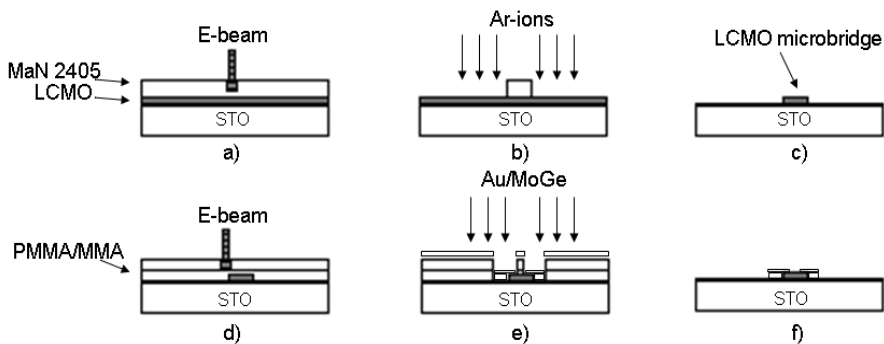


Figure 3.12 — Overview of the microstructuring process of the LCMO thin films. a) A layer of MaN-2405 resist is exposed by the electron beam. b) The excess LCMO around the resist mask is etched away by Ar-ions. c) The microbridge after etching and cleaning. d) E-beam exposure of PMMA-MMA resist bilayer to fabricate contact structure. e) After development the Au/MoGe is sputtered into the contact structure. f) The LCMO microbridge after the removal of excess Au/MoGe with the lift-off technique.

step. Patterning Au contacts onto a NGO substrate is impossible due to charging of the substrate. This means that both the microbridges on NGO and the macroscopic contacts consist of LCMO. An image of a typical structure is given in Fig. 3.13.

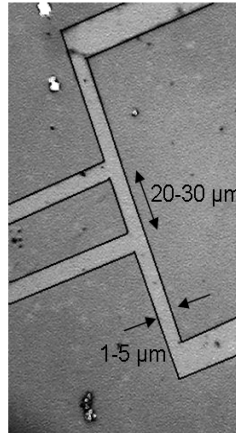


Figure 3.13 — Typical structure patterned in a LCMO thin film on a STO/NGO substrate.

3.6 Measuring thin films

We measured the transport properties of unstructured films as well as microbridges. The electrical contacts are made of indium which are pressed onto the contact pads. The samples are measured using a four probe configuration which should exclude any contribution from the contact-film interfaces (see section 3.7). For every sample, current-voltage (I-V) characteristics are measured in the temperature range 20 - 300 K in $B = 0$ T and $B = 5$ T. Furthermore, low field magnetoresistance is measured to study the magnetic domain formation in these microbridges. Temperature and field regulation were done in a PPMS (Physical Properties Measurement System) from Quantum Design which has a temperature range of 2 - 400 K and a field range of ± 9 T. The I-V's are measured using external current sources and nanovoltmeters. The current sources have a voltage limit of 105 V and the nanovoltmeter is used up to a range of 10 V (internal resistance > 10 G Ω), in autoranging mode. Furthermore, magnetic properties were measured using a MPMS (Magnetic Properties Measurement System, Quantum Design) in a temperature range of 5 - 300 K and in a magnetic field range of ± 5 T.

3.7 Conducting STO: problem and solution

Microbridge fabrication as described in section 3.5 enables us to measure current effects intrinsic to LCMO down to (sub)micron scales. However, special care has to be taken in the structuring process. The commonly used Ar-etching technique easily damages the STO substrate, which results in a conducting surface layer after etching [10]. Current leakage through this layer interferes with the transport measurements and obscures any intrinsic current effects of the LCMO. We will show here that this problem can be overcome by a brief oxygen plasma treatment. The resulting data also allow a discussion of the possible effects caused by Joule heating in the microbridge.

3.7.1 The effect of Ar-ion etching on STO

The epitaxial LCMO films presented in this section have a typical thickness of 8 nm and were grown on (001) STO substrates. The substrate surface was treated to have single termination of TiO_2 , and had a misorientation of 1° towards [010]. The presence of step edges on the substrate possibly leads to local variations in crystallographic disorder which could lead to conductance anisotropy w.r.t. the step edges. To investigate the influence of the misorientation on transport properties of LCMO thin films, we fabricated microbridges with a width of $5 \mu\text{m}$ and distance between the voltage contacts of $16 \mu\text{m}$. The orientation of the bridges is perpendicular to the step edges of the substrate. The films are etched with a calibrated etch rate of 0.31 nm/s . The films are overetched by 14 s, in order to be certain to remove all of the film. I-V characteristics were measured on the microbridges in the temperature range of 10 K - 300 K using currents up to 0.6 mA, which corresponds to a current density of $J = 1.5 \times 10^{10} \text{ A/m}^2$. A typical I-V curve, taken at 140 K, is shown in Fig. 3.14a. It shows nonlinearity and a large asymmetry between opposite current directions, as well as hysteresis at high current density. Similar curves could be observed at all temperatures. Still, by simply averaging voltages at small positive and negative currents ($\pm 0.1 \mu\text{A}$; this was performed with the PPMS electronics) the "resistance" R (Fig. 3.14b) shows a sharp phase transition accompanied by a resistance drop of three orders of magnitude at $T_{MI} = 150 \text{ K}$. Apparently, the measurements at least partly probe the bridge structure, but since this is a 4-point measurement (contact resistances do not affect the measurement), the asymmetry indicates that not all current is flowing between the voltage contacts. It is known that Ar-etching of STO causes the formation of a conducting surface layer by the removal of oxygen [11]. To conclusively show this in our system, we etched a 1.5 mm wide STO substrate for 30 sec. After etching, 4 Au/MoGe contacts were sputtered on top ($l = 2.6 \text{ mm}$ between the voltage contacts). Fig. 3.15 shows the temperature dependent sheet resistance $R =$

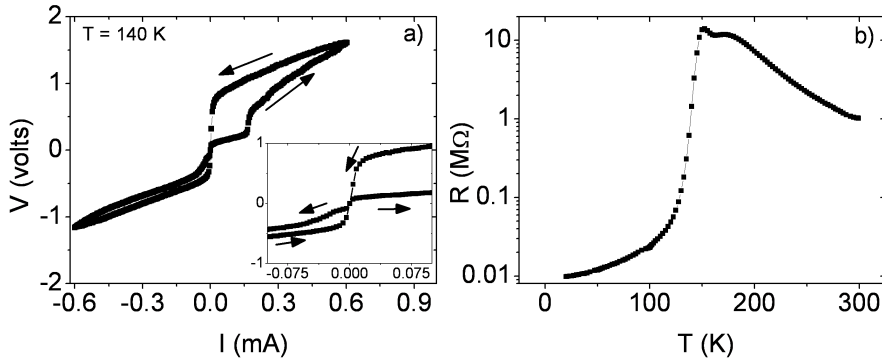


Figure 3.14 — a) I-V curve at $T = 140$ K of an LCMO bridge on STO after 14 sec overetching (inset: behavior near zero bias). b) Resistance measured as averaged voltage at $\pm 0.1 \mu\text{A}$ ($J = 2.5 \cdot 10^6 \text{ A/m}^2$) vs. temperature of the same sample.

Rw/l obtained at $I = 20 \mu\text{A}$. The dependence is metallic and the observed value for R is very close to the number reported in ref. [11]. Important to note is that the absolute value of R is in the range of (only) $1 \text{ k}\Omega - 10 \text{ k}\Omega$, which makes it substantially smaller than the peak value for R in Fig. 3.14b.

3.7.2 Conducting STO: solution

In order to restore the insulating properties of the substrate, post-annealing in an oxygen environment would probably be possible, but this is often unwanted as a process step; in our case, it might lead to strain relaxation and additional defects in the film. Instead, after the Ar-etch we subjected the etched STO substrate to an oxygen plasma for 2 min (RF power: 100 W pressure: 30 mTorr) to reinsert oxygen into the surface layer. The I-V curves after the treatment already show a significant reduction in conductivity of the substrate. In Fig. 3.16 we show an I-V curve at $T = 140$ K after 30 sec Ar-etching as well as the I-V curve, measured at the same temperature, after 2 min of oxygen plasma treatment. In this case an oxygen treatment of 4 min was enough to restore the insulating properties of the STO substrate. Generally, the procedure appears to work for small amounts of etching of the STO. Substrates which were Ar-etched for more than 1 min did not show recovery anymore, even after 4 min of plasma treatment (by which time the resist layer had been removed). We surmise that oxygen loss can be recovered by the plasma, but that more structural damage

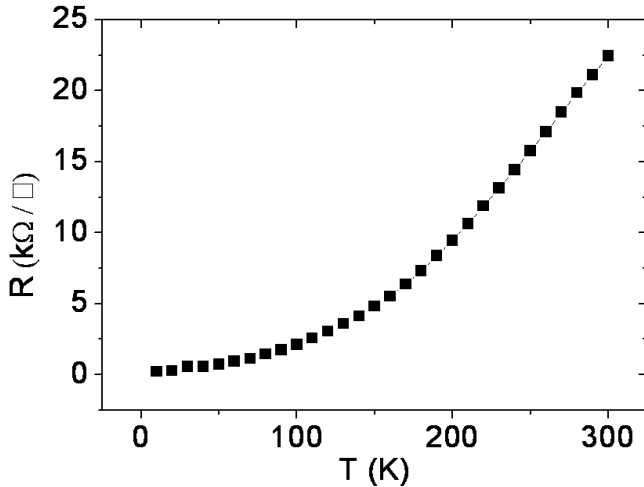


Figure 3.15 — Sheet resistance vs. temperature of the 30 sec Ar-etched STO sample ($1.5 \times 2.6 \text{ mm}^2$) obtained from I-V curves at $I = 20 \mu\text{A}$.

to the STO (amorphisation) renders this impossible. In Fig. 3.17 we show an I-V curve and the $R(T)$ plot for a microbridge which was overetched by 4 sec and then plasma-treated. The result clearly shows that when the STO substrate is restored to its insulating state, the microstructured LCMO thin film has linear and symmetric I-V characteristics for current densities between 2.5×10^7 and $1.5 \times 10^{10} \text{ A/m}^2$. Furthermore, instead of reversing the damage to the substrate after patterning the film one can also prevent the damage from occurring. This can be done by slightly underetching the LCMO thin film and by subsequently using an oxygen + argon plasma to remove the last $\sim 1 \text{ nm}$ of film. The etch rate for a 25 % Ar and 5 % O plasma (RF power: 125 W; pressure: 20 mTorr) is about 1 nm/min.

3.7.3 Contact resistance and Joule heating

With the help of the process steps described above we can fabricate microbridges (Fig. 3.13) in LCMO thin films and measure current effects intrinsic to LCMO. The presence of phase separation in our films could introduce nonlinear effects in the I-V curves around the transition. However, nonlinearities can also be caused by contact resistance and Joule heating.

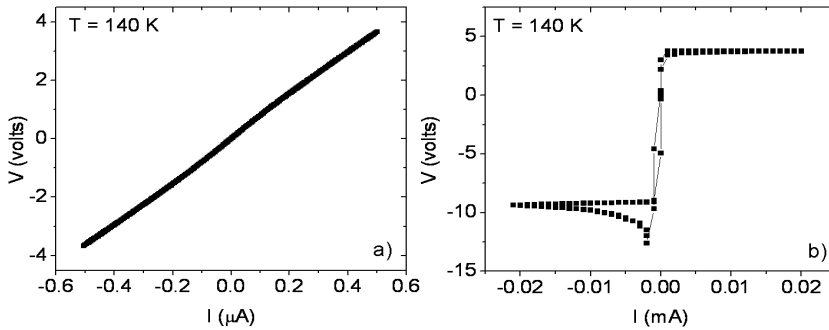


Figure 3.16 — a) I-V curve of 30 sec Ar-etched STO ($1.5 \times 2.6 \text{ mm}^2$) at $T = 140 \text{ K}$ before and b) after 2 min of oxygen plasma treatment. The high resistance between the current contacts leads to saturation of the current source.

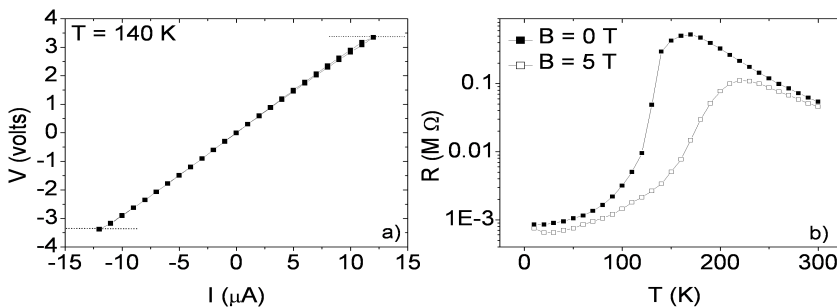


Figure 3.17 — a) I-V curve at $T = 140 \text{ K}$ of an LCMO bridge on STO after 4 sec overetching and oxygen plasma treatment. The thin lines indicate the voltage limit for the measurement; b) R-T plot at magnetic field $B = 0 \text{ T}$ and 5 T of the same sample.

Contact resistance

To observe possible effects of the contacts, we also measured the oxygen-treated sample (Fig. 3.17) in a two-probe configuration, with current injected through the voltage pads. The results are shown in Fig. 3.18 where we compare the I-V curves for two and four-point measurements taken at 10 K . The four-point measurement shows a linear and symmetric I-V curve, as expected. The two-point resistance is significantly larger (around a factor of 5 after correction for the extra lead resistance in the contact

pads). This can be attributed to a large contact resistance. Another feature is the non-linearity of the I-V curve, with the corresponding peak in the derivative dV/dI (see inset) clearly visible and most probably caused by the presence of a barrier at the contact-film interface. The interface is a known complication in two-point geometries; nonlinear and asymmetric I-V characteristics were demonstrated in rectifying Ti/Pr_{0.7}Ca_{0.3}MnO₃ contacts [12], in a p-n heterostructure involving La_{0.7}Ca_{0.3}MnO₃ and Nb-doped STO [13], and in Ag-La_{0.7}Ca_{0.3}MnO₃ heterostructures [14].

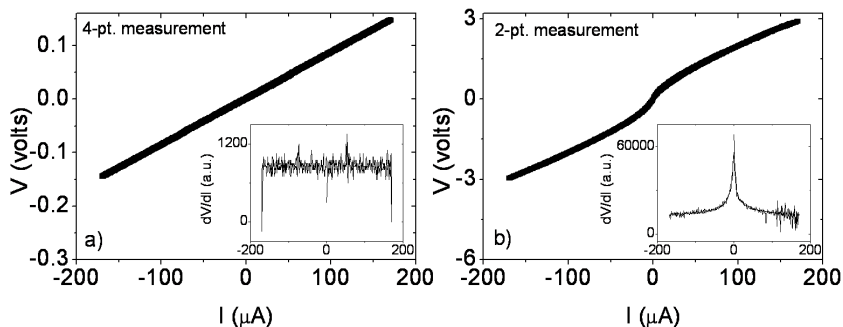


Figure 3.18 — I-V curves of an LCMO bridge on STO at $T = 10$ K (a) in 4-point configuration and (b) in 2-point configuration. Insets show derivatives dV/dI .

Joule heating

In the two-point measurements in the metallic state we also found a different type of nonlinear behavior in the I-V characteristics at larger currents which we ascribe to Joule heating. A measurement at 50 K is shown in Fig. 3.19 where the voltage-driven system suddenly switches to a lower current (higher resistance). It is not straightforward to make an estimate of the effect. The measured resistance is dominated by the contacts, but the area of the contacts is much larger than the bridge so that it is not a priori clear in which part of the structure the heating occurs. If we still assume it is the bridge, we can estimate the temperature increase ΔT from a current I using the following equation taken from [15],

$$\Delta T(T, I) = (2I^2\rho(T) + \Delta T)/(S\kappa_{sub}(T+\Delta T)) \quad (3.1)$$

with $\rho(T)$ the specific resistance of the bridge at temperature T , with cross section S , and κ the thermal conductance of the substrate. Taking $\rho(T)$ in the metallic state

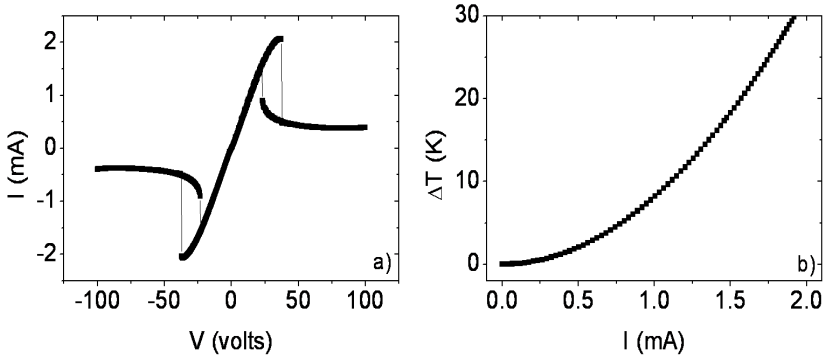


Figure 3.19 — (a) I-V curve of an LCMO bridge on STO at $T = 50$ K measured in 2-point configuration. (b) Calculation of the expected Joule heating represented as temperature increase ΔT vs. applied current I .

independent of temperature and using the value $\rho = 260 \mu\Omega \text{ cm}$ found in the four-point measurement at $T = 50$ K, and with $\kappa = 16 \text{ WK}^{-1} \text{ m}^{-1}$ [16], we find $\Delta T \approx 30$ K at 2 mA (Fig. 3.19b). The model is quite crude, but the result at least indicates that heating effects cannot be neglected in our bridges at these high currents (corresponding to a current density of $> 10^{10} \text{ A/m}^2$). If the heating is severe enough the effective temperature could increase to above the metal-insulator transition. The corresponding I-V should show at first a gradual increase of the resistance (decrease of current as function of applied voltage). This should be followed by a gradual decrease of resistance once the bridge has warmed into the paramagnetic insulating state. However, we observe a constant resistance value up to an applied bias of 25 V after which the resistance slowly increases before it sharply rises (current drops) to a much higher value. The mechanism leading to the switching behavior is not yet understood, however, and needs further investigation.

Bibliography

- [1] R. Krupke, Z. Barkay, and G. Deutscher, *Physica C* **315**, 99 (1999)
- [2] Z.Q. Yang, R. Hendriks, J. Aarts, Y.L. Qin and H.W. Zandbergen, *Phys. Rev. B*, **70**, 174111 (2004)
- [3] Specimen thickness should not be confused with the film thickness.
- [4] C. Beekman et al., *Phys. Rev. B*, in preparation
- [5] Gianluigi et al., *J. Microscopy*, **180**, 211 (1995)
- [6] T. Riedl, T. Gemmin, K. Dörr, M. Luysberg, and K. Wetzig, *Microsc. Microanal.* **15**, 213 (2009)
- [7] L. Samet, D. Imhoff, J.-L. Maurice, J.-P. Contour, A. Gloter, T. Manoubi, A. Fert, and C. Colliex, *Eur. Phys. J. B.* **94**, 179 (2003)
- [8] S. Estradé, J. Arbiol, F. Peiró, I.C. Infante, F. Sánchez, J. Fontcuberta, F. de la Peña, M. Walls, and C. Colliex, *Appl. Phys. Lett.* **93**, 112505 (2008)
- [9] Amorphous $\text{Mo}_{70}\text{Ge}_{30}$ was found to be a good adhesion layer for the Au contact.
- [10] C. Beekman, I. Komissarov, M. Hesselberth, and J. Aarts, *Appl. Phys. Lett.* **91**, 062101 (2007)
- [11] D. Kan, T. Terashima, R. Kanda, A. Masuno, K. Tanaka, S. Chu, H. Kan, A. Ishizumi, Y. Kanemitsu, Y. Shimakawa, and M. Takano, *Nat. Mater.* **4**, 816 (2005).
- [12] A. Sawa, T. Fujii, M. Kawasaki, and Y. Tokura, *Appl. Phys. Lett.* **85**, 4073 (2004)
- [13] X. P. Zhang, B. T. Xie, Y. S. Xiao, B. Yang, P. L. Lang, and Y. G. Zhao, *Appl. Phys. Lett.* **87**, 072506 (2005)

- [14] D. S. Shang, L. D. Shen, Q. Wang, W. Q. Zhang, Z. H. Wu, and X. M. Li, *Appl. Phys. Lett.* **89**, 172102 (2006)
- [15] P. Padhan, W. Prellier, Ch. Simon, and R.C. Budhani, *Phys. Rev. B* **70**, 134403 (2004)
- [16] E.F. Steigmeier, *Phys. Rev.* **168**, 523 (1968)

Chapter 4

Strain effects in (La,Ca)MnO₃ thin films

4.1 Introduction

The physics of doped manganites (explained in Chapter 2) is mainly determined by two competing factors: trapping of the electrons in Jahn-Teller (JT) distortions (polarons) and the itinerancy of the electrons in the Double-Exchange mechanism [1] when spins become polarized. This competition and therefore the properties of the material La_{1-x}Ca_xMnO₃ strongly depend on the amount of Ca-doping. In the doping range of $0.2 < x < 0.5$ a combined paramagnetic insulator to ferromagnetic metal (PI-FM) transition takes place at temperature T_{MI} . Direct comparison between systems with different alkaline ion doping results in a clear correlation between the position of T_{MI} and the tolerance factor (discussed in Chapter 2) [2, 3]. For example, the material La_{0.67}Sr_{0.33}MnO₃ (LSMO) has larger bandwidth (itinerancy) and higher transition temperatures compared to the smaller bandwidth system La_{0.67}Ca_{0.33}MnO₃ (LCMO). This correlation results in tunability of the material properties upon application of pressure [4] or epitaxial strain. For instance, the application of strain amplifies the JT distortions and makes them more static in nature. This has an inhibiting effect on band formation, which leads to reduction of T_{MI} [5, 6] in manganite thin films.

Before we go to LCMO microbridges we investigate the effect of strain on the magnetotransport properties of as-grown unstructured LCMO thin films. The question is whether the thin films still show the basic properties of bulk LCMO. Especially for ultra thin films the properties of the film-substrate interface layer may lead to deviating properties for the film. We compare LCMO films grown on flat SrTiO₃ (STO) (tensile strain) and NdGaO₃ (NGO) (lattice matched) substrates. Furthermore, we use substrates with a misorientation of 1° towards the [010] direction to introduce unit-cell high step edges onto the STO substrate surface which should induce addi-

tional disorder in the thin films. This provides new insights on the influence of strain and disorder on the properties of manganite thin films.

4.2 Transport properties and magnetization measurements

In this section we present the transport properties of as-grown unpatterned LCMO films on flat STO, 1° misoriented STO and NGO substrates as function of film thickness. We also investigate whether the Curie temperature coincides with the metal-insulator transition for our thin films. Furthermore, the deviations in Mn-valence near the LCMO-substrate interface (see Chapter 3) are expected to influence the transport and the magnetic properties, especially when the film thickness becomes small.

The magnetotransport properties of the as grown, unpatterned films as function of temperature are measured in both 0 T and 5 T applied magnetic fields. During measurements the contacts are arranged in a four point measurement geometry (distance between the voltage contacts is ~ 1 mm), to exclude influence of the contact-film interface resistance. We have measured current-voltage (I-V) characteristics for the temperature range 20 \rightarrow 300 K from which we determined the film resistance. The temperature and magnetic field regulation were done in a PPMS (Physical Properties Measurement System, Quantum Design) but external current sources and nanovoltmeters were used to perform the transport measurements. Here we remind the reader of the sample nomenclature which we introduced in Chapter 3, $L(d)$, $L(d)_{mis}$ and $L(d)_{NGO}$, with d the film thickness.

4.2.1 T_{MI} dependence on thickness

Films on flat STO

We have measured the I-V characteristics in a temperature range of 20 - 300 K for films with varying thicknesses between 6 - 20 nm. In Fig. 4.1 we show the temperature dependent resistance $R(T)$, as determined from the I-V characteristics, for three LCMO films grown on flat STO. The resistance values are determined at an applied current I of 0.1 μ A. Here we note that the I-V curves show weak nonlinear behavior around the transition but they are linear for most temperatures. The films show a clear metal-insulator transition accompanied by a resistance drop of three orders of magnitude (note the logarithmic scale). All films also show typical CMR effect, a reduction in resistance of a few orders of magnitude upon application of a 5 T magnetic field. Sample $L(20)$ shows the typical $R(T)$ behavior for a fully strained LCMO film. The transition temperature T_{MI} , which corresponds to the maximum resistance value, is 170 K, which occurs approximately 100 K below T_{MI} for bulk LCMO.

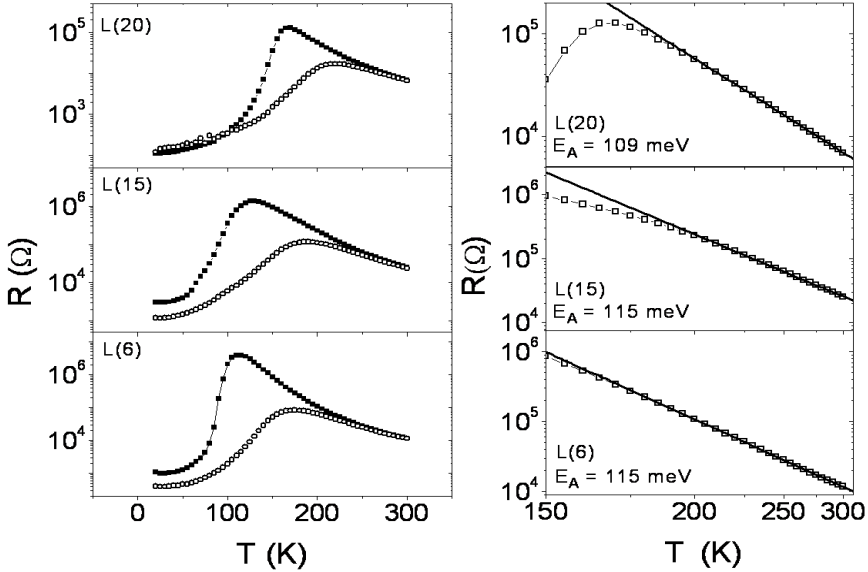


Figure 4.1 — (Left) resistance vs. temperature behavior of samples L(20) (top panel), L(15) (center panel) and L(6) (bottom panel). Determined from the I-V curves at an applied current of $0.1 \mu\text{A}$. Squares: zero field; circles: $B = 5 \text{ T}$. (Right) $\log R$ vs. T in the temperature range $150 - 300 \text{ K}$ for the same samples. Note: the scale on the T-axis is reciprocal in order to fit to $1/T$ -behavior. The fit to extract the activation energy (E_A) of the polaron hopping process is also shown (solid lines).

Furthermore, we observe that T_{MI} is reduced when the film becomes very thin; for example film L(6) shows the transition at $T_{MI} = 110 \text{ K}$, which is 60 K below T_{MI} for L(20). The thickness dependence of T_{MI} is shown in Fig. 4.2. For films grown on flat STO the metal-insulator transition is steadily shifted to lower temperature as the film thickness is reduced. We did not observe transition temperatures below 100 K . However, we found that one film (L(10), indicated by \star in Fig. 4.2) grown on flat STO deviated from this trend. In the previous chapter, see Fig. 3.7c, we surmised that L(10) may have a deviating epitaxial relation with the substrate. There is a connected observation in the magnetization measurements, which is discussed in section 4.2.2.

In the paramagnetic state, $R(T)$ is expected to show activated behavior. Therefore, in Fig. 4.1, we also plot $\log R$ vs. T^{-1} . A linear fit to the data provides the activation

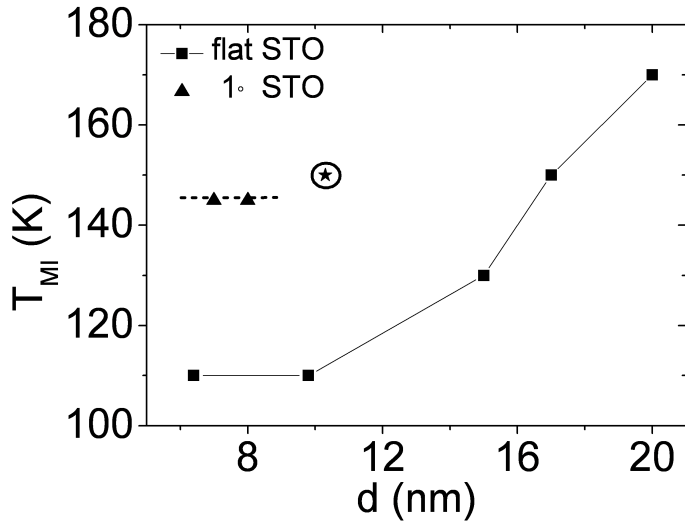


Figure 4.2 — The dependence of T_{MI} on film thickness for LCMO films grown on flat (squares + star) and 1° misoriented STO (triangles). The star designates sample L(10). Drawn and dashed lines are guides to the eye.

energy (E_A) for the polaron hopping process. For most films the high temperature data show activated behavior with $E_A = 110 - 120$ meV (see Table 4.1), independent of the film thickness. Deviations typically set in around $1.3x T_{MI}$ (for example see sample L(15) center panel Fig. 4.1). In this respect at least, the thin films do not behave different from bulk material. However, in Chapter 3 we found that all films on STO are coherently strained and that the out-of-plane lattice parameter a_{out} (Fig. 3.6) shows a similar thickness dependence as T_{MI} with the exception of L(10) and films on misoriented STO.

Films on 1° misoriented STO

A novel feature of our studies is the investigation of the effect of unit-cell high step edges on the STO substrate surface on the thin film properties. For these films the transport properties were measured in a four-point geometry with the current directed perpendicular to the step edges (see inset Fig. 4.3). Their thickness was determined from HR-TEM (high resolution transmission electron microscopy) micrographs and is 7 and 8 nm ($L(7)_{mis}$ and $L(8)_{mis}$). The $R(T)$ for $L(7)_{mis}$ was measured at $I = 0.1$

μA and is shown in Fig. 4.3, $R(T)$ of sample L(6) is shown for comparison. The

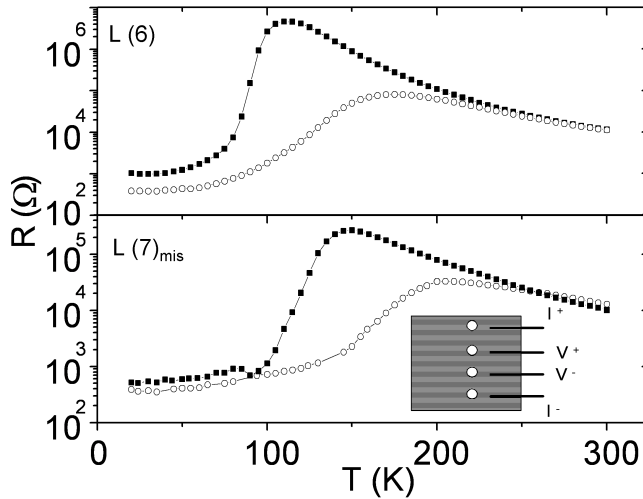


Figure 4.3 — Resistance vs. temperature behavior of sample L(6) (also shown in Fig. 4.1) and of $L(7)_{mis}$. For the films on misoriented STO the transport properties were measured with the current directed perpendicular to the step edges (see inset for measurement geometry). The resistance values were determined from the I-V curves at an applied current of $0.1 \mu\text{A}$. The squares denote zero field; circles: $B = 5 \text{ T}$.

observed T_{MI} for the films on 1° STO is 145 K, so T_{MI} is much less reduced than for films on flat STO (see Fig. 4.2, triangles). However, from the HR-TEM and RSM (reciprocal space mapping) characterization (see Chapter 3) it is clear that the films on misoriented STO are fully epitaxial across the entire film thickness. The lack of reduction in T_{MI} for films on misoriented STO is step-induced but not due to the loss of epitaxial relation with the substrate. It has been shown before that strain relaxation in these materials may occur in the form of dislocations in the film [7]. From HR-TEM we did not observe any dislocations in our thin films, however, point defects should still be present and the amount is possibly enhanced by the presence of the steps.

Films on NGO

We also investigated the transport properties of films on NGO (100) substrates (cubic notation) [8], with in plane lattice parameters of $a = 3.865 \text{ \AA}$ and $c = 3.87 \text{ \AA}$. In this case the film and substrate are almost lattice matched (mismatch: -0.26%) and therefore the film can be considered strain-free. In Fig. 4.4 we compare the $R(T)$ behavior of two LCMO films on NGO substrates with thicknesses 10 nm ($L(10)_{NGO}$) and 30 nm ($L(30)_{NGO}$). In both films the resistance decrease at the transition is around one

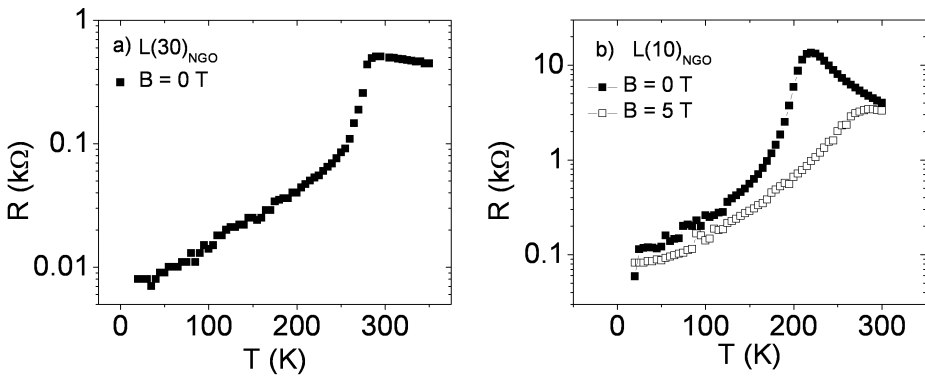


Figure 4.4 — a) Resistance behavior of $L(30)_{NGO}$. b) Resistance behavior of $L(10)_{NGO}$, which was measured in both $B = 0 \text{ T}$ and $B = 5 \text{ T}$ magnetic fields. The measurement was done in a four point configuration at an applied current $I = 0.1 \text{ }\mu\text{A}$.

order of magnitude. It drops an additional order of magnitude upon cooling to low temperatures. For $L(10)_{NGO}$ $R(T)$ was also measured in 5 T magnetic field, which shows that the transition is accompanied by the well known CMR-effect. The transition temperature of $L(30)_{NGO}$ is equal to T_{MI} of bulk LCMO. However, $L(10)_{NGO}$ shows that films on NGO substrates also show a strong dependence of T_{MI} on film thickness. This corresponds to the previously observed thickness dependence reported in ref. [9]. The observed reduction could be caused by the very small amount of strain that is imposed on the thin films.

4.2.2 Magnetic properties

In this paragraph we present the magnetization M of the as-grown films on flat and misoriented STO substrates. We have not measured the magnetic properties of the films on NGO because the substrate gives a large paramagnetic background due to the

presence of the magnetic Nd^{3+} -ion. Typical M vs. T behavior measured in magnetic fields of $B = 1$ T and $B = 0.1$ T is shown in Fig. 4.5. The Curie temperature was determined from M vs. T , measured in zero magnetic field and at $B = 0.1$ T, by taking the intercept of the constant high temperature magnetization with the linearly increasing $M(T)$. When the film thickness is reduced, we observe that T_C is also

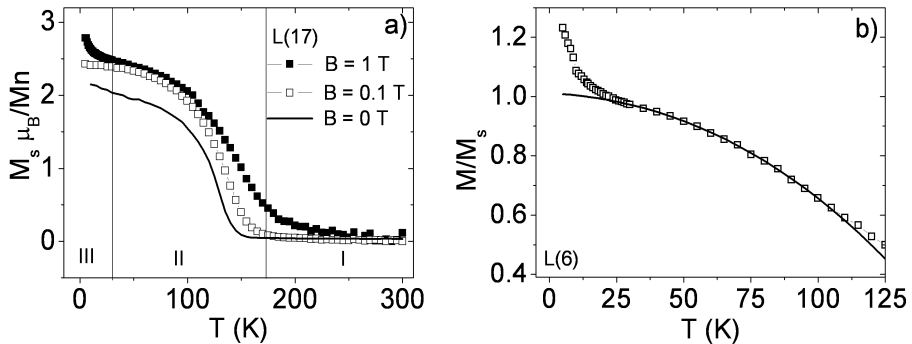


Figure 4.5 — a) M vs. T behavior for L(17). The magnetization was measured in $B = 1$ T (closed squares), $B = 0.1$ T (open squares) and $B = 0$ T (line). b) M vs. T behavior for L(6) normalized to the intercept of Bloch's law (solid line) and the linearly increasing low T upturn. The fit is $M \propto T^{-3/2} + T^{3/2}$.

shifted to lower temperature as shown in Fig. 4.6. The magnetic transition coincides with the metal-insulator transition also when the film thickness is reduced. However, when T_C is extracted from the measurements in $B = 0.1$ T the Curie temperature is enhanced for all thicknesses. Probably when measured in even higher fields (for example, $B = 0.3$ T as in [5]) T_C would be independent of film thickness. For the measurement in $B = 1$ T we assume that the magnetization is saturated. From the $M(T)$ behavior (see Fig. 4.5a) three regions can be differentiated. Region I: above the T_C the sample is in the paramagnetic state. Region II: between 30 K and T_C the sample is in the ferromagnetic state. In region III, below $T = 30$ K, the magnetization shows a sudden increase. The relative strength of the upturn in $M(T)$ increases as the film thickness is reduced but the temperature at which the upturn starts is constant. Furthermore, the upturn is absent in $B = 0.1$ T measurements. This upturn is not an intrinsic feature of the LCMO thin films. From Fig. 4.7 it becomes clear that the M vs. T of a bare STO substrate also shows an upturn below $T = 30$ K. Apparently, at low T a paramagnetic contribution ($\chi = C/T$, with C the Curie constant) dominates but disappears into the diamagnetic background above $T = 30$ K. We surmise that the emergent paramagnetism is due to the presence of impurities. Fig. 4.5b shows the M

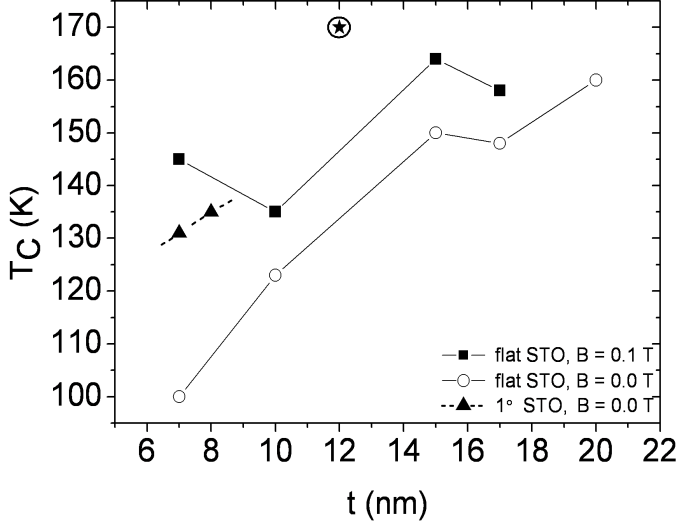


Figure 4.6 — The Curie temperature as function of film thickness. Determined from M vs T at $B = 0$ T (circles) and $B = 0.1$ T (squares). The triangles show T_C for two films grown on 1° STO and the star shows T_C for sample L(10). The drawn and dashed lines are guides to the eye.

vs. T behavior for sample L(6) in the ferromagnetic state measured in $B = 1$ T. For isotropic ferromagnetic materials demagnetization at low temperatures is caused by the excitation of ferromagnetic spin waves. We have fitted the M vs. T curve with,

$$M(T) = M_s * (1 - B_1 T^{3/2} - B_2 T^{5/2}) \quad (4.1)$$

with $B_1 = 170 \times 10^{-6} \text{ K}^{-3/2}$ and $B_2 = 1.8 \times 10^{-6} \text{ K}^{-5/2}$ which corresponds to the expected Bloch dependence. The value for M in Fig. 4.5 is normalized to the intercept of the fit and the linearly increasing low T upturn.

We have also investigated the field dependent magnetization at $T = 10$ K (Fig. 4.8). From these results we can extract coercive field and the value for the saturation magnetization (M_s) as function of film thickness. The coercive field varies between ± 6 and ± 15 mT for the different samples. The magnetization is given in units of μ_B per Mn-ion and can be described, at high fields, as $M = M_s + \chi H$ (see inset Fig. 4.8). The plotted data in the main graph is corrected for the diamagnetic and paramagnetic contribution of the STO substrate by subtracting χH determined at high fields. The values for M_s are determined after correction by taking the value for M at $B = 1$ T. Typical saturation magnetization for bulk LCMO would be around $3.7 \mu_B$

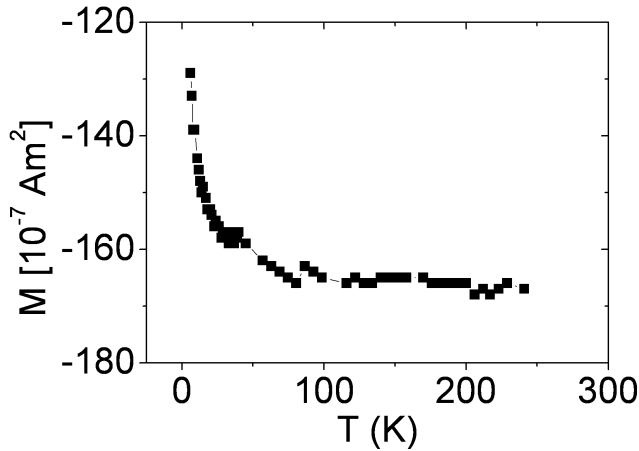


Figure 4.7 — M vs. T behavior for a bare STO substrate measured in $B = 1$ T.

per Mn-ion. For our films we observe slightly fluctuating values for M_s but always low compared to the expected bulk value (see Fig. 4.8). The lower values indicate that a magnetically dead or weak layer is generally present in our LCMO thin films.

4.2.3 Discussion

The main results which are presented in Chapters 3 and 4 are summarized in Table 4.1. We will use these results to form a general picture on strain effects in LCMO thin films. The characterization presented in Chapter 3 led to a few observations, summarized here. First, all films on STO are fully strained (the lattice parameters a_{in} and a_{out} are indicated in Table 4.1). Second, the films have the correct oxygen stoichiometry. Third, a reduction in Mn-valence occurs at the LCMO/substrate interface over a thickness of 2 to 5 nm for the various films. Here we will correlate these sample characteristics with the observations from the transport and magnetic properties of the films.

The values for T_{MI} and T_C are indicated in the table. Their values coincide quite well, T_C is generally (for films on flat STO) slightly higher. For all thicknesses the metal-insulator transition is strongly coupled to the onset of ferromagnetic ordering. Since our films are not oxygen deficient [10] we conclude that strain amplifies the JT distortions, which results in a reduced bandwidth for decreasing film thickness. All films (apart from L(10)) show a low value for the saturation magnetization compared

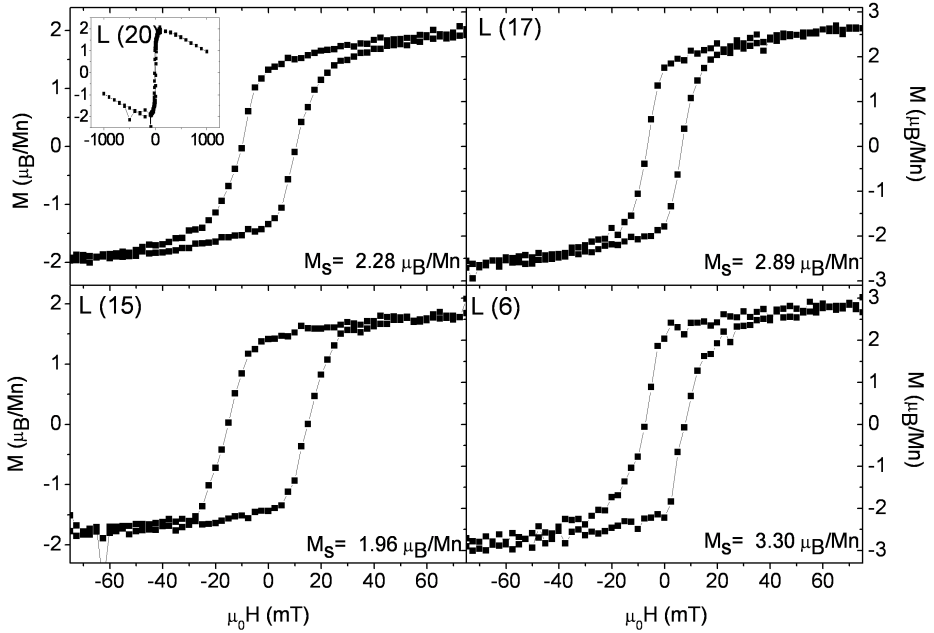


Figure 4.8 — The demagnetization curves for four different LCMO films on flat STO. The curves were measured between ± 5 T and at $T = 10$ K. The value for the saturation magnetization M_s is indicated. The plotted data is corrected for the diamagnetic + paramagnetic background of the substrate. Inset: uncorrected data for L(20).

to the expected value ($3.7 \mu_B/\text{Mn-ion}$) for bulk LCMO (see Table 4.1). This indicates the presence of a 'dead layer' [11, 12]. We find that L(10) did not show the reduction in valence and has a magnetic moment close to the expected bulk value. This result shows that the interface layer with reduced Mn-valence, which is generally present in our LCMO thin films, is magnetically dead or weak. Apparently, the dead layer reduces the effective thickness of the film which also explains the relatively high value for T_{MI} in L(10). Here we note that also sample L(6) shows a relatively high value for M_s when determined at $B = 1$ T. It is possible that at this high field the dead layer might become polarized, which results in a higher value for saturation magnetization.

The films which were grown on misoriented STO also show less reduction in T_{MI} than expected for their absolute film thickness. Here, the presence of the step edges

Table 4.1 — Summary of the measured values for the thin films presented in this chapter. Samples L(20)-L(6) are grown on flat STO, L(8)_{mis} and L(7)_{mis} are grown on 1° misoriented STO and samples L(30)_{NGO} and L(10)_{NGO} are grown on NGO substrates. The measured variables are, d : film thickness (nm), a : in-plane lattice parameter (Å), b : out-of-plane lattice parameter (Å), T_{MI} : metal insulator transition (K), T_C : Curie temperature (K), E_A : activation energy of polaron hopping (meV), M_s : saturation magnetization at $T = 10$ K determined at $B = 1$ T (μ_B/Mn) and the corresponding thickness of the dead layer (nm).

Sample	d nm	a (Å)	b (Å)	T_{MI} (K)	T_C (K)	E_A (meV)	M_s (μ_B/Mn)	dead layer (nm)
L(20)	20	3.90	3.8113	170	160	109	2.28	7.6
L(17)	17	3.91	3.8135	150	148	114	2.89	3.7
L(15)	15	3.90	3.8097	130	150	115	1.96	7.0
L(10)	10.3	3.90	3.796	150	170	114	3.50	0.5
L(6)	6.4	3.91	3.7979	110	100	115	3.30	0.7
L(8) _{mis}	8	-	-	145	135	119	2.41	2.8
L(7) _{mis}	7	3.90	3.7911	145	131	116	2.22	2.8
L(30) _{NGO}	30	-	-	285	-	-	-	-
L(10) _{NGO}	10	-	-	220	-	-	-	-

could lead to disorder (in the form of local defects [7]). Kumar et al. [13] use the Holstein-Double Exchange model to show how disorder enhancement of the polaron tendency in manganites leads to increased resistivity and reduction of T_{MI} . However, in our case the disorder leads to an enhancement of the one electron bandwidth (T_{MI}). In Chapter 5 we will correlate this observation with microbridge resistivities. Furthermore, an observation which was not mentioned till now is the presence of a large magnetoresistance effect at low temperatures for some samples. This effect is also dependent on film thickness but the microbridges in Chapter 5 show similar and larger MR effects, therefore we postpone the discussion to Chapter 5.

One observation which was not discussed up to now is the deviation from activated behavior above T_{MI} . We saw in Fig. 4.1b that some samples deviate from activated behavior already at $1.3xT_{MI}$. It might be thought that variable range hopping (VRH) [14] is at play, but the typical $T^{-\frac{1}{4}}$ -dependence expected at intermediate temperatures [15] is not found [16]. It seems probable that the emergent magnetism in this temperature range obscures the VRH mechanism.

4.3 Low field magnetoresistance

4.3.1 Introduction

In the previous sections we have seen that the LCMO thin films exhibit colossal magnetoresistance behavior around the transition in high magnetic fields. However, in the low magnetic field regime a different type of magnetoresistance (MR) effect occurs, for instance caused by the presence of grain boundaries [17–20] or the Anisotropic Magnetoresistance (AMR) effect. In this section we describe the resistance dependence of manganite thin films on applied magnetic fields. The AMR effect depends on the distribution of magnetic domains, since the resistance of a domain with M parallel to the applied current I is different from the resistance of a domain with M perpendicular to I . In many materials (mainly magnetic transition metals) the AMR effect is observed to vary as

$$\frac{\Delta\rho(H)}{\rho_{av}} = \frac{\Delta\rho}{\rho_{av}} \left(\cos^2\theta - \frac{1}{3} \right) \quad (4.2)$$

with $\Delta\rho = \rho_{\parallel} - \rho_{\perp}$ the difference between resistivity of domains parallel and perpendicular to the applied current, θ the angle between M and current I and ρ_{av} the appropriate average for the longitudinal and transverse resistivities. Here we will present low field-MR results on unpatterned LCMO thin films grown on STO substrates and we discuss the mechanism behind the AMR effect in manganites. The mechanism turns out to be different from that in transition metals.

4.3.2 Films on flat STO

We start with unpatterned as-grown thin LCMO films on flat STO substrates. The resistance is measured in a four point configuration to exclude any effects caused by contact resistances. We apply a field in the plane of the film, which is scanned between ± 500 mT, at which we assume the sample to be saturated (single domain). We investigated the temperature regime $T = 50 - 200$ K for both field directions $H \parallel I$ and $H \perp I$. At low field, we expect hysteresis since LCMO has a preferred direction of magnetization (easy axis lies along the (110) direction of the STO) which should induce anisotropy (magnetocrystalline anisotropy). Fig. 4.9 shows the field dependent resistance behavior of a sample L(20) for $H \perp I$ (left) and $H \parallel I$ (right). The behavior is shown at several temperatures between 50 - 150 K. At high fields the resistance increases linearly with decreasing magnetic field as expected from the CMR effect. Upon decreasing the field two types of behavior are observed depending on the direction of the applied field w.r.t. the current. For $H \parallel I$ the resistance can

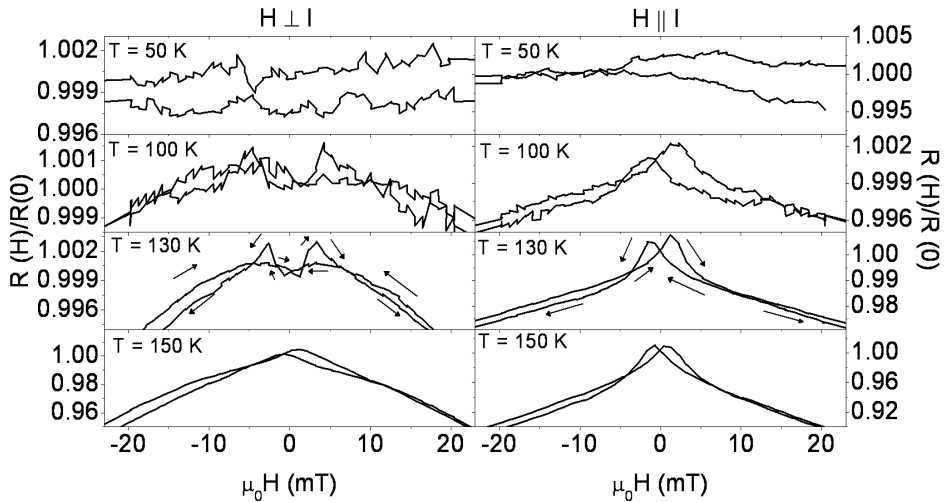


Figure 4.9 — The resistance behavior sample L(20) as function of low magnetic field for T : 50 - 150 K. Left: $H \perp I$. Right: $H \parallel I$. Measured at $I = 0.5 \mu\text{A}$.

start to vary superlinearly (right panel) when zero field is approached, after which it peaks at the switching field, $-H_{sw}$, followed by a drop in resistance. For $H \perp I$ the resistance varies sublinearly with field well before zero field is reached. It then shows a dip before it increases again and drops at $-H_{sw}$. For both directions the linear resistance behavior is recovered in negative fields and upon scanning the field in the opposite direction similar behavior is observed with switching at $+H_{sw}$. The anisotropy w.r.t. field direction is only observed in the temperature range between 130 K and 100 K (below the transition, see Fig. 4.1). For both field directions it is difficult to observe any hysteresis effects at low temperatures.

The sublinear behavior as in Fig. 4.9 is not observed for the thinner films. For instance, Fig. 4.10 shows the switching behavior for L(10), which appears to be independent of field direction. The field at which switching occurs decreases monotonically with increasing temperature. Switching is observed to slightly above the measured transition temperature. Furthermore, at very small thicknesses when T_{MI} is significantly reduced switching is only observed in a small temperature range just below the transition.

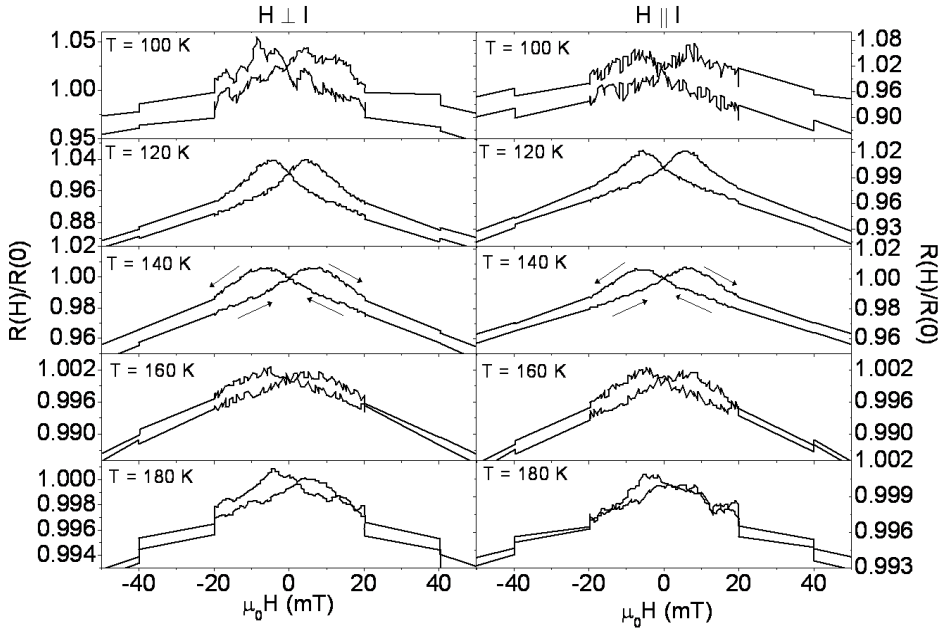


Figure 4.10 — The resistance behavior of sample L(10) as function of low magnetic field ($T_{MI} = 150$ K). Left: $H \perp I$. Right: $H \parallel I$. Measured at $I = 0.5 \mu\text{A}$. The curves for $T = 180$ K are smoothed by using adjacent averaging.

4.3.3 Films on 1° misoriented STO

We have also studied the switching behavior for films which were grown on 1° misoriented STO (see Fig. 4.11). The measurements were done in the same configuration as the films on flat STO with current directed perpendicular to the step edges of the substrate. The behavior for both field directions is similar (i.e. no anisotropy) and the switching field value is decreased with increasing temperature. The hysteretic behavior in low magnetic fields persists up to $\sim 1.4x T_{MI}$. It is not clear whether the switching above T_{MI} is induced by the presence of the step edges on the STO surface, because, it was also observed for one sample grown on flat STO (not shown).

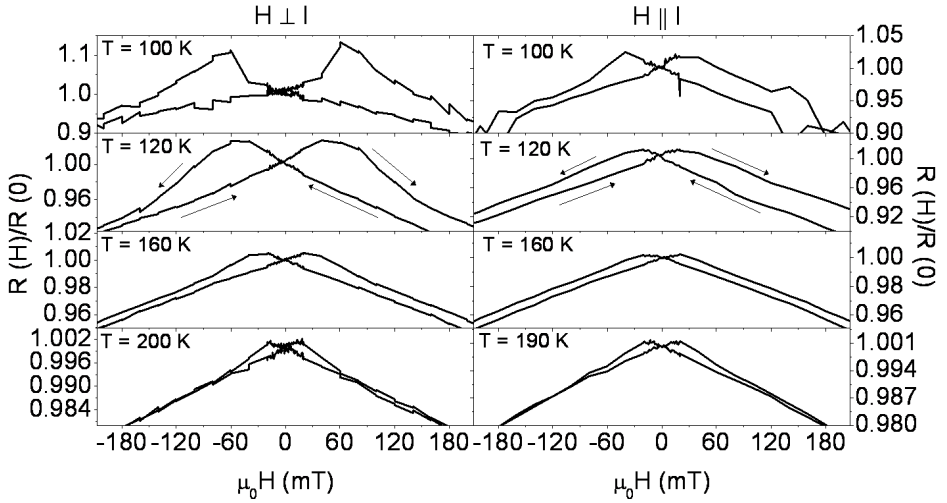


Figure 4.11 — The resistance behavior of sample $L(7)_{mis}$ as function of low magnetic field, current is applied perpendicular w.r.t. the step edges. Left: $H \perp I$. Right: $H \parallel I$. Measured at $I = 0.5 \mu\text{A}$.

4.3.4 Discussion

In 3d transition metals such as Ni (and Ni-alloys), a strong ferromagnetic material, the AMR behavior can be described by combining the two current model [21] with spin-orbit coupling (SOI) [22, 23]. The current is carried by two parallel channels, the majority and the minority electrons and the resistivity in each channel is determined by s-s and s-d scattering. When the SOI mechanism is inactive the $d\uparrow$ band is full (no holes present), therefore s-d scattering is negligible. However, when the SOI is turned on $d\uparrow \rightarrow d\downarrow$ scattering takes place creating $d\uparrow$ holes and opening channels for s-d scattering. This introduces scattering of $s\uparrow$ electrons into both $d\uparrow$ (no spin flip) and $d\downarrow$ (spin flip) states. These scattering events increase the total resistivity of the majority band because s-electrons become more localized. A requirement for scattering to take place is that the momentum \mathbf{k} of the s-electron lies in the plane of the classical orbit of the empty d-state. Furthermore, the angular momenta \mathbf{L} of the $3d\uparrow$ holes and occupied states are not generally parallel which induces a magnetic moment. This magnetization results in the states having orbitals perpendicular to the direction of magnetization to be filled first. Left are the holes with \mathbf{M} parallel to the orbitals. Anisotropy is now created because only when the magnetization is parallel

to the current ($M \parallel I$) can s-electrons scatter into these empty d-states. Therefore, the resistivity in the case $M \parallel I$ is generally larger than for $M \perp I$ ($\rho_{\parallel} > \rho_{\perp}$). Manganites behave quite differently from transition metals when low magnetic fields are applied. The two important ingredients are AMR (R is dependent on the angle θ between M and I) and magnetocrystalline anisotropy (MCA) which in the case of manganites is biaxial. In ref. [24] it is explained that the low field MR effect cannot be described with a single domain model with domain wall motion. The single domain model can describe the linear behavior at high fields very well, but the behavior would remain linear until H_{sw} , where it would always show a drop in resistance. To describe a linear dependence at high field with deviations from linearity upon approaching zero field, a multidomain model has to be used, in which transverse domains ($M \perp H$) nucleate and grow. The occurrence of these transverse domains is a direct result of the presence of biaxial MCA. The total resistance of the material depends on the fraction of parallel, antiparallel and transverse domains which are present in the sample. Magnetization directions in between these three domain states are forbidden. The

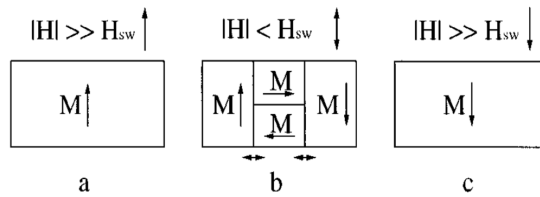


Figure 4.12 — Domain state of a sample with biaxial MCA. a) and c) At fields much larger than H_{sw} the sample is in a single domain state. b) When the field is decreased towards zero a multi domain state starts to form in which the fraction of transverse domains is determined by H . The deviation from linearity occurs due to the nucleation and growth of the transverse domains. Figure is taken from ref. [24].

superlinear behavior in the $H \parallel I$ configuration is caused by the formation of domains with $M \perp H$, $M \perp I$ domains have higher resistivity (due to AMR) compared to the the $M \parallel I$ domains. In the same way the sublinear behavior occurs in the $H \perp I$ configuration, however, now the nascent transverse domains have magnetization parallel to the applied current and therefore lower resistivity. The subsequent resistance jump/drop occurs when the magnetization aligns once more along the field direction (see Fig. 4.12). Whether the $H \perp I$ configuration shows a jump or drop at H_{sw} depends on the abundance of transverse, parallel and antiparallel domains at the onset of the reversal. When the sample has a large fraction of transverse (antiparallel) domains a rise (drop) in resistivity occurs because the final state has higher (lower) resistivity compared to the initial state. This explains the observed behavior of sample L(20) quite

well. However, we also found that the $H \perp I$ behavior can be very similar to $H \parallel I$ for thinner films or films grown on miscut STO. Clearly, the resistivity behavior depends on the domain configuration of the sample, as was already shown by Wu et al. [25] through correlation of resistivity and Magnetic Force Microscopy (MFM) measurements. Therefore, we may imagine that for films with very small thicknesses ($d < 20$ nm) and for films on misoriented STO the MCA could be uniaxial instead of biaxial. This is supported by ref. [26] in which photoelectron emission microscopy is used to show that magnetic domains are elongated along the step direction for $(\text{La,Sr})\text{MnO}_3$ films grown on misoriented (0.2°) STO, and by ref. [27] in which step-induced uniaxial MCA is reported in $\text{La}_{0.67}\text{Sr}_{0.33}\text{MnO}_3$ thin films ($0.1 - 0.3^\circ$ STO). For smaller miscut angles competition between biaxial and uniaxial MCA is observed (in ref. [26]). In our case, with a miscut of 1° we imagine that the presence of unit-cell high steps on the STO surface favors uniaxial MCA especially for small film thicknesses.

4.4 Conclusion

In this chapter we have observed that the metal-insulator transition for LCMO thin films indeed coincides with the onset of ferromagnetic ordering just as in the bulk material. The substrate imposed strain inhibits band formation which leads to a reduction in T_{MI} for decreasing film thickness. The introduction of step edges onto the STO surface leads to additional disorder, in the form of local defects. We observe that the steps (c.q. the defects) probably enhance the bandwidth which results in a T_{MI} which is less reduced than expected from the thickness. Furthermore, magnetization measurements, combined with the characterization in Chapter 3, show that the observed reduction in Mn-valence at the film-substrate interface results in a magnetically dead or weak layer. The low field MR measurements show that the presence of the step edges (and the reduction of film thickness ($d < 20$ nm) for films on flat STO) leads to uniaxial Magnetocrystalline Anisotropy.

Bibliography

- [1] C. Zener, Phys. Rev. **82**, 403 (1951)
- [2] A. Machida, M. Itoh, Y. Moritomo, S. Mori, N. Yamamoto, K. Ohoyama, and A. Nakamura, Physica B **281** & **282**, 524 (2000)
- [3] Y. Tokura and Y. Tomioka, C, J Mag. Mag. Mat. **200**, 1 (1999)
- [4] H.Y. Hwang, T.T.M. Palstra, S.-W. Cheong, and B. Batlogg, Phys. Rev. B, **52**, 15046 (1995)
- [5] J. Aarts, S. Freisem, and R. Hendrikx, and H.W. Zandbergen, Appl. Phys. Lett. **72**, 2975 (1998)
- [6] K. Dörr, J. Phys. D: Appl. Phys. **39**, R125 (2006)
- [7] K. Terai and M. Lippmaa, P. Ahmet and T. Chikyow, T. Fujii, H. Koinuma, and M. Kawasaki, Appl. Phys. Lett. **80**, 4437 (2002)
- [8] Note that different orientations of the NGO substrate lead to different strain states in the film. Here we use NGO (100), cubic notation, which is (110) in orthorhombic notation.
- [9] T. Walter, K. Dörr, K.-H. Müller, D. Eckert, K. Nenkov, M. Hecker, M. Lehmann, and L. Schultz, J. Mag. Mag. Mat. **222**, 175 (2000)
- [10] K. Dörr, J.M. Teresa, K.-H. Müller, D. Eckert, T. Walter, E. Vlahov, K. Nenkov, and L. Schultz, J. Phys.: Condens. Matter. **12**, 7099 (2000)
- [11] M. J. Calderón, L. Brey, and F. Guinea, Phys. Rev. B **60**, 6698 (1999)
- [12] S. Valencia, A. Gaupp, and W. Gudat Ll. Abad, Ll. Balcells, and B. Martnez, Appl. Phys. Lett. **90**, 252509 (2007)
- [13] S. Kumar and P. Majumdar, Phys. Rev. Lett. **96**, 016602 (2006)
- [14] N.F. Mott, E.A. Davis, Electronic Processes in Non-Crystalline Materials, Second ed., Oxford Clarendon, 1979

- [15] G.N. Greaves, *J. Non-Crys. Solids* **51**, 87 (1982)
- [16] S. Mollah, G. Anjum, and H.D. Yang, *J. Phys. Chem. Solids* **70**, 489 (2009)
- [17] H.Y. Hwang, S-W. Cheong, N.P. Ong, and B. Batlogg, *Phys. Rev. Lett.* **77**, 2041 (1996)
- [18] A. Gupta, G.Q. Gong, G. Xiao, P.R. Duncombe, P. Lecouer, P. Trouilloud, Y.Y. Wang, V.P. Dravid, and J.Z. Sun, *Phys. Rev. B*, **54**, R15 629 (1996)
- [19] X.W. Li, A. Gupta, G. Xiao, and C.Q. Gong, *Appl. Phys. Lett.* **71**, 1124 (1997)
- [20] M. Ziese, S.P. Sena, C. Shearwood, H.J. Blythe, M.R.J. Gibbs, and G.A. Gehring, *Phys. Rev. B* **57**, 2963 (1998)
- [21] N.F. Mott, *Proc. roy. Soc. London A* **153**, 318 (1936)
- [22] J. Smit, *Physica*, **16**, 612 (1951)
- [23] O. Jaoul, I.A. Campbell, and A. Fert, *J. Magn. Mag. Mat.* **5**, 23 (1977)
- [24] J. O'Donnell, M. Onellion, M.S. Rzchowski, J.N. Eckstein, and I. Bozovic, *Phys. Rev. B* **55**, 5873 (1997)
- [25] Y. Wu, Y. Suzukia, U. Rüdiger, J. Yu, A. D. Kent, T. K. Nath, and C. B. Eom, *Appl. Phys. Lett.* **75**, 2295 (1999)
- [26] T. Taniuchi, H. Kumigashira, M. Oshima, T. Wakita, T. Yokoya, M. Kubota, K. Ono, H. Akinaga, M. Lippmaa, M. Kawasaki, and H. Koinuma, *Appl. Phys. Lett.* **89**, 112505 (2006)
- [27] M. Mathews, F.M. Postma, J.C. Lodder, R. Jansen, G. Rijnders, and D.H.A. Blank, *Appl. Phys. Lett.* **87**, 242507 (2005)

Chapter 5

Mesoscopic transport in (La,Ca)MnO₃ thin films

5.1 Introduction

In the previous chapter, transport properties of La_{0.67}Ca_{0.33}MnO₃ (LCMO) thin films were studied as function of film thickness. We investigated the influence of strain on film properties, which led to several observations. All films exhibit a coupled ferromagnetic metal to paramagnetic insulator transition at transition temperature T_{MI} . The application of strain results in a strong reduction of T_{MI} compared to the bulk value ($T_{MI} \sim 250$ K). A striking result is that films with the same thickness show higher values for T_{MI} when grown on 1° misoriented SrTiO₃ (STO) than on flat STO. We attributed this effect to a higher amount of point defects in films on misoriented STO.

In this chapter we present the transport properties of microbridges which were patterned into the LCMO thin films presented in Chapter 4. We measure the transport properties of microbridges on flat STO, 1° misoriented STO and NdGaO₃ (NGO). Furthermore, the microbridges allow the investigation of LCMO thin film properties down to microscopic length scales. The susceptibility of the M-I transition to chemical and crystallographic disorder (doping disorder, oxygen nonstoichiometry, defects from strain relaxation, twinning, and grain boundaries) can lead to the coexistence of the metallic and insulating phases at a variety of length scales. The presence of this inhomogeneous state, in which conduction is percolative in nature, should be observable in e.g. the current-voltage (I-V) characteristics when these length scales match the physical size of the system. Here we note that the previously defined (Chapter 3) sample nomenclature will also be used in this chapter, to indicate in which film the microbridge was fabricated.

5.2 LCMO microbridges on flat STO

Here we present the transport measurements on LCMO microbridges grown on flat STO substrates with misorientation $< 0.2^\circ$ in random directions and mixed termination. The microbridges were fabricated using the e-beam lithography - the Ar-etching - oxygen plasma treatment process as described in Chapter 3 and in ref. [1]. The microbridge thickness varies between 6 and 20 nm and the width is $5 \mu\text{m}$ for all microbridges (typical length $30 \mu\text{m}$). The resistance is measured in a four point configuration to exclude any effects caused by contact resistances. For all measurements, current sources and nanovoltmeters were used to measure the I-V curves and resistance values. We measured I-V characteristics as function of temperature and in high magnetic fields for all microbridges. From the measurements we can extract resistance behavior for temperatures between $T = 20 - 300 \text{ K}$ and for various current densities, J .

Nonlinear I-V's in the transition

An example of typical temperature dependent resistance behavior $R(T)$, measured at a constant J of $1 \times 10^7 \text{ A/m}^2$ ($I = 0.5 \mu\text{A}$), is shown in Fig. 5.1a for a 10 nm thick microbridge (sample L(10)). Above the transition the resistance shows an exponential dependence as function of temperature. This corresponds to the expected thermally activated polaron hopping. We can extract the activation energy, $E_A = 112 \text{ meV}$ by fitting the high temperature data, as is shown in Fig. 5.1b. Here we note that the values for the activation energies in the microbridges are roughly equal to those of the unstructured films. Microbridge L(10) shows a metal-insulator transition at $T_{MI} = 130 \text{ K}$ (temperature of the maximum resistance value), below which the resistance drops three orders of magnitude before going into the ferromagnetic metallic state. The typical colossal magnetoresistance effect (CMR), a large drop in resistance upon application of $B = 5 \text{ T}$, is observed (see Fig. 5.1a). For most temperatures and in high magnetic fields the I-V curves are linear. However, in the steep part of the transition they show strong nonlinear behavior. A typical example measured at $T = 110 \text{ K}$ is shown in Fig. 5.2a. The nonlinear behavior disappears completely when a high magnetic field is applied. In Fig. 5.2b we show the I-V curve measured at the same temperature in $B = 5 \text{ T}$ field.

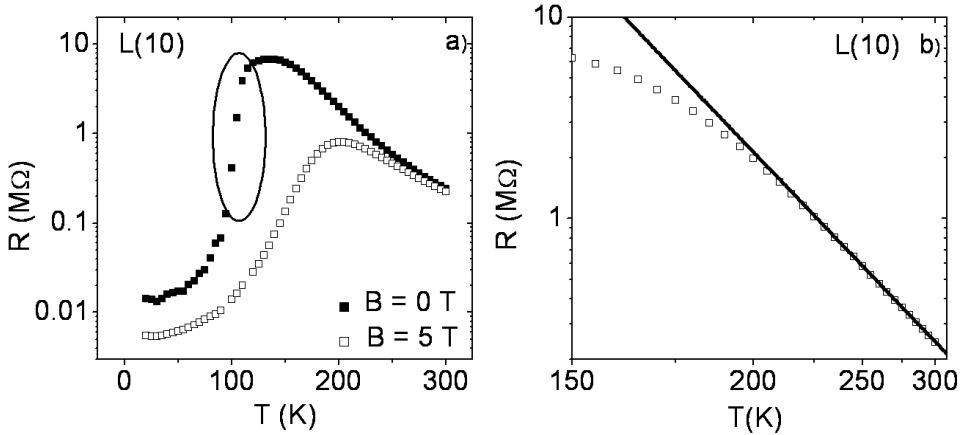


Figure 5.1 — a) Typical $R(T)$ behavior with CMR effect for the $5 \mu\text{m}$ wide microbridge L(10) with $J = 1 \times 10^7 \text{ A/m}^2$. We observe nonlinear I-V curves in the range which is indicated by the ellipse. b) Log R vs. T plot for high temperatures $T = 150 - 300 \text{ K}$. Note: the scale on the T -axis is reciprocal in order to it to $1/T$ -behavior. The solid line is a fit to the data to extract the activation energy, $E_A = 112 \text{ meV}$ for the thermally activated polaron hopping process.

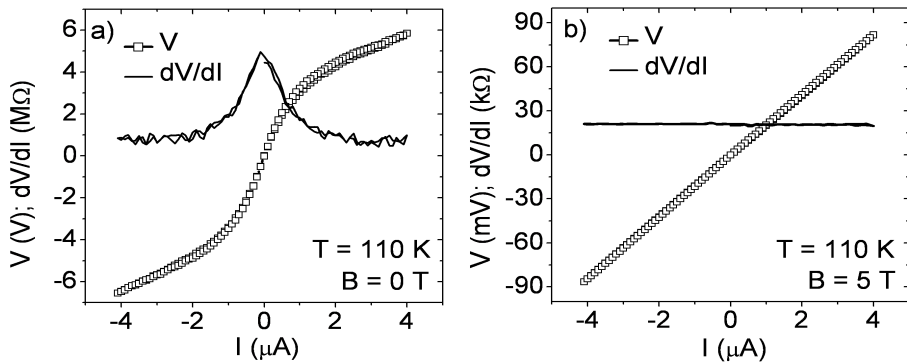


Figure 5.2 — a) (Squares) typical I-V curve in the steep part of the transition (sample L(10)), at 110 K , in $B = 0 \text{ T}$. (Solid line) numerical derivative of the I-V curve. b) The I-V curve at $T = 110 \text{ K}$ measured in $B = 5 \text{ T}$. Note: a current I of $1 \mu\text{A}$ corresponds to a current density $J = 2 \times 10^7 \text{ A/m}^2$.

The nonlinearities are even more apparent in the (numerical) derivatives of the I-V curves. In Fig. 5.2 and Fig. 5.3 we show the differential resistance, $\frac{dV}{dI}$, as function of J at four different temperatures in both $B = 0$ T and $B = 5$ T. At low temperature

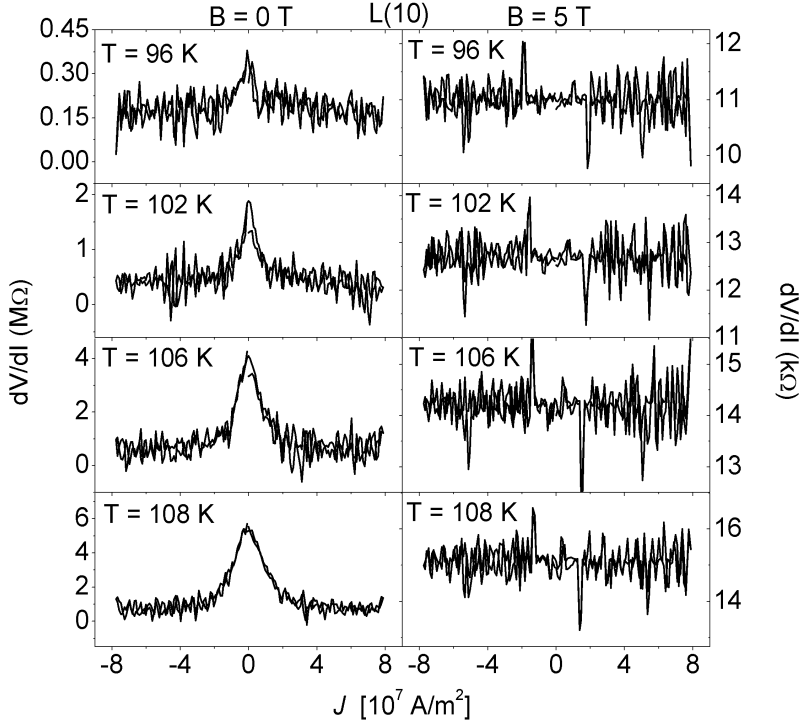


Figure 5.3 — The numerical derivatives of the I-V curves for sample L(10) of which the $R(T)$ behavior is shown in Fig. 5.1. The curves are measured at four different temperatures and in $B = 0$ T (left) and $B = 5$ T (right).

all I-V curves are linear up to $J = 8 \times 10^7$ A/m² ($I = 4$ μ A). Upon warming into the transition the nonlinear behavior starts to occur just before $T = 96$ K and appears to continue until T_{MI} . However, due to the voltage limit of the nanovoltmeter, it is difficult to observe any nonlinear behavior between 115 K - 170 K. Above this temperature range all I-V curves are linear. The effect on the $R(T)$ behavior becomes clear when we directly compare the R vs. T for low (2×10^6 A/m², $I = 0.1$ μ A) and high current density (4×10^7 A/m², $I = 2$ μ A) (see Fig. 5.4a). The dashed line indicates the measurement limit for the high current density measurement. Above this

line the resistance values could not be measured due to saturation of the nanovoltmeter. Application of current results in a shift of the upper part of the transition to

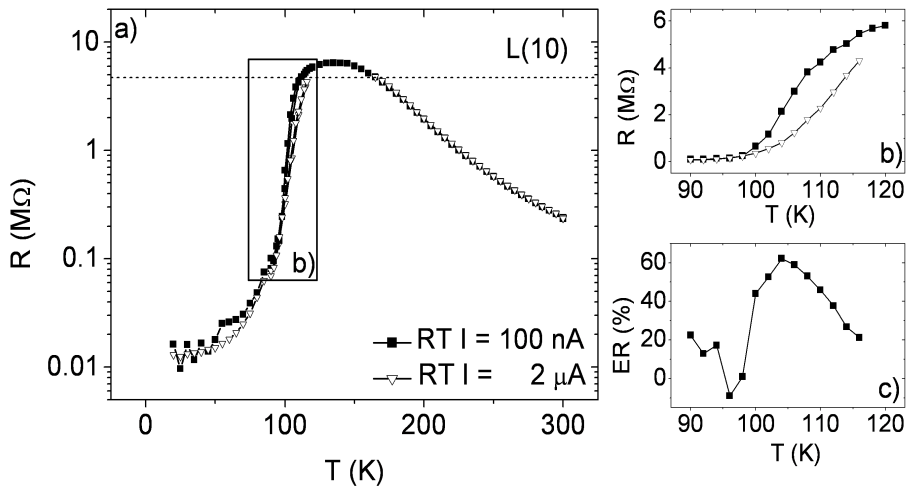


Figure 5.4 — a) $R(T)$ behavior at two different current densities ($J = 2 \times 10^6 \text{ A/m}^2$ and $J = 4 \times 10^7 \text{ A/m}^2$) for microbridge L(10). The dashed line indicates the measurement limit for the high current density measurement. The absence of resistance values above this limit is due to saturation of the nanovoltmeter. b) R vs. T for $T = 90 - 120 \text{ K}$ shows a shift of the upper part of the transition to higher temperature. c) The calculated ER effect as function of temperature.

higher temperature with 5 - 10 K (see Fig. 5.4b). We can calculate the corresponding resistance change (electroresistance, ER) using,

$$ER(\%) = \frac{R_{high} - R_{low}}{R_{low}} \times 100\% \quad (5.1)$$

in which $R_{high(low)}$ are determined at high (low) current density. The ER effect as function of temperature is plotted in Fig. 5.4c for microbridge L(10). We observe a reduction in resistance of 60 % just below T_{MI} . The plot shows that the ER effect first increases as the microbridge is warmed towards T_{MI} but starts to decrease around 105 K, well before T_{MI} is reached at 130 K.

In Fig. 5.5 we plot the differential resistance (at maximum ER effect), normalized with respect to the value at zero bias, as function of applied current density for the three microbridges L(6), L(10) and L(17) (all dimensions: $5 \times 30 \mu\text{m}^2$); the zero bias values are indicated in the caption. The behavior is similar for all three microbridges;

the differential resistance is largest at zero bias, drops with increasing applied current and saturates at roughly the same current density for the different samples. We

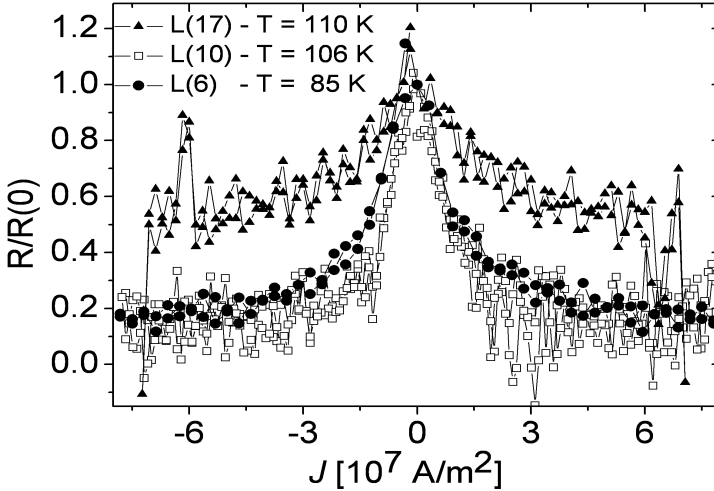


Figure 5.5 — Numerical derivatives dV/dI of the nonlinear I-V curves for three different microbridges on STO. Note: the curves are normalized w.r.t. the zero bias resistivity. For each curve the sample name is indicated as well as the temperature at which the I-V curve was measured. For all films the curves are shown for the temperature where the largest reduction as function of applied current occurred. The zero bias resistances are, L(17): $R(0) = 0.3 \text{ M}\Omega$, L(10): $R(0) = 4.0 \text{ M}\Omega$ and L(6): $R(0) = 4.3 \text{ M}\Omega$.

can extract a second observation from Fig. 5.5: the current-induced reduction in R appears to diminish when the microbridge thickness is increased. For sample L(6) the maximum resistance drop is around 80 % while for sample L(17) it is only 50%. Sample L(20) did not show nonlinear I-V curves in the transition. It was measured in a smaller current density range (up to $J = 1 \times 10^7 \text{ A/m}^2$), but given the sharpness of the feature, it should have been seen in this range, if present.

Magnetoresistance at low temperature

We observe the well known CMR effect around the transition for all microbridges. However, an additional observation can be made. We find that some microbridges also show strong MR effects at low temperature. In Fig. 5.6 we show the $R(T)$ plots for two microbridges L(17) and L(10). For L(10) the application of a $B = 5 \text{ T}$ field leads to a significant reduction in R at low temperature (Fig. 5.6b). Sample L(17)

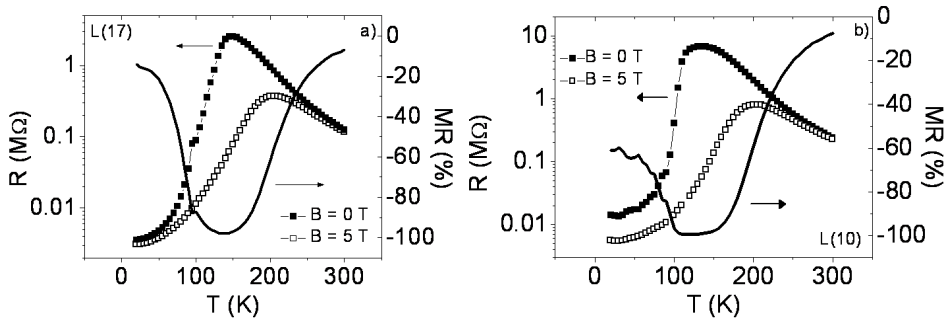


Figure 5.6 — $R(T)$ behavior at $B = 0$ T and $B = 5$ T, for two different film thicknesses. a) L(17) at $J = 3.5 \times 10^6$ A/m² ($I = 0.5$ μ A). b) L(10) at $J = 1 \times 10^7$ A/m² ($I = 0.3$ μ A). Both microbridges have a width of 5 μ m. The calculated MR as function of T is also shown for both samples (solid line).

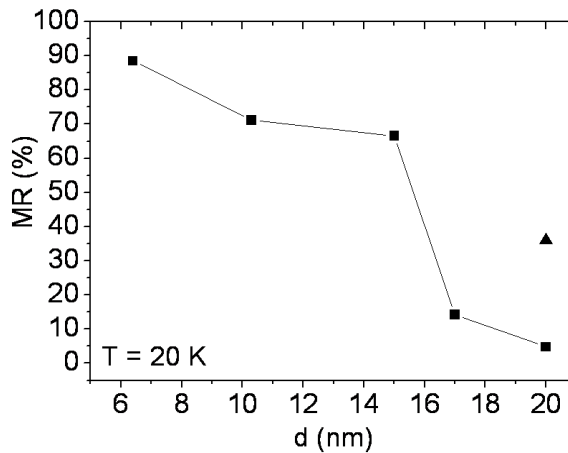


Figure 5.7 — Calculated MR effect at $T = 20$ K as function of microbridge thickness. For L(20) R vs. T is measured in both crystallographic directions ((100) & (010)) of the substrate; both values are indicated (triangle = 010).

(Fig. 5.6a) does not show a large MR effect at low temperature; the $B = 0$ T and $B = 5$ T curves almost overlap. To make this effect more clear we have also plotted the

calculated MR value,

$$MR(\%) = \frac{R(B) - R(0)}{R(0)} \times 100\% \quad (5.2)$$

as function of temperature (see Fig. 5.6 right axes). The values for all microbridges are plotted in Fig.5.7 as function of the microbridge thickness. For L(20) we measured the R vs. T in both (100) and (010) crystallographic directions of the STO substrate which results in two different values for the MR effect. Both are plotted in Fig. 5.7. The strength of the MR effect appears to be dependent on microbridge thickness. The effect increases to almost an order of magnitude for sample L(6).

5.3 LCMO microbridges on NGO

We found strong nonlinear behavior in the transition for microbridges on STO which are fully strained. An almost strain-free situation can be achieved by growing LCMO thin films on the lattice matched substrate NGO. We have measured the transport properties for unstructured thin films (see Chapter 4) as well as 5 μm wide microbridges for film thicknesses of 30 nm (sample L(30)_{NGO}) and 10 nm (L(10)_{NGO}). In Fig. 5.8 we show the transport properties of both microbridges. Sample L(30)_{NGO}

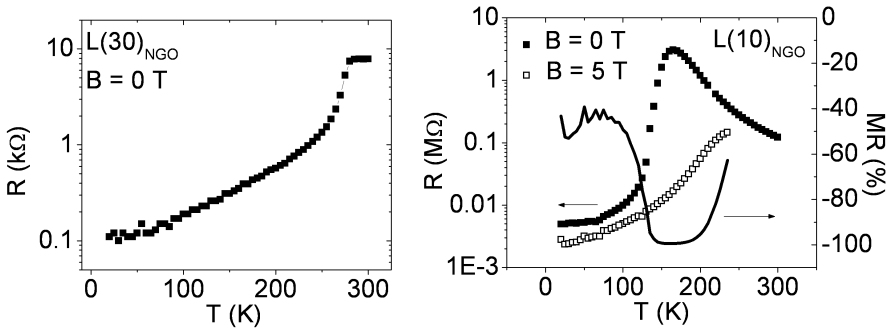


Figure 5.8 — a) R(T) behavior of microbridge L(30)_{NGO} ($J = 7 \times 10^5$ A/m², 0.1 μA). b) R(T) behavior of microbridge L(10)_{NGO} ($J = 2 \times 10^6$ A/m², 0.1 μA) measured in both B = 0 T and B = 5 T. The calculated magnetoresistance as function of temperature is also shown (solid line). Both microbridges have a width of 5 μm .

shows typical R(T) behavior for a strain-free LCMO film, with $T_{MI} = 280$ K around the bulk value. However, microbridge L(10)_{NGO} shows a much lower transition

temperature, $T_{MI} = 165$ K since for films grown on NGO substrates T_{MI} is also dependent on film thickness. Fig. 5.8 also shows that the strength of the low T MR-effect increases (absent in microbridge $L(30)_{NGO}$) when the film thickness is reduced ($L(10)_{NGO}$ MR = -45 %). In Fig. 5.9 we compare the differential resistance vs. current density curve of microbridge $L(10)_{NGO}$ with microbridge $L(10)$. Although measured in a somewhat smaller current density range we find that there is

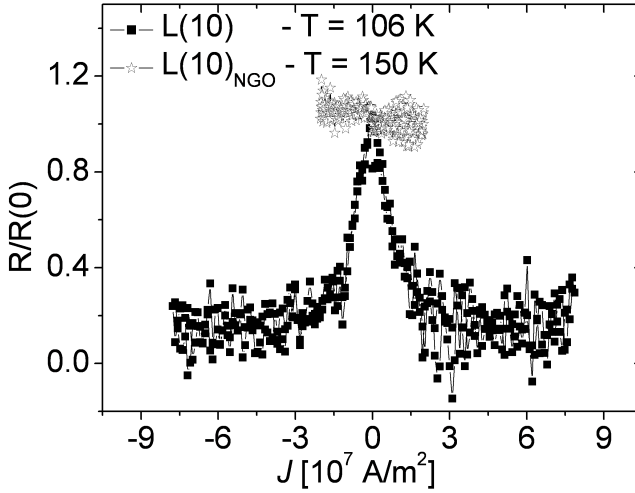


Figure 5.9 — Numerical derivative dV/dI of microbridge $L(10)_{NGO}$ at $T = 150$ K (open symbols). The dV/dI curve for microbridge $L(10)$ at $T = 106$ K (closed symbols) is shown for comparison. Note: the curves are normalized w.r.t. the zero bias resistivity, $L(10)$: $R(0) = 4.0$ M Ω and $L(10)_{NGO}$: $R(0) = 1.6$ M Ω

no nonlinear behavior observed in microbridges on NGO substrates with dimensions down to $5 \mu\text{m} \times 10$ nm.

5.4 LCMO microbridges on 1° STO

In this section we present transport measurements on LCMO microbridges which were patterned on 1° misoriented STO with the microbridge oriented perpendicular w.r.t. the step edges. We inferred (see Chapter 3) that the step edges introduce disorder in the film in the form of point defects. In Fig. 5.10 we show the resistance behavior for two microbridges, $L(7)_{mis}$ (width: $5 \mu\text{m}$) and a 10 nm \times $1 \mu\text{m}$ microbridge

L(10)_{mis} (TiO₂ termination). In both microbridges the resistance behavior shows a

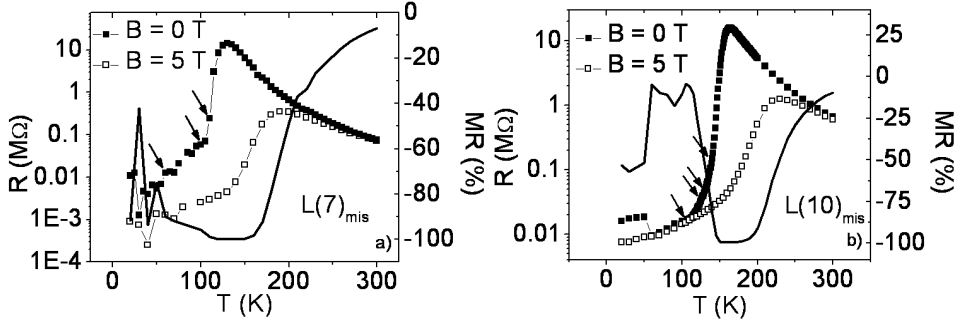


Figure 5.10 — a) $R(T)$ behavior of microbridge $L(7)_{mis}$ ($J = 3 \times 10^6$ A/m², $0.1 \mu\text{A}$), which is $5 \mu\text{m}$ wide. b) $R(T)$ behavior of microbridge $L(10)_{mis}$ ($J = 1 \times 10^7$ A/m², $0.5 \mu\text{A}$), width $1 \mu\text{m}$, grown on singly TiO₂ terminated 1° STO. Both microbridges were measured in $B = 0$ T as well as in $B = 5$ T. The calculated magnetoresistance as function of temperature is also shown (solid line). The arrows indicate the range in which nonlinear behavior is observed.

typical metal-insulator transition and CMR effect. There is a significant increase in the observed T_{MI} compared to bridges on flat STO, $T_{MI} = 163$ K ($L(10)_{mis}$) and $T_{MI} = 130$ K ($L(7)_{mis}$). This result is in line with the measurements on unstructured thin films shown in Chapter 4. Again, we find nonlinearities associated with the transition. The arrows in the Figure indicate the range in which nonlinear behavior is observed. We have determined numerical derivatives for all I-V curves. Fig. 5.11 shows $\frac{dV}{dI}$ as function of J at different temperatures and also in high magnetic field for microbridges $L(10)_{mis}$ and $L(7)_{mis}$. A striking difference compared to the transport properties of microbridges on flat STO is observed. The nonlinear behavior occurs in the onset of the transition, not close to T_{MI} . Differential resistance peaks are observed at zero bias. The shape of the peak is slightly different than found for films on flat STO, in that the differential resistance shows a small undershoot before saturation sets in ($L(7)_{mis}$), or even some increase again ($L(10)_{mis}$). The observed current effects do occur in the same current density range as the microbridges on flat STO. Another observation is that the nonlinear behavior disappears before the steep part of the transition is reached. This becomes more clear in Fig. 5.12 where we show the $R(T)$ behavior ($L(7)_{mis}$) for low and high current density and the corresponding ER effect. In the temperature range $T = 55 - 100$ K an ER effect of 80 - 90 % is observed. The effect decreases to zero before T_{MI} is reached. In the case of the microbridges on flat STO such a pronounced decrease in current effect just below T_{MI} is not observed, which may be due to the measurement limit of the nanovoltmeter.

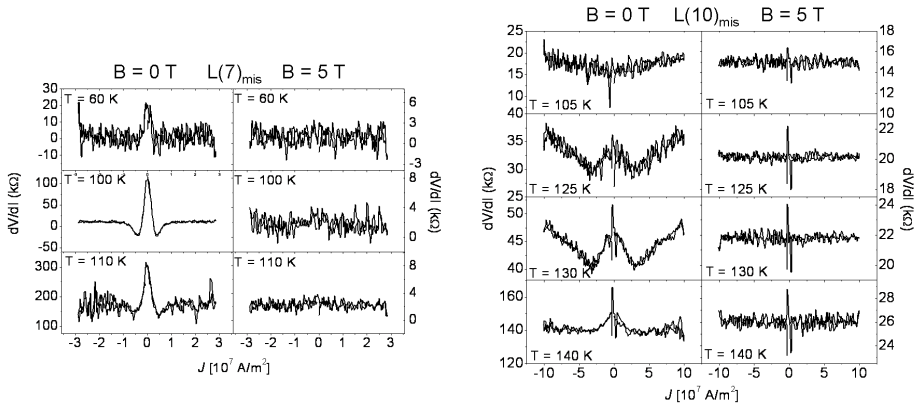


Figure 5.11 — a) Numerical derivatives of the measured I-V curves for 1 μm wide microbridge $L(10)_{\text{mis}}$. b) Numerical derivatives of the measured I-V curves for the 5 μm wide microbridge $L(7)_{\text{mis}}$. For all curves the temperature and the magnetic field at which the curve was measured is indicated.

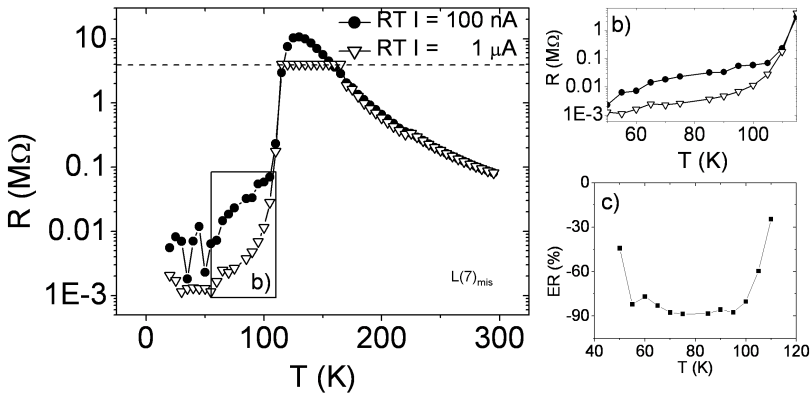


Figure 5.12 — a) $R(T)$ behavior at two different current densities ($J = 3 \times 10^6 \text{ A/m}^2$ (0.1 μA) and $J = 3 \times 10^7 \text{ A/m}^2$ (1 μA)) for microbridge $L(7)_{\text{mis}}$. The larger current density results in a reduction of resistance in the onset of the transition (see inset). The dashed line indicates the measurement limit for the high current density measurement. The absence of resistance values above this limit is due to saturation of the nanovoltmeter. b) $R(T)$ in the temperature range $T = 55\text{-}110 \text{ K}$. c) Calculated ER effect as function of temperature for the 50 - 110 K temperature range.

Finally, (from Fig. 5.10) also for microbridge L(7)_{mis} low temperature magnetoresistance of about an order of magnitude is observed.

5.5 Discussion

The measurements show that the reduced size of the physical system leads to novel behavior which is linked to the metal-insulator transition. For strained microbridges we find strongly nonlinear behavior in the steep part of the transition. We have also investigated how disorder (microbridges on misoriented STO; nonlinearities but at somewhat lower temperature) and strain (microbridges on NGO; no nonlinearities) influence this behavior. Basically, nonlinear behavior as found here under the controlled circumstances of substrate, sample thickness, and bridge width, have not been reported before. Nonlinear behavior was observed recently in thick unstructured and strongly oxygen deficient samples [2], but temperature regime, magnetization and field dependence were all different, and it is difficult to connect that work to our observations. Furthermore, we have shown through characterization (see Chapter 3) that oxygen deficiency is not an issue in our LCMO films. Another concern is the possibility of Joule heating in the microbridge. The peak resistivity for our microbridges is $\rho \sim 10^5\text{-}10^6 \mu\Omega \text{ cm}$ which we use to estimate the effect of Joule heating in the measured current density range. The power which is inserted into the bridge is of the order of μW ; the estimated Joule heating would be in the mK range which is clearly negligible. Furthermore, heating would lead to different nonlinear behavior (increasing resistance with increasing current) and can be ruled out as a possible cause for the observed nonlinearities. A last concern is the the influence of the structural phase transition, tetragonal to cubic, which occurs in the STO substrate at $T = 105 \text{ K}$. Since our LCMO films are epitaxial this could influence microbridge properties. However, we have shown that the observed nonlinear behavior can occur at different temperatures, both above and below $T = 105 \text{ K}$. This indicates that the nonlinear behavior is not an STO-induced effect but intrinsic to the material LCMO.

In Fig. 5.13 we provide the R(T) data of L(10) again, in order to discuss the different regimes we believe are present, c.q. the different states of the microbridge as it is warmed through the metal-insulator transition. At low temperature (region I), the strong MR effects show that an external perturbation, in this case a high magnetic field, can still assist in increasing the metallicity in our microbridge. Clearly, inhomogeneities persist in the microbridges down to low T (also suggested in ref. [3]). The inhomogeneities are shorted by the DE-type metallic state, which exists in the rest of the microbridge, but they are abundant enough to cause an increase in their overall resistivity. Upon warming into the transition the conduction electrons become more

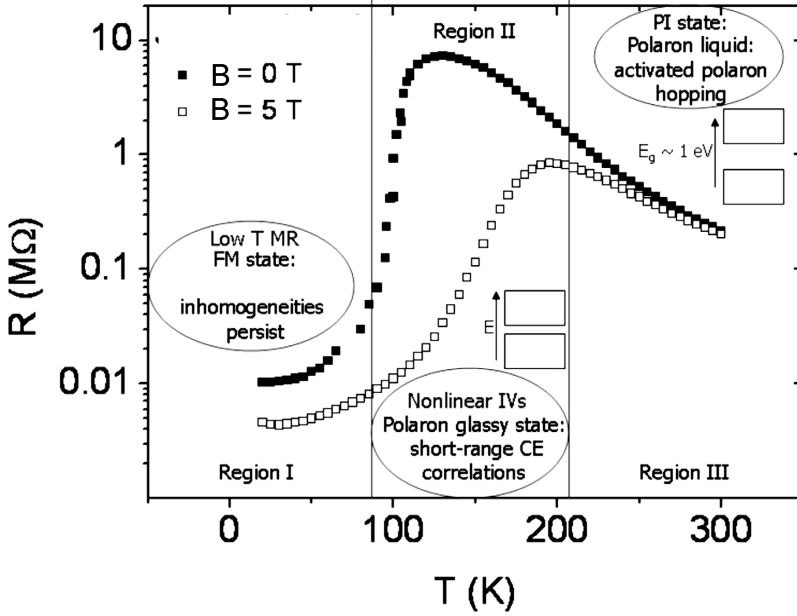


Figure 5.13 — Proposed scheme for the metal-insulator transition in LCMO (R vs. T for microbridge $L(10)$ at $J = 2 \times 10^6 \text{ A/m}^2$). Region I: at low temperature the material is in a FM state but nanoscale inhomogeneities persist. Region II: in the transition e_g electrons are localized by Jahn-Teller splitting resulting in the formation of a glassy state of correlated (CE-type, charge ordered) polarons. Region III: at a certain temperature above the transition the polaron correlations break down and the system becomes a polaron liquid with only single dynamic polarons. In the graph the JT-splitting is indicated with $E_g \sim 1 \text{ eV}$ in the polaron liquid state.

localized, with the Jahn-Teller splitting of the e_g -levels leading to polaron formation. In the steep part of the transition we start to observe strongly nonlinear behavior. The nonlinearities are not hysteretic which means that the voltage drop/increase, when we sweep current density, is fully reversible. The reversibility indicates that the current-driven transition to the metal is not first-order. A scenario in which current transforms a possible antiferromagnetic insulator to a ferromagnetic metal, e.g. through spin torque processes, is not likely. The closeness of the M-I transition in LCMO to a first-order transition [4] would probably render this process hysteretic. The scenario we are looking for is that of an intervening more or less homogeneous phase, which can sustain a voltage difference. Such a phase was actually demonstrated to exist, and is called the polaron glass phase [5]. To understand the origin of this phase, we have to review the phase diagram for LCMO (see Fig. 2.3). At a doping of $x \geq 0.5$ the ma-

material becomes antiferromagnetic and charge and orbital ordered. At lower doping $x = 0.33$ (our material), this ordering is frustrated, but polaron correlations can still occur. In ref. [5] it was shown through neutron scattering experiments that a correlated polaron (glass) phase is formed in LCMO single crystals. The nanoscale structural correlations occur just above T_{MI} . The development of these static (charge ordered, CE-type) polaron structures trap electrons and drive the system into the insulating state. Therefore, this transition has a strong first order component. Our observations show that the correlated regions already start to occur below T_{MI} and become more abundant when the bridge is warmed through the transition. At a certain moment this results in an homogeneous glass phase which fully closes off the microbridge. In this rather homogeneous state the application of current induces a novel type of melting of the charge ordered state which we believe is responsible for the observed strongly nonlinear behavior. We also observe a large CMR effect in the transition; which is, as reported both experimentally [6, 7] and theoretically [8], also directly related to the occurrence of the correlated polaron phase. Much weaker CMR effects are observed in systems with only single dynamic polarons. Warming into region III, the polaron correlations break down (polaron liquid) and conduction is governed by thermally activated (single) polaron hopping.

In the following we discuss how the above mentioned general picture is influenced by microbridge thickness, disorder and strain. We observe several thickness dependencies in our LCMO microbridges. The position of T_{MI} is shifted to lower temperature, the strength of the low temperature MR effect is increased and the low temperature resistivity value (see Table 5.1) is increased when the microbridge thickness becomes smaller. The above mentioned trends appear to be correlated with the occurrence and strength of the observed nonlinear behavior in the transition. When film thickness is reduced the nonlinear behavior becomes more pronounced. The higher values for low T resistivity (and lower values for T_{MI}) indicate an increasing first order component of the transition.

Films on misoriented STO show higher T_{MI} and an increased itinerancy of the microbridge. As discussed in Chapter 4 the introduction of step edges onto the STO surface leads to disorder in the form of point defects. Possibly, when the microbridge tends to become insulating the introduction of density of state inhomogeneities, through defects and impurities, results in the formation of additional conduction channels. This is in line with previous reports [9] which show that metallization of an insulating phase of (La, Ca)MnO₃ is possible by introducing valence variation on the Mn-site or by introducing defects in the parent magnetic state. However, it seems probable that the introduction of disorder also leads to disruption of the formation of the glassy phase. The microbridge is now less homogeneous when

Table 5.1 — Resistivity at $T = 20$ K for samples L(20)-L(6), L(8)_{mis} and L(7)_{mis} and samples L(30)_{NGO} and L(10)_{NGO}. The corresponding values for T_{MI} are also indicated. Note: apart from L(20) ($50 \mu\text{m}$) all values are determined for $5 \mu\text{m}$ wide bridges. The anomalously high value for L(15) is probably caused by damage to the microbridge.

Sample	d nm	T_{MI} (K)	$\rho(T = 20 \text{ K})$ [$10^3 \mu\Omega \text{ cm}$]
L(20)	20	150	1.76
L(17)	17	150	1.53
L(15)	15	125	22.6
L(10)	10.3	130	2.44
L(6)	6.4	110	4.46
L(10) _{mis}	10	163	0.80
L(7) _{mis}	7	130	1.90
L(30) _{NGO}	30	280	0.083
L(10) _{NGO}	10	165	1.23

going through the M-I transition which most probably leads to the occurrence of the nonlinear behavior in the onset of the transition instead of just below T_{MI} . From Table 5.1 we conclude that an increased bandwidth which is associated with larger film thickness, films grown on NGO and films grown on misoriented STO leads to reduced sensitivity to polaronic effects. The formation of correlated regions becomes increasingly difficult as it is counteracted by the enhanced band formation. In the case of microbridges on NGO this leads to absence of nonlinearities since the glassy regions (which remain nanoscopic entities) are shorted by the rest of the microbridge which has higher conductivity, either consisting of ferromagnetic metallic (low temperature) or single dynamic polaron (high temperature) regions.

In the past nonlinear I-V curves have been observed in $\text{La}_{0.8}\text{Ca}_{0.2}\text{MnO}_3$ single crystals [10] and were, although more pronounced at low temperatures, explained as the presence of metastable resistivity states due to the coexistence of different phases. In Chapter 6 we will show through electric field effect experiments that such phase separation also plays a role in our LCMO microbridges. However, we have argued here that the cause for the observed current effects has a different origin, namely current-induced melting of the homogeneous glassy polaron phase.

5.6 Conclusion

When the physical size of an LCMO strip becomes small novel behavior is found in the transport properties. The observed nonlinear behavior is caused by a novel kind

of melting of the insulating state. As a possible explanation, we use the concept of a phase of glassy polarons which is formed in the M-I transition, and which leads to strongly nonlinear behavior when this phase fully and homogeneously closes off the microbridge. We also observe that strain, which inhibits band formation, enhances the polaron correlations leading to lower values for T_{MI} , higher values for the low T resistivity and stronger current effects. The absence of hysteresis in the nonlinearities indicates that the "current melting" is not first order (although probably close) and that the reduction in microbridge thickness even increases the first order component. The introduction of atomic steps on the STO substrate surface and the corresponding point defects in the film inhibit the formation of the glassy polaron regions. However, these microbridges still exhibit nonlinear behavior but that is shifted to the onset of the transition instead of just below T_{MI} . In microbridges on NGO for which strain is absent, the correlations now occur on too small length scales to cause nonlinear behavior in the transition. The physical size of the bridge has to be reduced further to observe the effect.

Bibliography

- [1] C. Beekman, I. Komissarov, M. Hesselberth, and J. Aarts, *Appl. Phys. Lett.* **91**, 062101 (2007)
- [2] S.J. Liu, J. Y. Juang, J.-Y. Lin, K. H. Wu, T. M. Uen, and Y. S. Gou, *J. Appl. Phys.* **103**, 023917 (2008)
- [3] N. Mannella, W. L. Yang, K. Tanaka, X. J. Zhou, H. Zheng, J. F. Mitchell, J. Zaanen, T. P. Devereaux, N. Nagaosa, Z. Hussain, and Z.-X. Shen, *Phys. Rev. B* **76**, 233102 (2007)
- [4] D. Kim, B. Revaz, B. L. Zink, F. Hellman, J. J. Rhyne, and J. F. Mitchell, *Phys. Rev. Lett.* **89**, 227202 (2002)
- [5] J.W. Lynn, D. N. Argyriou, Y. Ren, Y. Chen, Y. M. Mukovskii, and D. A. Shulyatev, *Phys. Rev. B* **76**, 014437 (2007)
- [6] V. Kiryukhin, A. Borrisov, J. S. Ahn, Q. Huang, J.W. Lynn, and S.-W. Cheong, *Phys. Rev. B*, **70**, 214424 (2004)
- [7] V. Moshnyaga, K. Gehrke, O.I. Lebedev, L. Sudheendra, A. Belenchuk, S. Raabe, O. Shapoval, J. Verbeeck, G. Van Tendeloo, and K. Samwer, *Phys. Rev. B* **79**, 134413 (2009)
- [8] C. Sen, G. Alvarez, and E. Dagotto, *Phys. Rev. Lett.* **98**, 127202 (2007)
- [9] K. Pradhan, A. Mukherjee, and P. Majumdar, *Eur. Phys. Lett.* **84**, 37007 (2008)
- [10] V. Markovich, G. Jung, Y. Yuzhelevski, G. Gorodetsky, and Y. M. Mukovskii, *Eur. Phys. J. B*, **48**, 41 (2005)

Chapter 6

Electric field effects in (La,Ca)MnO₃ thin films

6.1 Introduction

In Chapter 5 we presented the magnetotransport properties of La_{0.67}Ca_{0.33}MnO₃ (LCMO) microbridges grown on various substrates. We found large magnetoresistance (MR) effects at temperatures well below the metal-insulator transition and strong nonlinear behavior in the transition. We interpreted this as the signature of the occurrence of a homogeneous glassy polaron phase which can be melted by an applied current density. The reversibility of the melting indicates that the transition is not (although probably close to) first order which may lead to sensitivity to applied electric fields.

There is a special interest in electric field effects. Conventional field effect transistors (FET) consist of semiconductor channels of which the conductivity can be modulated by an electric field applied through a gate positioned on top or below the channel. Materials which are commonly used in FET's are Si with SiO₂ as gate dielectric. The carrier density in a layer (with thickness equal to the screening length for the electric field) at the Si-SiO₂ interface can be controlled by the gate voltage; this leads to modulation of the conductivity between the source and the drain. The demand to fabricate higher circuit densities has led to increasingly smaller feature size. However, the dimensions of these semiconductor microstructures are reaching their intrinsic physical limit. Further increase of circuit density requires the consideration of different materials for the gate oxide, but another direction might be to consider different materials for the channel. Si-based FET's rely on the bandgap deriving from the covalent bonds in the material. Carriers are brought in by doping, and have a low density. In correlated electron systems such as the manganites, the band gap is the result of electron correlations in the d-band (Mott-Hubbard gap). Being able to control this band gap and the large amount of potential carriers could result in

novel FET-type devices.

Field effects have already been investigated in several types of correlated electron systems such as high T_C superconductors [1] and colossal magnetoresistance (CMR) manganites (for a review see ref. [2]). Epitaxial perovskite heterostructures have been used in various FET geometries. For example La_{0.7}Ca_{0.3}MnO₃ thin films were combined with a ferroelectric material (PbZr_{0.2}Ti_{0.8}O₃, PZT) as gate dielectric [3] and the material La_{0.67}Ba_{0.33}MnO₃ [4, 5] was used in a side gate geometry. For the material La_{0.8}Sr_{0.2}MnO₃ (LSMO) [6] (PZT gate) E-field induced modulation of T_{MI} and magnetoresistance behavior is reported. The high carrier density, although desirable, also brings a problem with it. The screening length of the E-field is typically less than 1 nm [6], therefore the manganite layer has to be very thin. In refs. [4, 6] the field effects are attributed to charge carrier density modulation in the manganite channel since a (reversible) shift of T_{MI} upon application of an electric field is observed. The effect is bipolar (i.e. a doping effect) meaning that opposite signs of the gate voltage result in opposite shifts in T_{MI} as expected for a change in carrier density with the electric field. The shift is small. For a film of 3 nm LSMO, a variation of about 10 K could be achieved.

A different effect with the PZT-gate geometry was reported for the material LCMO [7] for which large (in-plane) resistance variations ($\sim 76\%$) are observed in 50 nm thick LCMO films. In the same effort much weaker field effects (few percent) are also presented for devices in which the SrTiO₃ (STO) substrate is used as backgate dielectric. The reported effects are bipolar (and strongly asymmetric w.r.t. the sign of the field) but no shift in T_{MI} is observed. Since the thickness of the film is much larger than the screening length of the electric field the effects are attributed to the presence of a phase separated state. The applied field changes the relative volume fraction of coexisting metallic (M) and insulating (I) regions by accumulating charge at the M-I interfaces. This is contradictory to other reports in which phase separation is correlated with unipolar field effects (i.e. sign of resistance change is the same for opposite signs of the applied gate voltage) for example in La_{0.8}Ca_{0.2}MnO₃ thin films on thinned STO substrates [8]. The effect does not occur at the M-I transition but at lower temperature at a reentrant insulating state. Since the effect is unipolar it cannot be due to doping effects; a pseudogap scenario is suggested. Clearly, there are still some contradictions to resolve.

The investigation of field effects in micron-sized structures could lead to more conclusive results. In this chapter we investigate the response of LCMO microbridges to an applied electric field. We present the device and some issues which occur when STO is used as backgate dielectric and we show the results of the gating experiments.

6.2 STO: backgate dielectric

In conventional field effect transistors SiO_2 is used as a gate dielectric (breakdown field $E_b = 10 \text{ MV cm}^{-1}$ and dielectric constant $\epsilon_r = 3.9$). The material STO can also be used as gate dielectric. This is advantageous since we can fabricate a device consisting of only complex oxides. Furthermore, the relative dielectric constant is two orders of magnitude higher ($\epsilon_r = 310$ at room temperature) compared to SiO_2 . In this section we discuss the device geometry and a few practical issues like electrostriction in the STO and the possibility of leak current through the gate.

6.2.1 The device

The substrates we use are generally 0.5 - 1.0 mm thick and are therefore difficult to use as backgate dielectrics. The required applied gate voltage would be larger than 500 V to create an electric field which would significantly affect the microbridge (see section 6.3). We have followed two different approaches for device fabrication. Directly growing the LCMO film on a two side polished 100 μm thick commercially obtained STO substrate can be done, but film growth (the substrate is glued directly onto a heater surface) is very difficult with such a fragile sample. The other possibility is to mechanically mill down the 0.5 mm thick STO substrate with a microbridge already fabricated on top. The disadvantage in this case is the roughness of the backside of the STO which might interfere with the homogeneity of the electric field. In this chapter the results are all on samples which were milled down after microbridge fabrication process was complete¹. The microbridges were measured before and after the milling procedure; comparison of the results shows that the bridges remain undamaged during this process. The geometry of the measured devices is shown in Fig. 6.1 with the same microbridge structure as was shown in Fig. 3.13. The gate

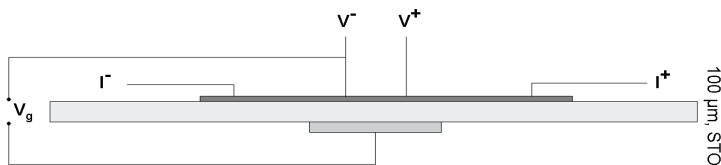


Figure 6.1 — The geometry of the devices for field effect measurements. The STO is mechanically milled down to 100 μm and electrical connections for the measurement are indicated.

voltage V_g is applied between the back of the STO substrate (through a silver paint

¹The milling was performed at Louwers Glass and Ceramic Technologies in Eindhoven

contact) and one of the voltage contacts of the microbridge. In this way we can apply an electric field across the microbridge while measuring the I-V curves.

6.2.2 Electrostriction

Here we note that STO exhibits a cubic to tetragonal phase transition at $T = 105$ K. Our observations and ref. [9] show that the effect of this phase transition on transport properties is small. Fig. 6.2 shows the temperature dependent resistance of sample L(20) (Fig. 6.2: a) unstructured; b) the $5 \mu\text{m}$ wide microbridge). The value for $1/\rho(d\rho/dT)$ (right axis) shows a small effect around 105-100 K which is, only for the microbridge, directly visible as a small peak in $R(T)$. Furthermore, the

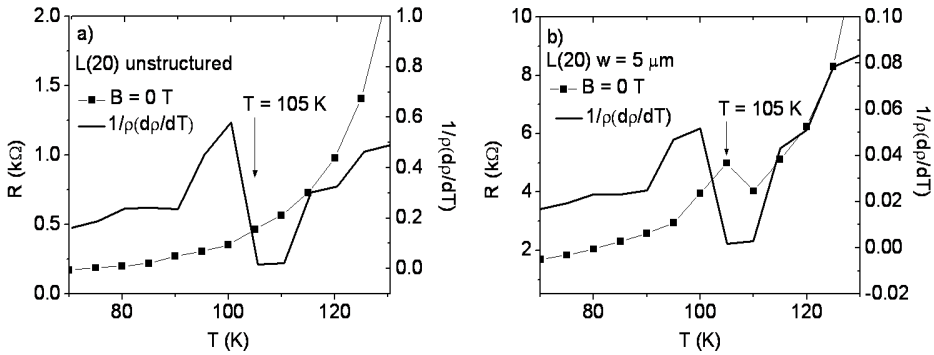


Figure 6.2 — $R(T)$ behavior of sample L(20) a) unstructured and b) microbridge ($w = 5 \mu\text{m}$) between $T = 70 - 130$ K. Right axis: $1/\rho(d\rho/dT)$ (solid line). The position of the phase transition in the STO is indicated by the arrow. Similar behavior is observed in ref. [9].

material is also piezoelectric. When mechanical stress is applied on the material, the deformation induces electric dipole moments, which results in a voltage across the material. The other way around also occurs, when an electric field is applied (e.g. gating experiment) across the material the crystal lattice is deformed. This is called electrostriction. A systematic study of the lattice parameters of STO as function of applied voltage was reported in ref. [10]. The main conclusion was that for increasing applied voltages ($0 \rightarrow 500$ V) a larger volume fraction of the STO is converted from the cubic phase to a distorted phase. This could be a disadvantage for our gating experiment, since the microbridges in our device are epitaxial and therefore fully adapted to the STO substrate. Lattice deformations in the substrate could lead to strain relaxation and defect formation in the film. Furthermore, the

structural distortion in the film and substrate might not be reversible and the device would not be returned to the initial state even after gate voltage has been turned off. Strain-induced resistance variations caused by piezoelectric gate dielectrics have been reported [11, 12]. However, the observed variations are all smaller than 1 %.

6.2.3 Possibility of leak current

Since the STO has defects and impurities we check whether leak current through the gate is an issue in our devices. We monitored the current through the gate at $V_g = 0$ V before measuring I-V curves on the bridge which were taken every 5 K from 20 to 300 K. The same measurement was performed with $V_g = +100$ V and $V_g = -100$ V. The measured gate current I_{gate} is plotted as function of temperature in Fig. 6.3. We find that for $T < 100$ K I_{gate} is zero. However, when warming from

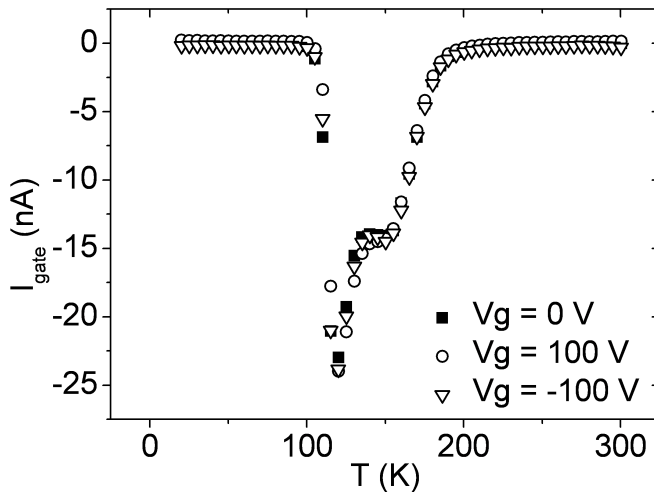


Figure 6.3 — The current measured between the gate voltage contacts upon warming from 20 to 300 K. For the closed squares we did not apply any gate voltage. The open symbols indicate $V_g = 100$ V and $V_g = -100$ V.

$T = 100$ K to $T = 200$ K we find gate currents up to 25 nA even when the applied gate voltage is zero. Above 200 K there is no current flow between the gate contacts. An interesting observation is that the current effects start to occur at $T = 105$ K, the transition temperature for the structural phase transition from cubic to tetrag-

onal. However for a measurement in which I_{gate} was measured *continuously* during thermal cycling we did not observe gate currents. Nor did we observe gate currents when the I-V curves are not measured. This indicates that the observed current is not a leak current due to the application of a gate voltage but rather a discharge current. Apparently, when the temperature of the STO is changed *and* I-V curves are measured in the microbridge, charging occurs in the STO. The measurement of the current between the gate contacts subsequently discharges the STO. A second measurement, on a timescale much faster than 1 sec, does not show a current anymore. At the structural transition the dielectric constant of the STO changes, which would explain the occurrence of the above mentioned results. The observed current effect is small compared to the measurement current in the microbridge. Therefore, it is expected that this will not significantly influence our gating experiment.

6.3 Gating effects in LCMO microbridges

In this section we present the results of the gating experiments performed on two different microbridges ($L(10)$, width = $5 \mu\text{m}$ (see Chapter 5); $L(10)_{gate}$, width = $0.5 \mu\text{m}$) on mechanically milled STO substrates.

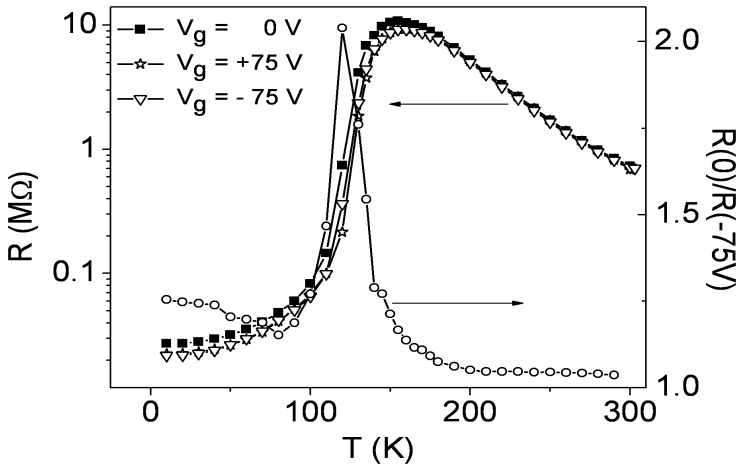


Figure 6.4 — Resistance vs. temperature behavior (left axis) of a $500 \times 10 \text{ nm}^2$ LCMO bridge (sample $L(10)_{gate}$) determined from I-V curves at I around $0.1 \mu\text{A}$. We show curves for three applied gate voltages: $V_g = 0, \pm 75 \text{ V}$. On the right axis the ratio between $R(0 \text{ V})$ and $R(-75 \text{ V})$ is shown. The measurements in this graph were performed by I. Komissarov.

In both cases I-V curves were measured while warming from 20 to 300 K with applied gate voltages of $V_g = 0, \pm 75$ V (this corresponds to a maximum E-field of $E = 7.5 \times 10^5$ V/m). The results for sample $L(10)_{gate}$ are shown in Fig. 6.4a². From

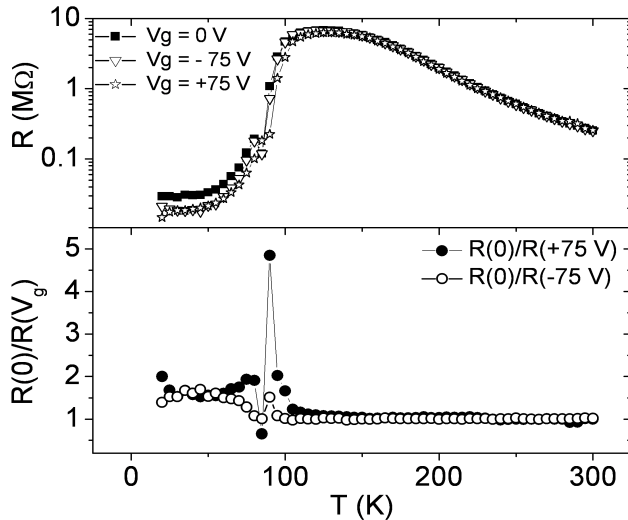


Figure 6.5 — (Top) $R(T)$ behavior of a $5 \mu\text{m} \times 10 \text{ nm}$ LCMO bridge ($L(10)$, see Chapter 4 and 5) measured at $I = 0.1 \mu\text{A}$. We show curves for three applied gate voltages: $V_g = 0, \pm 75$ V. (Bottom) ratio between $R(0)$ and $R(V_g)$ (closed circles: $V_g = +75$ V; open circles: $V_g = -75$ V).

the resistance vs. temperature behavior it is clear that there is a strong electric field effect in the transition around $T = 120$ K and below $T_{MI} \approx 160$ K. The resistance is reduced by a factor of 2 when $V_g = -75$ V is applied. The resistance is also reduced upon application of a positive gate voltage, however, the effect is less strong. The observed effect is unipolar and important to note is that the position of T_{MI} remains unchanged when gate voltages are applied. We have repeated this measurement for sample $L(10)$ (see Chapter 4 and 5). The results are shown in Fig. 6.5. Again we observe an electric field induced reduction of the microbridge resistance in the transition. In this case the effect is quite sharply peaked at $T = 90$ K and the resistance is reduced by a factor of 5 upon application of $V_g = +75$ V. The asymmetry between gate voltage with opposite sign is somewhat larger compared to the microbridge in Fig. 6.4. In both microbridges another effect is observed as well. The electric field

²The measurements on $L(10)_{gate}$ were performed by I. Komissarov

induces a (smaller) reduction in resistance at low temperatures. Again both signs of the gate voltage result in similar resistance changes. Important to note is that once an electric field has been applied the microbridge appears to be irreversibly changed. For the microbridge in Fig. 6.5 we could not recover the low temperature initial state with the higher resistivity after gating. This is also seen from measurements in which a gate voltage sweep was done at constant temperature. The initial zero voltage state

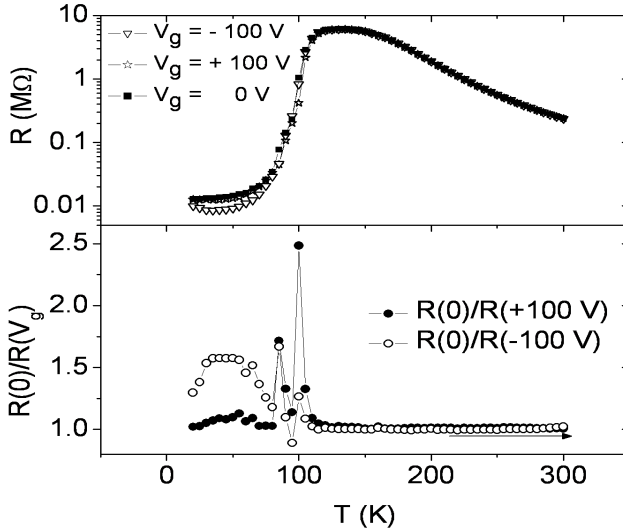


Figure 6.6 — (Top) $R(T)$ behavior of a $5\ \mu\text{m} \times 10\ \text{nm}$ LCMO bridge (L(10), see Chapter 4 and 5) determined from I-V curves at $I = 0.5\ \mu\text{A}$. We show curves for three applied gate voltages: $V_g = 0$, ± 100 V. (Bottom) ratio between $R(0)$ and $R(V_g)$ (closed circles: $V_g = +100$ V; open circles: $V_g = -100$ V).

was not regained. This could be caused by the electrostriction which was mentioned in the previous section. However, we do not see signs of strain relaxation (shift of T_{MI} to higher temperatures) in the microbridge properties after application of an electric field. To check whether the microbridge eventually relaxes back to its initial state we measured the L(10) again at a somewhat larger V_g of ± 100 V. The results are presented in Figs. 6.6 and 6.7. Fig. 6.6 (top) shows the $R(T)$ behavior for different values for V_g (0 V, +100 V and -100 V). The bottom panel shows the ratio $R(0)/R(100\text{V})$ for both signs of the gate voltage. The observed response is again asymmetric w.r.t. the sign of V_g ; $V_g = -100$ V shows a much stronger effect at low temperature while $V_g = +100$ V only shows a response in the transition. The electric

field effect shows two peaks but is again largest in the transition now at $T = 100$ K. Here we note that this occurs at slightly higher temperature compared to before ($T = 90$ K) and the strength of the effect is a factor of 2 smaller. The origin of the double peak is unclear. In Fig. 6.7 we show two I-V curves ($T = 100$ K and $T = 110$ K)

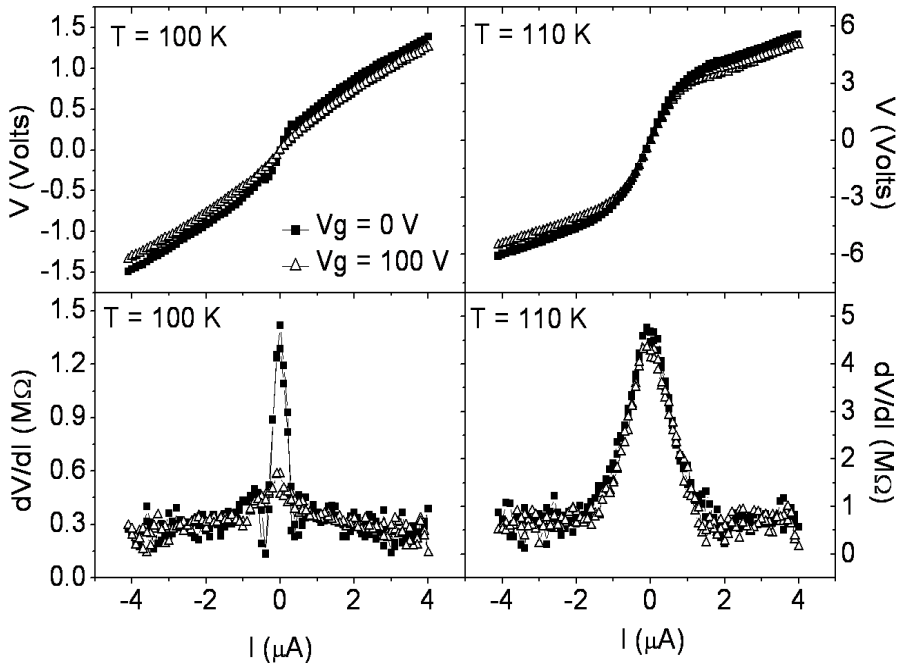


Figure 6.7 — (Top) I-V curves for L(10) at $T = 100$ K and $T = 110$ K. (Bottom) the corresponding numerical derivatives. The figure shows curves for $V_g = 0$ V (closed squares) and $V_g = +100$ V (open triangles).

and their corresponding (numerical) derivatives for $V_g = 0$ V and $V_g = +100$ V. We extract two striking observations from Fig. 6.7. First, at $T = 100$ K the nonlinearities which we associated with the formation of a homogeneous glassy polaron phase start to appear, with a full width of the peak in dV/dI of $1 \mu\text{A}$. From the I-V's and the derivatives it becomes clear that the nonlinearity is suppressed upon application of an E-field. Second, at $T = 110$ K, where the maximum current effect is observed in the I-V (peak width: $4 \mu\text{A}$), the strength and shape of the nonlinear behavior is fully unaltered by application of the E-field.

6.4 Discussion

In this chapter we have observed a strong electric field induced resistance reduction, electroresistance (ER) in the metal-insulator transition and a smaller effect at low T. For both effects the resistance appears to decrease irrespective of the sign of the applied gate voltage. We also observe that T_{MI} remains constant when E-fields are applied. Since our effect is unipolar we attribute the observed ER effects to a form of phase separation. We have shown in Chapter 5 that even at low T inhomogeneities persist in the microbridge. The applied E-field changes the relative volume fraction of the coexisting phases by accumulating charge at the interfaces between them, which can result in the dielectric breakdown of the inhomogeneities. Important to note is that the maximum in the ER effect occurs in the onset of the transition when the nonlinearities start to appear in the I-V curves. On the other hand, when the nonlinear effect has fully developed, the electric field effect disappears. All this takes place in a temperature range of not more than 10 K. Apparently, when the glassy polaron regions start to close off the microbridge the E-field has maximum effect. In this stage a small change in volume fraction of the correlated polaron phase opens the microbridge again for percolation. However, when the glassy phase becomes homogeneous and closes off the bridge (i.e. when strong nonlinear behavior is observed) the E-field does not result in the breakdown of the glassy phase, and therefore the nonlinearities are not altered by the E-field. Here we note that the observed ER effect in the transition is (strongly) asymmetric with respect to the sign of the applied gate voltage. It is possible that doping still plays a role and that asymmetry in hole and electron modulation of inhomogeneities in the microbridge lead to the observed asymmetric behavior. However, the unipolar behavior is dominant. The asymmetry may also be caused by substrate-induced effects like electrostriction; however, this effect would lead to strain variations which should alter T_{MI} (in our experiments T_{MI} remains constant). Another issue could be the possible inhomogeneity of the E-field due to the roughness of the backside of the STO substrate after milling. Here we note another peculiarity, the ER effect at low temperature is irreversible or hysteretic. Once an E-field has been applied the microbridge is not returned to the initial higher resistivity state. This feature makes it impossible to sweep the gate voltage at constant temperature since the initial zero field state is not regained after gating. Clearly, the collapse and rebuilding of the correlated regions is not well controlled [13]. However, the microbridge appears to at least partially relax back to its initial state since remeasuring the gate effect (days later) leads to similar but smaller effects at low T and in the transition. The observed hysteresis is another indication of the closeness to a first order nature of the M-I transition in very thin microbridges.

6.5 Conclusion

We have extracted three important observations from the E-field measurements, ER at low temperatures, a large effect in the transition and disappearance of the field effects when the transport current start to show its nonlinear features. At lower temperatures and in the onset of the transition, the short range polaron correlations form in small regions. These regions can be (partially) melted by the application of an electric field. When the regions start to close off the bridge the field applied across the gate shows maximum effect. The application of the E-field now leads to a change in volume fraction of the glassy phase which results in percolation through the bridge. However, when the microbridge is fully closed off by the glassy phase (i.e. the bridge is homogeneous) the E-field disappears and the strongly nonlinear I-V curves, in the steep part of the transition, remain unaltered even when an E-field is applied.

Bibliography

- [1] C.H. Ahn et al., *Science* **284**, 1152 (1999)
- [2] C.H. Ahn et al., *Rev. Mod. Phys.* **78**, 1185 (2006)
- [3] S. Mathews, R. Ramesh, T. Vankatesan, and J. Benedetto, *Science* **276**, 238 (1997)
- [4] I. Pallechi, L. Pellegrino, E. Bellingeri, A.S. Siri, and D. Marré, *Appl. Phys. Lett.* **83**, 4435 (2003)
- [5] I. Pallechi, L. Pellegrino, E. Bellingeri, A.S. Siri, D. Marré, A. Tabano, and G. Balestrino, *Phys. Rev. B* **78**, 024411 (2008)
- [6] X. Hong, A. Posadas, A. Lin, and C. H. Ahn, *Phys. Rev. B*, **68**, 134415 (2003)
- [7] T. Wu, S.B. Ogale, J.E. Garrison, B. Nagaraj, Amlan Biswas, Z. Chen, R.L. Greene, R. Ramesh, and T. Venkatesan, *Phys. Rev. Lett.* **86**, 5998 (2001)
- [8] M. Eblen-Zayas, A. Bhattacharya, N.E. Staley, A.L. Kobrinskii, and A.M. Goldman, *Phys. Rev. Lett.* **94**, 037204 (2005)
- [9] M. Egilmez, M. M. Saber, I. Fan, K. H. Chow, and J. Jung, *Phys. Rev. B*, **78**, 172405 (2008)
- [10] D.C. Meyer, A.A. Levin, S. Bayer, A. Gorbunov, W. Pompe, and P. Paufler, *Appl. Phys. A*, **80**, 515 (2005)
- [11] C. Thiele, K. Dörr, and L. Schultz, E. Beyreuther, and W.-M. Lin, *Appl. Phys. Lett.* **87**, 162512 (2005)
- [12] R. K. Zheng, Y. Wang, H. L. W. Chan, C. L. Choy, and H. S. Luo, *Appl. Phys. Lett.* **90**, 152904 (2007)
- [13] S. Dong, C. Zhu, Y. Wang, F. Yuan, K.F. Wang, and J.-M. Liu, *J. Phys. Condens. Matt.* **19**, 266202 (2007)

Chapter 7

Putting the pieces together

The results which we presented in Chapters 3-6 led to many observations. Here we summarize the major findings and where possible interconnect them. We started in Chapter 3 with the characterization of our $\text{La}_{0.67}\text{Ca}_{0.33}\text{MnO}_3$ (LCMO) thin films grown on various substrates. A general feature for both strained (SrTiO_3) and unstrained (NdGaO_3) films is the formation of a substrate-film interface layer of reduced Mn-valence to compensate for Madelung potentials caused by charge mismatch between the film and the substrate. In Chapter 4 we were able to directly correlate this layer with a reduced value for saturation magnetization of our films. The compensation layer is clearly a magnetically dead or weak layer. Apart from reducing the effective thickness of the film the interface layer does not appear to have a large influence on transport properties.

In Chapters 5 and 6 we found novel behavior in LCMO microbridges in the form of strong nonlinear behavior in the steep part of the transition. The nonlinearities are attributed to a novel type of current-induced melting of the intervening glassy polaron phase which is formed when the microbridge is warmed into the M-I transition. This correlated polaron phase is similar to the charge ordered state at higher doping levels. The sensitivity to E-fields occurs in the phase separated state and is maximal when the correlated regions become comparable to the physical size of the microbridge. Once the bridge becomes too homogeneous the E-field does not lead to dielectric breakdown of the glassy phase. The strong nonlinear behavior just below T_{MI} remains unaltered when an E-field is applied. Therefore, an important finding is that the phase separation which is associated with the M-I transition in LCMO microbridges leads to sensitivity to applied electric fields but is not responsible for the observed nonlinearities (c.q. the nonlinearities are not caused by current-induced percolation). The observed novel behavior in LCMO microbridges is directly correlated with the small bandwidth of this system. This leads to clear trends in transport properties such as the strain-induced reduction of the transition temperature T_{MI} (T_C) with decreasing film thickness which is directly coupled to increased values for

the low T resistivity. The absence of strain (NGO) and the introduction of unit-cell high steps on to the STO surface (c.q. point defects) leads to an enhancement of T_{MI} compared to films on flat STO. These trends indicate that the application of strain and reduction of film thickness results in an increase of the first order component of the transition. This coincides with the observation that the nonlinear behavior becomes more pronounced for the very thin ($d < 15$ nm) microbridges. In contrast, materials such as $\text{La}_{0.67}\text{Sr}_{0.33}\text{MnO}_3$ (LSMO) with larger bandwidths are less sensitive to electron-phonon coupling and Coulomb correlations. The M-I transition in such materials is second order in nature. Therefore, it is expected that thin films of LSMO on STO have much less (or no) tendency to phase separate nor to form the intervening glassy phase. Our expectation is that LSMO does not exhibit the nonlinear behavior and the unipolar E-field effect even for very thin films. However, nonlinear behavior is expected for the smaller bandwidth materials which are obtained when the doping level of $(\text{La,Ca})\text{MnO}_3$ is reduced. For example for $x = 0.18$ the material is charge ordered at low temperatures therefore compositions near this phase boundary provide interesting materials for further study of the observed glassy phase and possible E-field effects.

Appendix: (La,Ca)MnO₃ nanowires, growth process and preliminary findings

A.1 Introduction

We have observed nonlinear behavior in the metal-insulator transition for La_{0.67}Ca_{0.33}MnO₃ (LCMO) microbridges on STO substrates. We ascribe this behavior to the formation of an intervening glassy polaron phase in the transition. The condensation of the correlated polaron regions occurs on mesoscopic length scales and is a generic feature of the material LCMO. Given the various effects (nonlinear transport, low-temperature magnetoresistance) we found in LCMO microbridges on STO, it can be of interest to investigate LCMO nanowires. Moreover, according to Shankar et al [1] the transition temperature in such wires is shifted to higher temperatures compared to the bulk transition temperature, even to above room temperature! In this chapter we present a recipe for LCMO nanowire fabrication in which a sol-gel (liquid) is brought into the pores of an Al₂O₃ template. Furthermore, we present Scanning Electron Microscopy (SEM) images for characterization and preliminary magnetization measurements which were performed in a MPMS (Magnetic Properties Measurement System, Quantum Design) with the field directed along the pore direction. The goal is to measure the transport properties of single LCMO nanowires, which was not measured in [1]. However, we could not reproduce the basic results of Ref. [1], as will be detailed below.

A.2 Growth process

A.2.1 The sol-gel process

The growth process for nanowires is a template assisted sol-gel process. A stoichiometric solution is used consisting of the elements that make up the material of the wire. An additional ingredient to the solution is a polymer. The polymer, in this case

ethylene glycol (EC), is necessary to serve as a backbone for the nanowire nucleation process. The solution is prepared within a specific viscosity range by heating it, after which the sol is brought into the pores by emerging the template. Ideally, the sol penetrates the template, filling the pores fully. Subsequently the filled template is heated to higher temperatures to crystallize the correct phase. An advantage of the sol-gel process is the relatively low temperature at which this phase forms ($> 600^\circ\text{C}$). For comparison, conventional solid state methods for making polycrystalline material require temperatures $T > 1000^\circ\text{C}$. The nanowire growth process is shown in Fig. A.1 (taken from [1]). Two different nucleation processes are shown in the

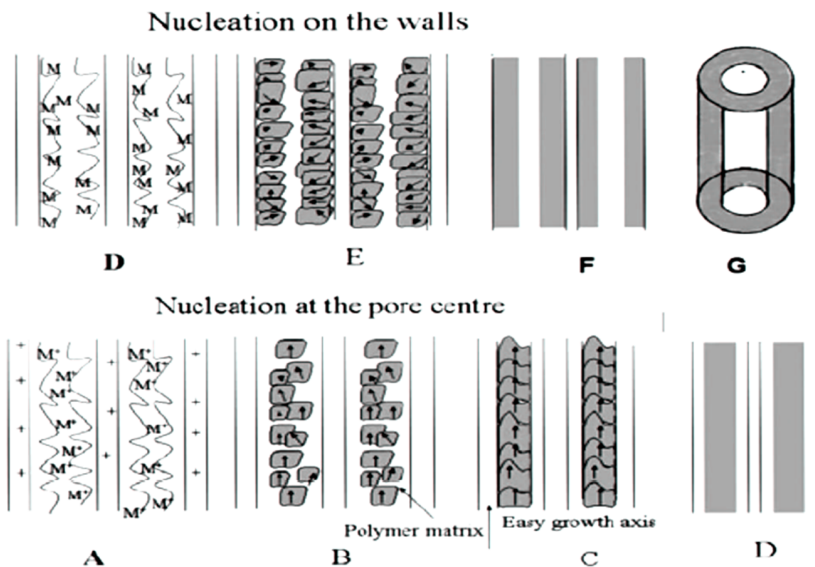


Figure A.1 — Two possible growth processes for nanowires inside the pores of a template. Top (D-G): growth when nucleation starts on the walls of the pore. This will result in a polycrystalline shell wire. Bottom (A-D): Nucleation commences in the pore center and results in a single crystalline wire. Taken from [1].

figure. In both cases, when the template is heated to higher temperature, the EC polymerizes and cation complexes nucleate along the polymer. However, the nucleation of the final phase of the material can either start on the pore walls (top panel) or in the center of the pore (bottom panel). Wall nucleation will result in a polycrystalline shell nanowire. When nucleation can be forced to commence in the pore center the nanowires should be single crystalline. Reportedly, Shankar et al [1] have successfully grown $\text{La}_{0.67}\text{Sr}_{0.33}\text{MnO}_3$ (LSMO) and LCMO nanowires using anodized

Al₂O₃ templates. The stoichiometric solution consisted of lanthanum, strontium and manganese nitrates dissolved in water and ethylene glycol. The anodization of the template results in a positively charged template which induces pore-center nucleation. We have used this recipe as our starting point for nanowire fabrication.

A.2.2 Templates and pores

Choosing the proper template and the corresponding pore characteristics is important for nanowire growth. In the case of [1] anodized alumina was used to serve as template. The template should have certain properties to be useful in growth processes. It should be able to withstand high temperatures (> 600°C), which is necessary to form the perovskite phase, while remaining mechanically stable. Such templates are commercially available [2]. We have investigated three possible templates for the nanowire growth process. We used a FEI nanoSEM to characterize them and in the following paragraphs we will present the characteristics of the various templates.

Commercial anodized alumina

We have used commercial alumina templates from Whatmann. These templates are hydrophillic inorganic membranes designed as biological filters with the following properties, template thickness: 60 μm , diameter: 13 mm , nominal pore size: 100 nm, pore density: 25 - 50 % , maximum service temperature: 400 °C. The corresponding SEM images are shown in Fig .A.2. From the cross-sectional views (Fig. A.2a,b and c) it is clear that the pores intersect each other and that a filter layer is present on one side of the membrane with nominal pore size of ~ 20 nm. This could seriously hamper effective filling of the pores with the prepared solution. Furthermore, the surface of the membrane is rough and pores are not well ordered in a hexagonal lattice [3]; some are bunched into pores with larger diameter.

Custom made anodized alumina

We have also looked into the possibility to use custom made anodized alumina templates. The membranes shown in this paragraph were fabricated in Halle in the group of Prof. Dr. K. Nielsch [4]. The membranes were prepared in 1wt% phosphoric acid and have a thickness of 40 μm, an inter-pore distance of 500 nm and a pore diameter of 190 nm (see Fig. A.3 and ref. [5]). These templates show straight pores through the entire thickness of the membrane and the usual hexagonal ordering of the pores.

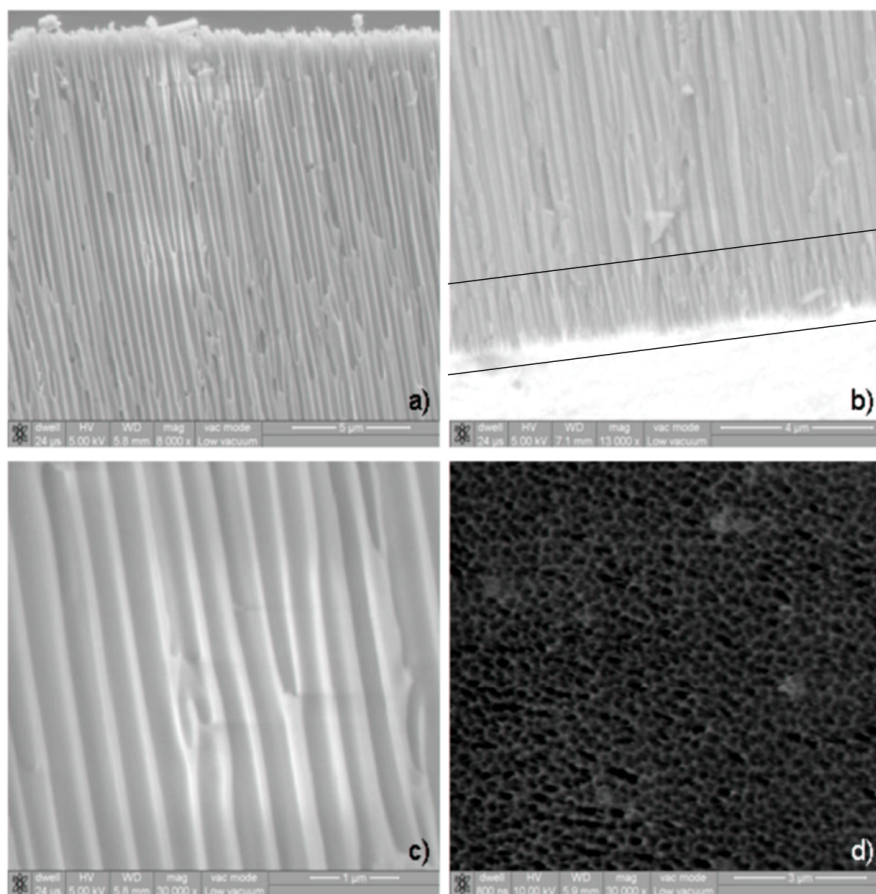


Figure A.2 — SEM images of anodized alumina bought from Whatmann. a) b) and c) are cross-sections of the template at different magnifications: 8000x, 13000x, and 30000x respectively. Image b) shows the presence of a filter layer with pore size ~ 20 nm indicated by the two lines. d) Top view of the template showing a rough surface.

Polycarbonate templates

Another possible template which can be used in the fabrication of LCMO nanowires is polycarbonate (PCB) (also commercially available). The SEM images in Fig. A.4 show the characteristics of the polycarbonate template. The PCB membranes have the following properties, thickness: $6 \mu\text{m}$, average pore size: 50 nm, pore density: 1×10^5 to 6×10^8 pores/ cm^2 and maximum service temperature: 140°C . The templates are coated with polyvinylpyrrolidone (PVP) to make them hydrophilic. Because of the

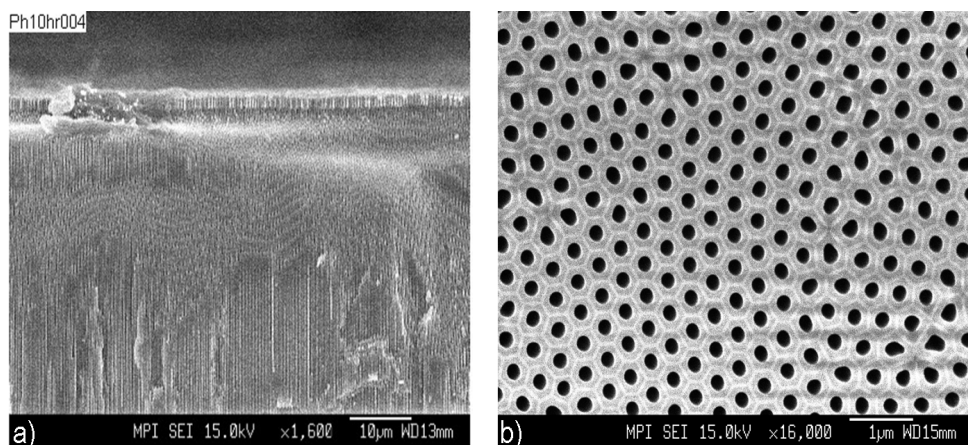


Figure A.3 — SEM images of anodized alumina fabricated in Halle. a) Cross-sectional view of the membrane (magnification: 1600x). b) Top view of the template (magnification: 16000x).

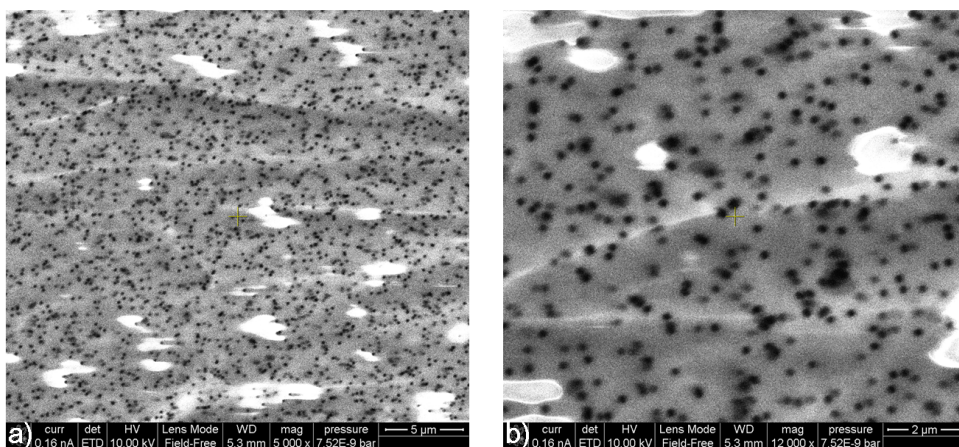


Figure A.4 — SEM images of the polycarbonate template. a) Top view magnetification: 5000x. b) Top view of the template at magnification: 12000x.

low maximum service temperature the membrane will disintegrate during the calcination process. If the wires are already formed during the low temperature stages, we can use this template. However, the disadvantage is that after the growth process the wires are not aligned which makes characterization through magnetization measurements difficult.

A.3 LCMO nanowires

In this section we present SEM images of templates after the nanowire growth process. For each template we used similar recipes for the solution but solution viscosity and temperature during the calcination process were varied.

A.3.1 Viscosity

We measured the viscosity as function of heating time of the sol using a rheometer Physica MCR 501. The following stoichiometric composition was used:

- $\text{La}(\text{NO}_3)_3 = 3.089$ gr; molecular weight: 433.02 g / mol; atomic weight La: 138.9
- $\text{Mn}(\text{NO}_3)_2 = 4.427$ gr; molecular weight: 164.09 g / mol; atomic weight Mn: 54.9
- $\text{Ca}(\text{NO}_3)_2 = 1.684$ gr; molecular weight: 178.95 g / mol; atomic weight Ca: 39.96
- $\text{H}_2\text{O} = 8$ ml; molecular weight: 18.02 g
- ethylene glycol = 9.5 ml; molecular weight: 62.068 g / mol

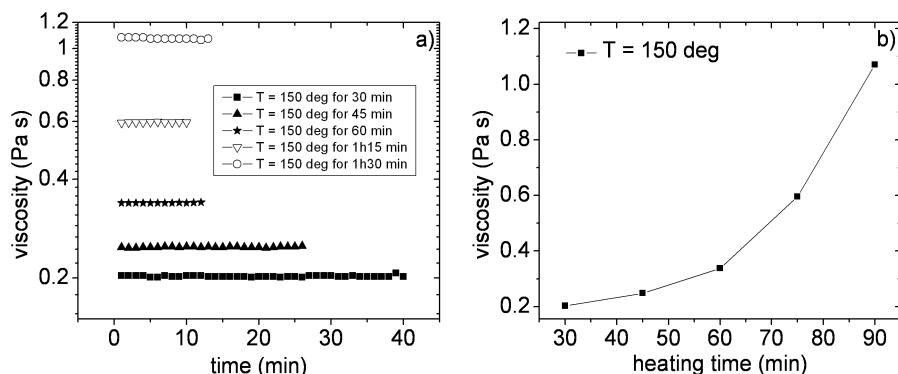


Figure A.5 — a) Viscosity as function of measurement time for the solution which was kept at 150 °C for different durations. The sol is not heated during the measurement. b) Viscosity vs. heating time at T = 150 °C.

The sol was kept at $T = 150\text{ }^{\circ}\text{C}$ on a hotplate for different amounts of time. The viscosity was measured directly after taking the sol off the hotplate. In Fig. A.5 we show the viscosity of this sol for the different heating times. In Fig. A.5a we measured the time dependence since the sol is still cooling after taking it off the hotplate. Apparently, the viscosity increase is not reversed when cooling back to room temperature. Fig. A.5b shows the viscosity dependence on heating time (at $150\text{ }^{\circ}\text{C}$). It varies between $\sim 10\text{ mPa s}$, for the unheated sol, to 1.08 Pa s for the sol which is heated for 1h and 30 min. For comparison the viscosity of water is 1 mPa s .

A.3.2 Commercial anodized alumina template

In this section we show both SEM results as well as magnetization data for a typical nanowire growth process. The stoichiometric solution, mentioned in section A.3.1, was heated to $150\text{ }^{\circ}\text{C}$ for 1h and 30 min with continuous stirring. In our case simple emersion of the template in the sol did not result in any filling of the pores, but only covers the surface of the template. Therefore, we have developed a setup in which a pressure difference was applied across the template to pull the sol through the pores. After filling, the template surface is wiped clean and the template is dried at $120\text{ }^{\circ}\text{C}$, after which it is filled again using the same procedure and the same sol. Next, the template is placed in a furnace (in air) where it is heated with a rate of $3\text{ }^{\circ}\text{C}/\text{min}$ to $700\text{ }^{\circ}\text{C}$ at which it stays for 5 hours; it is subsequently cooled with a rate of $5\text{ }^{\circ}\text{C}/\text{min}$. The ethylene glycol polymerizes around $200\text{ }^{\circ}\text{C}$ and has an auto-ignition temperature of $410\text{ }^{\circ}\text{C}$. The corresponding SEM images which were recorded directly after growth are shown in Fig. A.6. From the images it is observed that only particles (see arrow in Fig. A.6) are formed in the pores. Both increasing or decreasing the viscosity of the sol did not improve the filling fraction of the pores. For an additional example of an attempt to grow LCMO nanowires in commercial templates now with the sol at significantly higher viscosity, see Fig. A.7. For this growth process the filling fraction seems slightly higher. However, there is a strong gradient of the filling fraction across the template. The fraction is higher at the side of the template which contains the 20 nm filter layer. We were unable to grow continuous structures in these templates. Furthermore, for both samples we measured the magnetic properties, with the applied magnetic field directed along the pore direction. The results are shown in Fig. A.8. The measurement includes the material which is in the pores as well as on top of the template. From the magnetization as function of temperature and of applied magnetic field we observe that the material inside the membranes is ferromagnetic with a transition temperature around 260 K . The measured Curie temperature corresponds to the bulk transition temperature of LCMO which is expected from the prepared stoichiometry of the initial solution. Furthermore, we observe an upturn in

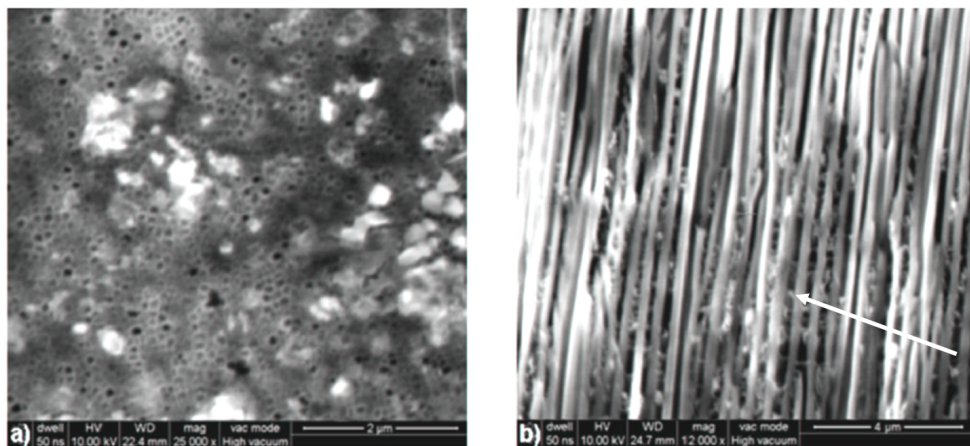


Figure A.6 — SEM images of a template after filling of the pores (sol heated to 150 °C for 1h 30 min) and after heating to 700 °C for 5 hours in air. The arrow indicates the particles which are in the pores. a) Top view. b) Cross-sectional view.

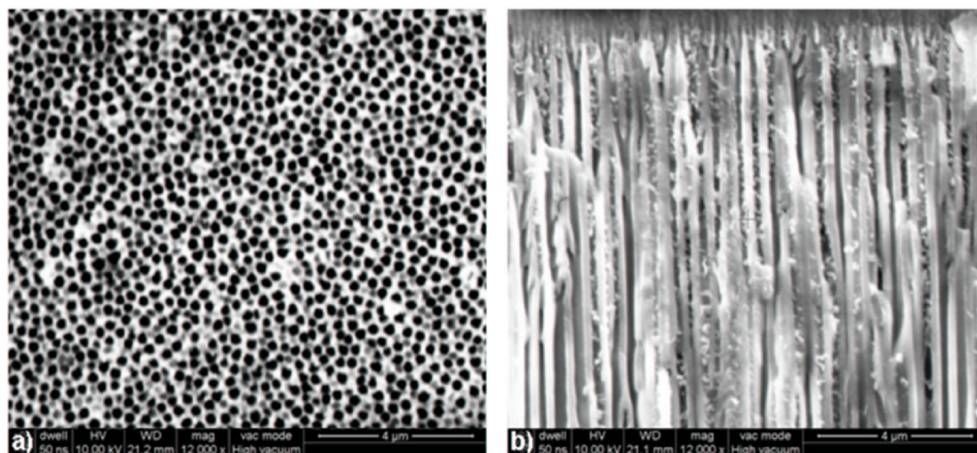


Figure A.7 — SEM images of a template after filling of the pores (sol heated to 150 °C for 1h 50 min) and after heating to 700 °C for 5 hours in air. a) Top view. b) Cross-sectional view.

magnetization vs . temperature at low T for all measured samples. Mandal et al. [6] showed that ferrite nanoparticles exhibit an upturn in saturation magnetization at low temperature. This effect was reportedly caused by the quantization of the spin-wave spectrum due to the finite size of the particles. We have not measured the saturation magnetization of our samples. However, our observation does confirm that our filled

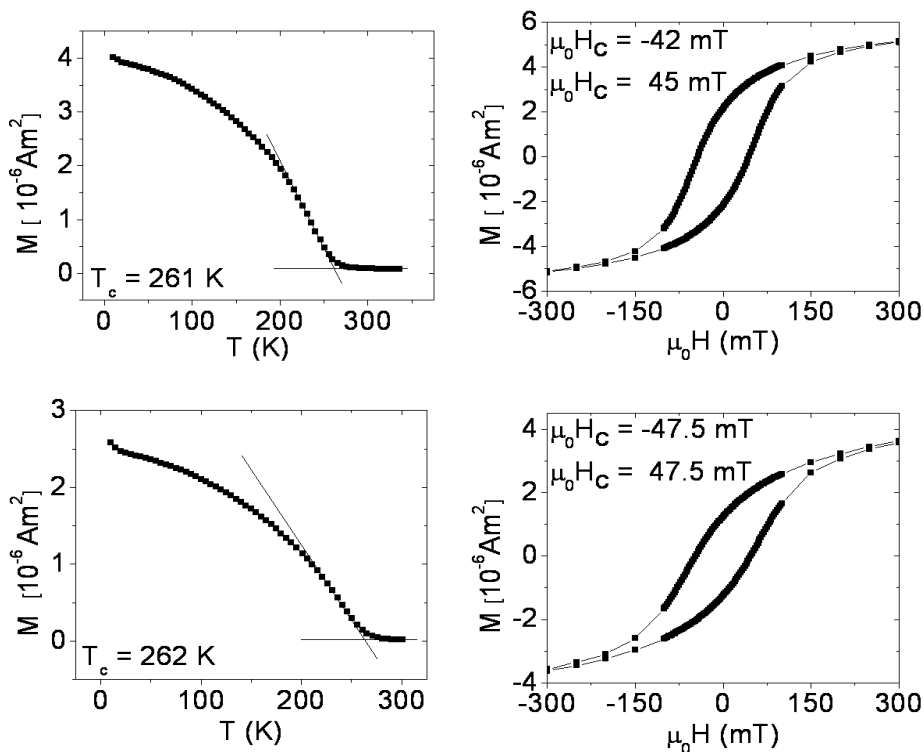


Figure A.8 — Magnetic properties of LCMO material inside the pores and on top of the alumina, which were filled and heated according to the recipe stated in section A.3.1. Top: template filled with 1h 50 min heated sol. Bottom: template filled with 1h 30 min heated sol. M vs. T was measured in $B = 0.1$ T and M vs. B at $T = 10$ K.

templates contain LCMO nanoparticles.

A.3.3 Custom anodized alumina template

The pores and walls of the commercial template are quite disordered. This could result in nucleation at the pore walls leading to very polycrystalline nanowires. We only managed to fabricate nanoparticles but no nanowires in the commercial template. Therefore, we tried to use anodized alumina templates which have a self-ordered hexagonal pore structure. These templates (see Fig. A.3) have straight pores with smooth walls throughout the template. Furthermore, the somewhat larger pore size

could improve the filling fraction. In this section we show the SEM results (see Fig. A.9) on one sample starting with the stoichiometric solution mentioned in section A.3.1. Although the surface was wiped clean after the filling of the template, bub-

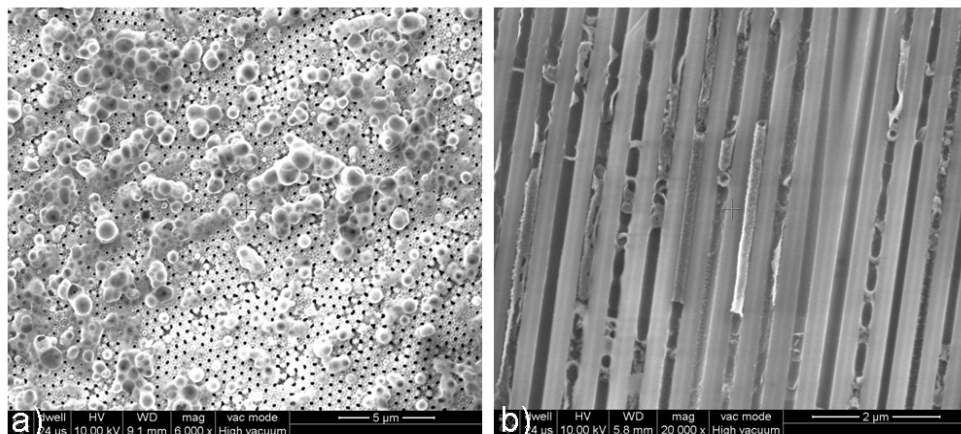


Figure A.9 — SEM images of a template after filling of the pores (sol heated to 150 °C for 1h) and after heating to 600 °C for 5 hours in air. a) Top view. b) Cross-sectional view.

bles of material are observed on top. Apparently, during the calcination process sol is pushed out of the pores. From the cross-sectional view we do observe formation of a continuous structure, which is 2 μm long. However, despite the applied pressure difference during filling, the filling fraction of the pores is still poor. Possibly, the pores do get filled initially, but the sol is pushed out upon calcination. Perhaps, the confinement that the template imposes on the sol (nanowires) and the different thermal expansion coefficients of the system interfere with nanowire growth. We did perform magnetization measurements on these templates with the field directed along the pores. Fig. A.10 shows the magnetic properties for two templates. The measurements include both the material which is in the pores as well as the material on top of the template (see Fig. A.9a). The difference between the samples is the heating time before filling the template. The sample shown in the top panel was heated for 1h while the one in the bottom panel was heated for 1h 30 min. For the first sample, although we did find some continuous structures in the template (Fig. A.9b), the magnetic properties do not show ferromagnetic behavior. However, the second sample, which only showed nanoparticles in the template, did show clear ferromagnetic behavior with a T_C of 255 K, close to that of bulk LCMO and the low T upturn. Apparently, the heating time of the sol before filling is not only important to control the viscosity of the solution but also changes the solid content of the sol which might

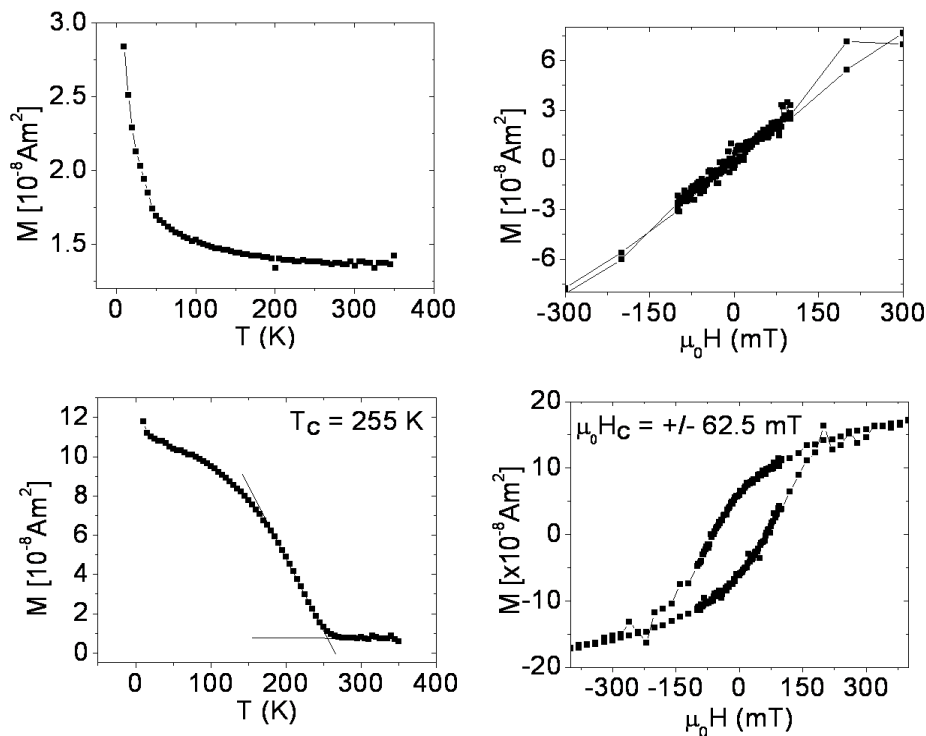


Figure A.10 — Magnetic properties of two templates, which were filled according to the recipe given in section A.3.1. Heating times of the sol before filling were different. The measurement includes material in the pores as well as on top of the template. Top: template filled with 1h heated sol. Bottom: template filled with 1h 30 min heated sol. Furthermore, the calcination of these templates was done at 600 °C for 5 h. M vs. T was measured in $B = 0.1$ T and M vs. B at $T = 10$ K.

influence the magnetic properties.

A.3.4 Polycarbonate template

The confinement of the sol during calcination might hamper the formation of nanowires of the correct phase. Therefore, we tried to use polycarbonate templates as well (see also ref. [7]). Since this template is flexible it is supported by placing it on a Si substrate during the calcination process. The template disintegrates already in the low temperature stage ($T \sim 140$ °C) of the calcination process. This means that when the correct LCMO phase is formed the template is no longer present and cannot in-

duce any confinement. The disadvantage is that after growth the nanowires cannot be aligned for magnetization measurements. For this template we started by preparing a stoichiometric solution of 2.1M (as in ref. [7]) with the following composition of the sol,

- $\text{La}(\text{NO}_3)_3 = 4.33 \text{ gr}$
- $\text{Mn}(\text{NO}_3)_2 = 2.68 \text{ gr}$
- $\text{Ca}(\text{NO}_3)_2 = 0.82 \text{ gr}$
- $\text{H}_2\text{O} = 7 \text{ ml}$
- ethylene glycol = 7 ml

This sol was only heated at 150°C for 15 min . The filling is done by simply immersing the template in the sol, no pressure difference is required to pull the sol into the pores. The filled template was heated to 800°C for 5 h in air to fully burn away the template. In Fig. A.11 we show one of the SEM images which were obtained on this sample after the calcination process. In this SEM image we can clearly see LCMO nanowires. The wires have varying diameters between 50 nm - $1 \mu\text{m}$ and length up to $5 \mu\text{m}$. Although with this process we cannot control nanowire diameter and the directional alignment of the wires, it was the only attempt which resulted in continuous LCMO wires. From this it seems possible that confinement of the sol during the calcination process is detrimental for nanowire fabrication. We have also repeated this process but now performing the calcination process in flowing O_2 . In Fig. A.12 we show a SEM image of this sample after calcination and the corresponding magnetic properties as well as a magnetization vs. temperature measurement for the sample from Fig. A.11. Although we were unable to observe nanowires in the sample calcinated in oxygen (see Fig. A.12a) the sample does show enhanced ferromagnetism compared to the sample which was calcinated in air. This growth process should be reproduced and refined in the future. Initial attempts to manipulate a single wire using a nanomanipulator did not succeed. Future experiments are required to place a single wire on a set of predefined Au-contacts for transport measurements of single LCMO wires.

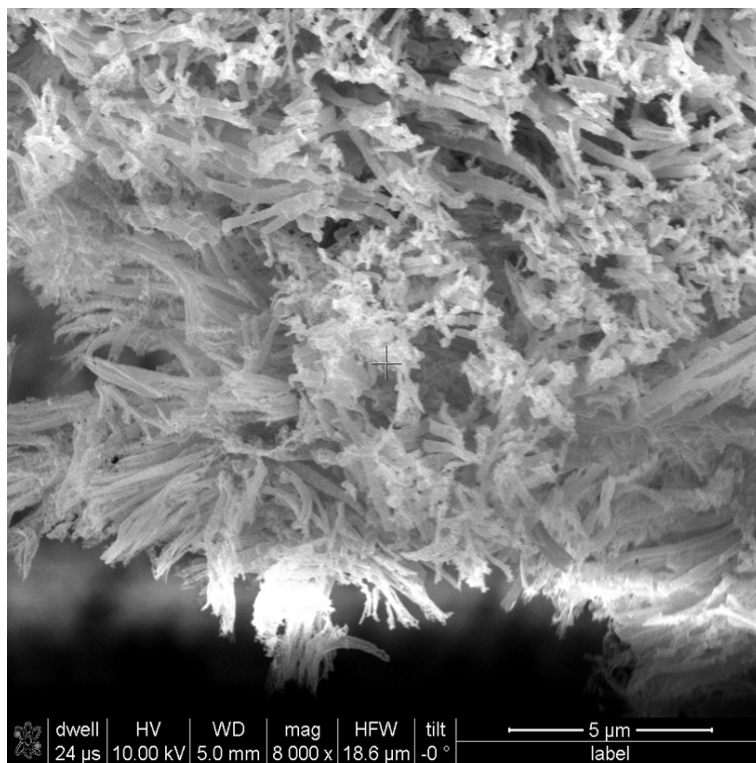


Figure A.11 — SEM image of nanowires (sol heated to 150 °C for 15 min) after heating the filled PCB template to 800 °C for 5 hours in air.

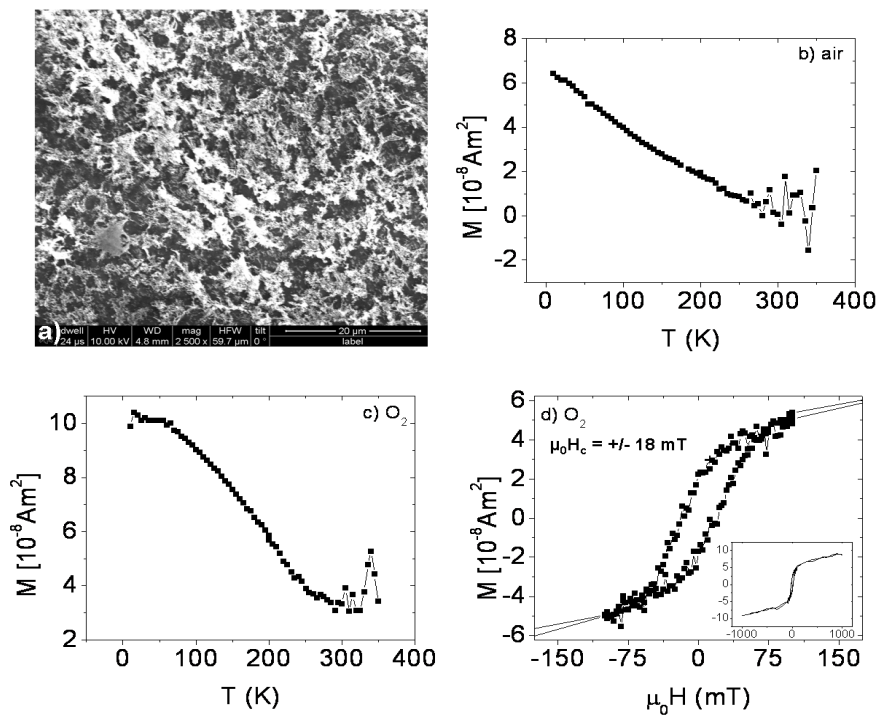


Figure A.12 — a) SEM image of the PCB template filled with 2.1M sol after calcination. b) Magnetization vs. temperature of PCB template filled with 2.1M sol after calcination in air. c) and d): Magnetic properties of PCB template filled with 2.1M sol after calcination in flowing O_2 . M vs. T is measured in $B = 0.1 \text{ T}$ and M vs. B is measured at $T = 100 \text{ K}$.

A.4 Discussion

The first point to make is that we have not been able to reproduce the results of ref. [1] for the case of LCMO. In this chapter we have shown that growing complex oxide nanowires using a template assisted sol-gel process is difficult. There are several process parameters which are critical for successful growth. The solution should have the correct stoichiometry and a minimal solid content to form continuous structures during calcination. A correct choice of template is absolutely critical. In the case of anodized alumina, previously reported to be successfully used in LSMO and LCMO nanowire growth, we observe two problems which are detrimental to the growth process. First, it is very difficult to get proper filling of the pores with the sol. This appears to be independent of sol viscosity. Even the unheated sol, with viscosity slightly higher than water, can only be inserted into the pores if a pressure difference is applied. Apparently, the template is not very hydrophilic, which results in poor filling fraction. The second problem is the confinement of the sol during calcination. The alumina do not disintegrate upon heating to higher temperatures. Therefore, the material remains confined when the LCMO phase is formed. This confinement seems to inhibit the growth of continuous structures in alumina templates. We have shown that we can overcome these problems, by using a polycarbonate template which resulted (for one attempt) in successfully grown LCMO nanowires. For this template filling is easily achieved by putting the template in the solution. Apparently, the loss of the template at an early stage of the calcination process happens after the wires are sufficiently formed. The disadvantage of using the PCB template is the lack of control in wire diameter and directional alignment, which is advantageous for characterization of the magnetic properties. However, with this template an additional process step which involves the dissolving of the membrane to extract the nanowires can be omitted.

A.5 Conclusion

We have presented a recipe for a sol-gel template assisted growth process for LCMO nanowires. We have provided results and discussions for various possible templates; we have shown that the PCB template is the most suitable for this process. The next step would be to do a more elaborate characterization of the wires using techniques such as transmission electron microscopy. Furthermore, a single LCMO wire can be positioned on predefined Au-contacts for transport measurements. Here we note that transport measurements of such wires are not straightforward because of their high resistivity.

Bibliography

- [1] K. S. Shankar and A. K. Raychaudhuri, *Nanotechnology* **15**, 1312 (2004); K. S. Shankar, S. Kar, A. K. Raychaudhuri, and G.N. Sabbanna, *Appl. Phys. Lett.* **84**, 993 (2004)
- [2] The templates are commercially available at www.whatmann.com
- [3] K. Nielsch, J. Choi, K. Schwirn, R. B. Wehrspohn, and U. Gosele, *Nano Lett.* **2**, 677 (2002)
- [4] Template fabrication was done in the group of Prof. Dr. Kornelius Nielsch in the Max Planck Institute in Halle, Germany. This group is now at the University of Hamburg, Germany.
- [5] W. Lee, R. Ji, U. Gosele, and K. Nielsch, *Nat. Mater.* **5**, 741 (2006)
- [6] K. Mandal, Subarna Mitra, and P. Anil Kumar, *Europhys. Lett.* **75**, 618 (2006)
- [7] A. Carretero-Genevri, N. Mestres, T. Puig, A. Hassini, J. Oró, A. Pomar, F. Sandiumenge, X. Obradors, and E. Ferain, *Adv. Mater.* **20**, 3672 (2008)

Samenvatting

Overgangsmetaal oxiden met de perovskietstructuur laten een grote variatie in fysische eigenschappen zien. Dit hangt direct samen met de sterke koppeling van de elektronen met het onderliggende rooster, en met de sterke correlaties tussen de elektronen. Het optreden van supergeleiding, magnetisme en ferroelectriciteit in dit type materialen maakt dat ze aantrekkelijk zijn voor fundamenteel onderzoek, maar dat ook over toepassingen gedacht kan worden. De doping-geïnduceerde metaal-isolator overgang in $(\text{La,Ca})\text{MnO}_3$ kan bijvoorbeeld leiden tot gevoeligheid voor elektrische velden zoals in veldeffect transistoren. Tot op heden bestaan dergelijke transistoren uit silicium en er is noodzaak om steeds meer transistoren op een chip te kunnen plaatsen. De halfgeleider microstructuren dreigen hun intrinsieke fysische limiet te bereiken, met name wat betreft de lengte van het kanaal tussen de stroomcontacten. Om de dichtheid op chips dan te verhogen moet er gekeken worden naar andere materialen die over de juiste functionaliteit beschikken voor gebruik in veldeffect transistoren. Kandidaten hiervoor zijn de overgangsmetaal oxiden.

Dit proefschrift beschrijft de karakterisatie van $\text{La}_{0.67}\text{Ca}_{0.33}\text{MnO}_3$ (LCMO) dunne films en microstructuren om een beter begrip van de fysica in kleine geometrieën te verkrijgen, maar ook om de functionaliteit te onderzoeken voor mogelijke applicaties. **Hoofdstuk 2** beschrijft de eigenschappen van het materiaal LCMO. Er wordt achtergrond informatie verstrekt over het uitgangsmateriaal LaMnO_3 en hoe de eigenschappen (zoals kristalstructuur en geleiding) veranderen door het toevoegen van Ca-ionen. Het materiaal LCMO heeft als belangrijke eigenschap dat het een (bijna eerste orde) metaal-isolator (M-I) overgang laat zien die gekoppeld is aan een ferromagnetische-paramagnetische overgang. **Hoofdstuk 3** beschrijft de technieken die gebruikt zijn voor het groeien van de dunne films en de fabricage van de microstructuren. De beschreven films zijn gegroeid op SrTiO_3 (STO) en NdGaO_3 (NGO) substraten zodat de effecten onderzocht kunnen worden die veroorzaakt worden door substraat-geïnduceerde strain (rooster mismatch tussen film en substraat). Tevens worden er films gepresenteerd die op 'gestapt' STO gegroeid zijn, zodat het effect van atomaire stapranden op het substraatooppervlak onderzocht kan worden. Dit hoofdstuk beslaat ook verscheidene karakterisatie technieken en de bijbehorende resultaten, zoals het bepalen van de oppervlakte ruwheid van de films d.m.v. krachtmicroscopie, het bepalen van de dikte door Röntgen diffractie, het bepalen van de

roosterparameters van het kristal en het bepalen van de compositie en Mn valentie profielen van de film. Als laatste wordt hier een probleem beschreven dat optreedt in het fabricage proces van microstructuren op STO substraten met behulp van ionen-etsen; na het oplossen hiervan kunnen de geleidingseigenschappen van de LCMO microstructuren op een betrouwbare manier bestudeerd worden. De karakterisatie wordt in **Hoofdstuk 4** uitgebreid met de magnetotransport eigenschappen van de ongestructureerde dunne films. Dit leidt tot een directe correlatie van een waargenomen reductie in de Mn valentie aan het film-substraat oppervlak met een tekort aan magnetisch moment in de film (i.e. de film bevat een magnetisch 'dode' laag). Verder veranderen de eigenschappen van de film sterk met de filmdikte, en door gebruik van de verschillende substraten. Dit is voornamelijk zichtbaar in de dikte afhankelijkheid van de temperatuur (T_{MI}) waarbij de M-I fase overgang optreedt. Een gereduceerde filmdikte leidt tot een lagere waarde voor T_{MI} ; dit effect wordt toegeschreven aan strain. De aanwezigheid van stapranden leidt echter tot relatieve verhoging van T_{MI} en wordt toegeschreven aan een toename van wanorde (puntdefecten) in de film. In **Hoofdstukken 5 en 6** worden respectievelijk de transport eigenschappen en de veld-effecten van LCMO microstructuren bestudeerd. De waarnemingen leiden tot een scenario wat verschillende stadia van de elektronenstructuur beschrijft als functie van temperatuur. Bij lage temperaturen (ver onder T_{MI}) is het materiaal een metaal met inhomogeniteiten. Ver boven T_{MI} gedraagt het materiaal zich als halfgeleider en laat temperatuur-geactiveerd gedrag zien. In de faseovergang wordt echter sterk niet-linear gedrag gevonden in de stroom-spanning (I-V) karakteristieken, en treden er sterke veldeffecten op. De niet-lineariteiten, net onder T_{MI} , worden verklaard door het vormen van een gecorreleerde elektronglas fase. Het 'smelten' van de deze (homogene) fase leidt tot een toename van de geleiding van de microbrug met toenemende stroomdichtheid. De oorzaak van de waargenomen veldeffecten, bij lage temperatuur of in de overgang, is echter een andere, en hangt eerder samen met de aanwezigheid van inhomogeniteiten in de microbrug. De geleiding wordt beïnvloed door het elektrisch veld als de overgang van metaal naar isolator inzet, maar verdwijnt weer als de homogene glas fase gevormd wordt. In **Hoofdstuk 7** worden de belangrijkste observaties en conclusies samengevat en met elkaar gecorreleerd. Een nadeel van het materiaal LCMO is dat al deze sterke effecten ver beneden kamertemperatuur optreden. In de literatuur wordt beschreven dat LCMO nanodraden een hogere T_{MI} hebben, zelfs boven kamertemperatuur. In de **Appendix** onderzoeken we een nanodraden fabricage proces, maar komen tot de conclusie dat de claims prematuur zijn.

Summary

Transition metal oxides with the perovskite structure show a wide variety of physical properties. This is correlated with the strong coupling between the electrons and the crystal lattice, and with the strong correlations between the electrons. The occurrence of superconductivity, magnetism and ferroelectricity in this type of material makes them attractive for fundamental research but also allows to consider applications. The doping-induced metal-insulator transition in $(\text{La,Ca})\text{MnO}_3$ can for instance lead to sensitivity to electric fields, as in field effect transistors. Until now such transistors consist of silicon and there is the necessity to keep increasing the density of transistors on a chip. However, the semiconductor microstructures (in particular length of channel between the current contacts) are approaching their intrinsic physical limit. Therefore, further increase of the circuit density requires the consideration of other channel and gate-oxide materials, such as transition metal oxides.

This thesis describes the characterization of $\text{La}_{0.67}\text{Ca}_{0.33}\text{MnO}_3$ (LCMO) thin films and microstructures to better understand the physics in small geometries, but also to investigate functionality for future applications. **Chapter 2** describes the properties of the material LCMO. Background information is provided on the parent material LaMnO_3 , and the influence of Ca-doping on properties such as crystal structure and conductivity is discussed. The material LCMO has the important property that it shows an almost first order metal-insulator (M-I) transition which is coupled to a ferromagnetic-paramagnetic transition. **Chapter 3** describes the techniques used for the thin film growth and microstructure fabrication. The films are grown on SrTiO_3 (STO) and NdGaO_3 (NGO) substrates which allows investigation of the effect of epitaxial strain (lattice mismatch between film and substrate). Furthermore, films are presented which are grown on misoriented STO substrates to investigate the influence of unit-cell high steps on the substrate surface. This chapter also describes the several characterization techniques and corresponding results such as the determination of film roughness with atomic force microscopy, the use of X-ray diffraction to determine thickness and lattice parameters and the determination of composition and Mn valence profiles across the films. Lastly, a problem which occurs during microstructure fabrication by ion-etching on STO substrates is discussed. After solving this problem the transport properties of LCMO microstructures can be studied in a reliable way. The characterization is extended in **Chapter 4** to include

the magnetotransport properties of unstructured LCMO thin films. This leads to a direct correlation between an observed reduction in Mn valence at the substrate-film interface and a lack of magnetic moment in the films (i.e. the film contains a magnetically 'dead' layer). Also, the film properties are both sensitive to film thickness and to the substrate used. This is mainly visible in the thickness dependence of the temperature (T_{MI}) at which the M-I phase transition occurs. A reduced film thickness leads to a lower value for T_{MI} ; this effect is associated with epitaxial strain. The presence of step edges on the STO surface leads to a relative increase of T_{MI} and is attributed to an increased amount of disorder (point defects) in the film. In **Chapters 5 and 6** the transport properties and electric field effects of LCMO microstructures are investigated. The observations lead to a scenario in which the different stages of the electronic structure are described as function of temperature. At low temperature (far below T_{MI}) the material is a metal with inhomogeneities. Far above T_{MI} the material behaves as a semiconductor and shows activated behavior. However, in the phase transition strongly nonlinear behavior is found in the current-voltage (I-V) characteristics and strong field effects appear. The nonlinearities, just below T_{MI} , are associated with the formation of a correlated electron glass phase. The 'melting' of this (homogeneous) phase leads to an increased conductivity of the microbridge when the current density is increased. However, the cause for the observed field effects in LCMO, both at low temperature and in the transition, is different, and is attributed to the presence of inhomogeneities in the microbridge. The conductance is influenced by the electric field when the transition from metal to insulator starts, but disappears when the homogeneous glass phase is formed. In **Chapter 7** the major findings and conclusions are summarized and interconnected. A disadvantage of the material LCMO is that the strong effects occur well below room temperature. In literature experiments are described in which LCMO nanowires show increased values for T_{MI} , even above room temperature. In the **Appendix** we investigate a nanowire fabrication process, however, we conclude that these claims are premature.

Curriculum vitae

Ik ben geboren op 12 oktober 1980 te Amsterdam. Na het behalen van mijn VWO diploma aan het Solyvius College te Hoofddorp ben ik begonnen met de studie Natuurkunde aan de Universiteit van Leiden. Tijdens mijn master heb ik een tweetal onderzoeksstages uitgevoerd. Eén daarvan was aan het FOM instituut AMOLF te Amsterdam waar ik water onderzocht met Terahertz spectroscopie, en de ander bij Prof. Dr. J. Aarts in de magnetische en supergeleidende materialen groep te Leiden met als titel: Supergeleidende eigenschappen van Al/Py hybride structuren. Vrijwel direct na het behalen van mijn doctoraal examen begon ik als FOM-OIO, eveneens onder leiding van Prof. Aarts, aan het werk beschreven in dit proefschrift. Ik heb delen hiervan in de afgelopen jaren verscheidene malen gepresenteerd in de vorm van posters en voordrachten op zowel nationale als internationale conferenties. Tijdens mijn studie en mijn promotie-onderzoek ben ik ook bezig geweest met andere zaken waaronder twee bestuursfuncties. De eerste was bij de Stichting RINO (een groep enthousiaste studenten die met demonstraties van natuurkundige effecten door het land reizen) en de tweede als penningmeester bij de Ultimate Frisbee vereniging genaamd 'Panic'. De volgende stap in mijn carrière betreft een postdoc positie aan de Universiteit van Toronto, Canada waar ik in maart 2010 zal beginnen.

Publicatielijst

REFEREED PAPERS

- *C. Beekman*, I. Komissarov, M. Hesselberth, and J. Aarts, **Transport properties of microstructured ultrathin films of $\text{La}_{0.67}\text{Ca}_{0.33}\text{MnO}_3$ on SrTiO_3** , Applied Physics Letters **91**, 062101 (2007)
- *C. Beekman*, and J. Aarts, M. Porcu, and H. Zandbergen, **Effects of strain on transport properties of $\text{La}_{0.67}\text{Ca}_{0.33}\text{MnO}_3$ ultra thin films**, Physical Review B, in preparation
- *C. Beekman*, and J. Aarts, **Mesoscopic transport in $\text{La}_{0.67}\text{Ca}_{0.33}\text{MnO}_3$ thin films**, Physical Review Letters, in preparation
- I. Mubeen, *C. Beekman*, X. He, and J. Aarts, **Variations in the Hall coefficient for strained and unstrained films of $\text{La}_{0.7}\text{Ca}_{0.3}\text{MnO}_3$ and $\text{La}_{0.7}\text{Sr}_{0.3}\text{MnO}_3$** , Physical Review B, in preparation

POPULAR ARTICLES

- *C. Beekman* **Veldeffecten in manganaten** Eureka, Tijdschrift van de Universiteit van Leiden Faculteit natuurwetenschappen, 24, Feb. 2009

Nawoord

Ik ben 10 jaar in Leiden werkzaam geweest. Eerst als student en de afgelopen 4.5 jaar als promovenda. Het is een hele leuke tijd geweest en daarom wil ik hier alle mensen noemen die daar op enige manier aan hebben bijgedragen. Om te beginnen wil ik Jan Aarts bedanken voor de geboden begeleiding bij de totstandkoming van dit proefschrift. De samenwerking met alle leden van de magnetische en supergeleidende materialen groep was erg goed. Marcel Hesselberth, Ruud Hendriks en Daan Boltje zijn altijd erg behulpzaam geweest met hun technische ondersteuning. De samenwerking met alle studenten, postdocs en gasten van de groep was ook altijd erg plezierig. Ik wil hier in het bijzonder Ishrat Mubeen (also thanks for the lovely Pakistani food), Ivan Komissarov, Xin He and Yuqin Zhang noemen vanwege de goede samenwerking en discussies op het gebied van oxiden. Ik heb in de afgelopen jaren ook een aantal samenwerkingsverbanden opgezet. Ik heb daardoor vele interessante discussies gehad met veel wetenschappers van andere universiteiten: vooral de Universiteit van Delft (Mauro Porcu) en Twente (Andre ten Elshof, Michiel Maas en Hans Boschker). Ik wil hier ook graag Fred Kranenburg noemen voor zijn hulp met alle meetcomputers, en Kiri Nichol voor haar gezelligheid tijdens koffiepauzes maar ook tijdens de kayak- en schaatsuitjes. Naast mijn collega's heb ik ook veel gehad aan de steun en vriendschap van andere mensen. De vele erg gezellige meidenavonden en vakanties met Anne-Marie, Barbera, Caroline, Demerese, Frederike, Marieke en Mascha zijn ook erg belangrijk geweest in het met succes volbrengen van dit werk. Ik ben ook met veel plezier twee jaar lid geweest van Ultimate Frisbee vereniging Panic. Ik wil alle leden van Panic bedanken voor de gezelligheid en sportiviteit tijdens de trainingen, competitiedagen en tijdens tal van georganiseerde evenementen. Als laatste wil ik nog mijn familie, mijn zussen Barbera, Marina en mijn ouders Rina en Elbert bedanken voor hun steun en bijdrage. Ik wil in het bijzonder mijn moeder bedanken voor het ontwerpen van de omslag.